A Cosmic ORigins Explorer (COrE) Satellite Mission for probing Cosmic origins, neutrinos masses and the Origin of Stars and Magnetic Fields through a high-sensitivity survey of the microwave polorization on the full sky

A proposal in response to the
European Space Agency Cosmic Vision 2015-2025 Call

First draft due 10 November 2010—final draft due 24 November 2010
Submission deadline : 3 December 2010

LATEX information for assembling the first draft

Contents

1 Cover page (1 page) PdB, FRB

Free format, should contain the proposal title.

2 Proposal contact details (1 page) PdB, FRB

Should contain the proposal title, and name and contact details of the proposal's contact person. It can also contain a list of proposers and their institutions. This will form the back of the cover page when the proposal is printed two-sided.

3 Executive Summary (2 pages) PdB, FRB

Text

4 Introduction (1 page) PdB, FRB

Text

5 Scientific objectives and requirements Bucher (12 pages)

Text

5.1 Physics of the Beginning (2) Bucher

Text

5.1.1 Inflation & B-modes Melchiorri, Ferreira Garcia-Bellido....

One of the striking developments to arise in the past few decades is the concept and mechanism of *Cosmic Inflation*. Put simply, there is compelling evidence that the Universe underwent a period of very rapid, sometimes dubbed *superluminal*, expansion at very early times. As a result of Inflation, the Universe ended up in a special, almost perfectly homogeneous state with a geometry which is almost exactly Euclidean.

A key prediction to arise from Inflation is that the large scale structure of the Universe was seeded by quantum fluctuations in fabric of space time in conjunction with those in the underlying energy content of the Universe at that time. These seeds can be described as an almost perfect Gaussian random field, with a scale invariant spectrum of both scalar and tensor fluctuations. The scalar fluctuations are the seeds for density perturbations that lead to the formation of the Cosmic Web. The tensor fluctuations are the gravitational waves that may be detected in the large scale polarization of the CMB.

The theory of Inflation has been extraordinarily successful when confronted with the new spate of high quality cosmological data, most notably, the WMAP data and we are clearly at the cusp of understanding the workings of the early Universe by targetting observations which directly probe the energy scale and the dynamics of inflation. This can be done directly through measurements of the running of the spectral index (defined below), the relative amplitude of gravitational wave fluctuations relative to density fluctuations and through deviations from non-Gaussiniaty. The temperature and polarization of the CMB are the observables of choice for achieving this goal.

The simplest model of inflation is based on a single scalar field ϕ having a potential $V(\phi)$. The overall energy density in the scalar field (neglecting fluctuations) is the sum of a kinetic and potential terms $\rho = \frac{1}{2}\dot{\phi}^2 + V(\phi)$, while its pressure is given by $p = \frac{1}{2}\dot{\phi}^2 - V(\phi)$. The energy and pressure of the scalar field drive the expansion of the universe according to the Einstein equations

$$H^2 \equiv \left(\frac{\dot{a}}{a}\right)^2 = \frac{8\pi G}{3}\rho - \frac{k}{a^2}, \qquad \frac{\ddot{a}}{a} = -\frac{4\pi G}{3}(\rho + 3p) \tag{1}$$

where $a(t)$ is the scale factor of the Universe and H is the Hubble parameter. To obtain an epoch of inflationary expansion, we consider a *slow-roll* regime, $p \approx -\rho \approx -V(\phi)$, and find that the expansion accelerates, with the scale factor evolving as $a(t) \propto e^{Ht}$ where $H^2 = (8\pi G/3)V$. The geometry of the Universe is closely tied to the fractional energy density, Ω, of the Universe; during Inflation we have that $\Omega \to 1$, driving the Universe to a Euclidean geometry. A period of Inflation also resets the initial state of the observable Universe, as a patch of space that undergoes inflation becomes exponentially stretched and smoothed. Both of these predictions are spectacularly born out by observations.

As mentioned above, one of the striking predictions to arise from inflation is a mechanism for seeding large scale structure from quantum fluctuations in the primordial Universe. The statistical properties of the large-scale structure imprinted during inflation depend on the form of the potential $V(\phi)$ for the scalar field ϕ driving inflation. It is convenient to define the following dimensionless *slow-roll* parameters: $\epsilon \equiv \frac{M_{Pl}^2}{2}\left(\frac{V'}{V}\right)^2$ and $\eta \equiv M_{Pl}^2\frac{V''}{V}$ where $M_{Pl} = (8\pi G)^{-1/2}$ is the reduced Planck mass. Both parameters must be small during inflation and in the discussion below we shall assume the slow-roll approximation $\epsilon, \eta \ll 1$.

*S*calar perturbations arising from inflation imprint irregularities in the energy density of the Universe, which can be described as a Gaussian random field with amplitude A_S (i.e., $\left\langle \delta^2 \right\rangle = 2\pi^2 A_S^2/k^3$) that depends on the wave number k where $A_S(k) \approx \frac{1}{5\sqrt{3}\pi}\left(\frac{V^{1/2}(\phi)}{M_{pl}^2}\right)\epsilon^{1/2}$ Here k is the co-moving wave number, and the fluctuations are imprinted as that scale "crosses the horizon". The amplitude will depend on scale and we can define a scalar spectral index through $n_S \equiv 1 + \frac{d\ln A_S^2(k)}{d\ln k} \approx 1 + 2\eta - 6\epsilon$. In the extreme slow roll limit, the spectrum of density perturbations is almost scale invariant, with $n_S \approx 1$.

Inflation also generates *tensor perturbations*; transverse traceless perturbations in the metric of space time that can be described in terms of two spin-2 polarization states which obey the equations of a massless scalar field and are therefore called gravity waves. Their amplitude and spectral index are given by $A_T(k) \approx \frac{1}{5\sqrt{6}}\frac{V^{1/2}}{\pi M_{Pl}^2}$ at horizon crossing and $n_T \approx -2\epsilon$ where A_T is defined so that $A_T^2/A_S^2 = \epsilon$ to lowest order. The relative contribution of gravity waves to curvature perturbations is given by the *tensor-to-scalar* ratio $r = (T/S) \equiv 16\frac{A_T^2}{A_S^2} \approx 16\epsilon$. Using the COBE normalization $A_S = 1.91 \times 10^{-5}$, we find that $V^{1/4} = 3.3 \times 10^{16}\,(T/S)^{1/4}$ GeV. Hence a measurement of (T/S) directly probes the energy scale of Inflation and is a window onto the early Universe.

There is a wide range of models of inflation the simplest of which is single-field inflation that satisfies the Lyth relation, $\frac{\Delta\phi}{M_{\rm Pl}} \simeq \left(\frac{(T/S)}{0.01}\right)^{1/2}$ where $\Delta\phi$ is the variation in the inflaton field between the end of inflation and the time at which CMB-scale perturbations were generated. The Lyth relation implies that tensor modes may be detectable if inflation involves a large field variation. Candidate theories that lead to large-field variation are the *chaotic* inflation models which can be severely constrained if no tensor modes are detected at a level of $(T/S) \sim 0.1$. Small-field inflation models are much more difficult to rule out via the tensor amplitude, with most models generically predicting $(T/S) < 0.01$ and may be constrained more effectively by the measurements of the spectral index and its running. Hence, a measurement of tensor amplitude in the CMB will be invaluable in discriminating and ruling out a large class of single-field models.

String theory contains an abundance of light scalar fields which may be responsibe for Inflation. Examples are the *hybrid* inflation models which involve two (or more scalar fields) and generally produce a negligible tensor amplitude and $n_S > 1$ although complicated multi-field models can be constructed with a large number of fields which lead to a broad spectrum of predictions for the amplitude of tensor modes. In recent years the so-called *curvaton* model of multi-field inflation has been a subject of considerable interest and produces a smaller tensor amplitude than a single-field model (for example, $(T/S) \approx 0.3$ in the single-field ϕ^4 model, but $(T/S) \approx 0.08$ when a curvaton field is included). This effectively validates large-field inflationary mechanisms which would have been ruled out otherwise. Unlike a single-field model, the curvaton generically produces isocurvature perturbations and large non-Gaussianities which are intimately tied to T/S. Other candidates arise with non-standard kinetic terms in the Lagrangian leading to *Dirac-Born-Infeld* Inflation. These models have the particularity of introducing both lower and upper bounds on T/S.

CMB temperature and polarization anisotropies are by far the most promising route to explore the physics behind inflation. Recent measurements by the Wilkinson Microwave Anisotropy Probe (WMAP) satellite combined with the ground-based and balloon-borne experiments, and probes of large scale struc-

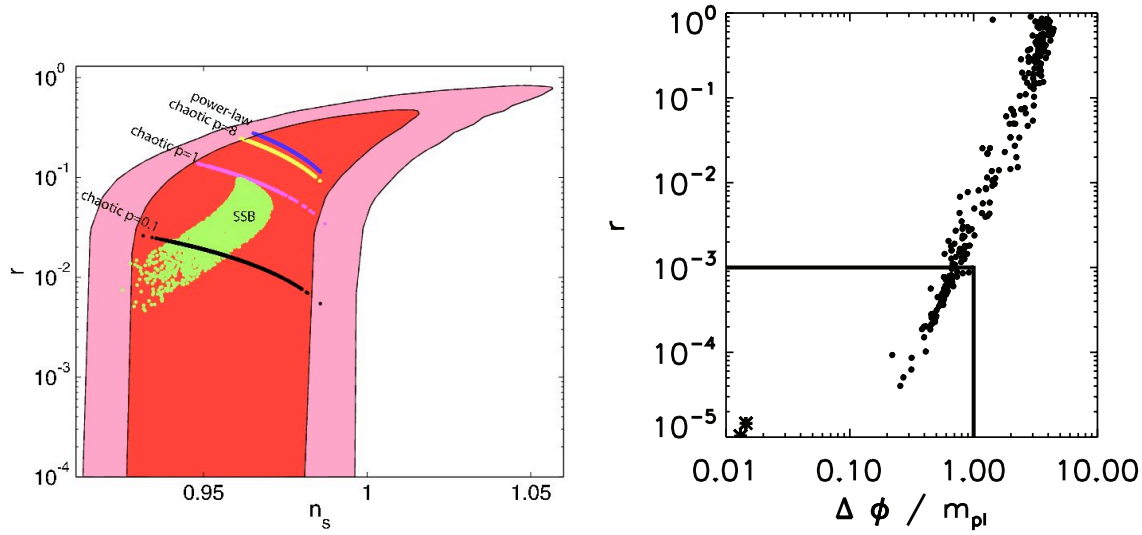

Figure 1: On the left we show model dependent WMAP7 (red shaded areas) constraints to the n_s-r parameter space. The outer (inner) contours are the 2σ (1σ) contours. We also plot the models within $\Delta\chi^2 = 1$ (1σ) from the best fit for power-law and chaotic models, and at $\Delta\chi^2 = 2.3$ (also 1σ) for the SSB models. On the right we show a model independent analysis using the WMAP7 data to constrain the absolute value of the range traversed by the scalar field ϕ over the final 55 e-folds of inflation, $\Delta\phi$, against the tensor-to-scalar ratio r.

ture, have sharpened our knowledge of some key inflationary parameters. The recent analysis in WMAP7 constrains $r < 0.24$ and $n_S = 0.968 \pm 0.012$ (which intriguingly places it at 3-sigma away from pure scale invariance). If running spectral index is allowed, constraints become $r < 0.49$, $ns = 1.076 \pm 0.065$ and $dn_S/d\ln k = -0.048 \pm 0.029$.

The panorama of inflationary models is sufficiently vast and intricate that it is, in practice, difficult to make definitive statements about Inflation as a whole. Yet, it is possible to, given current cosmological constraints, to forecast the expected amplitude of T/S (or equivalently r) for classes of models. A possibility is to consider a reasonable extensive set of models as we do in the left hand plot in Figure 1 . There we consider *Power Law*, *Chaotic* (where the potential is of the form $V(\phi) \simeq \phi^p$) and *Spontaneous Symmetry Breaking* Inflationary models and find current constraints on r and n_S. In choosing this subclass of models we are naturally making specific prior assumptions yet we can get a clear sense of what to expect in terms of the amplitude of gravity waves.

A more model independent approach is taken in the right hand plot of Figure 1 which shows extracts from a 2-million point Monte-Carlo simulation of the inflationary flow equations (adapted from [**?**]). In this approach one starts from Hamilton-Jacobi formulation of inflationary dynamics, expressing the Hubble parameter directly as a function of the field ϕ. Then one reformulates the exact dynamical equations for inflation as an infinite hierarchy of flow equations; in practice one has to truncate the infinite hierarchy at some finite order. Fortunately the results do not depend strongly on choices of prior ranges leading once known observational constraints (on n_s and $dn_s/d\ln k$) are imposed, leading to somewhat model-independent constraints on r. Figure ... shows that models do not cover the observable parameter space uniformly and that there are significant concentrations of points with significant tensor/scalar ratio. From these two different analysis it is clear that $r \sim 10^{-3}$ is a natural target for a CMB polarization experiment.

** WHAT IS ACHIEVABLE GIVEN FOREGROUNDS**?

5.1.2 Inflation & B-modes Text from Hiranya Peiris and Licia Verde

CORE Proposal-Inflation and Tensor Modes

last modified November 22, 2010

Preamble

One of the striking developments to arise in the past few decades is the concept and mechanism of *Cosmic Inflation*. Put simply, there is compelling evidence that the Universe underwent a period of very rapid, sometimes dubbed *superluminal*, expansion at very early times. As a result of Inflation, the Universe ended up in a special, almost perfectly homogeneous state with a geometry which is almost exactly Euclidean.

A key prediction to arise from Inflation is that large scale structure was seeded by quantum fluctuations in fabric of space time in conjunction with those in the underlying energy content of the Universe at that time. The seeds of large scale structure can be described as an almost perfect Gaussian random, with a scale invariant spectrum of both scalar and tensor fluctuations. The scalar fluctuations are the seeds for density perturbations that lead to the formation of the Cosmic Web. The tensor fluctuations are the gravitational waves that may be detected in the large scale polarization of the CMB.

The theory has been extraordinarily successful when confronted with the new spate of high quality cosmological data, most notably, the WMAP data. Furthermore, in roads have been in made in very mild deviations from both scale invariance and attempting to constrain deviations from Gaussianity. These precise measurements can then be used to learn about the details of cosmological inflation itself.

We are clearly at the cusp of understanding the workings of the early Universe and we can do this be targetting observations which directly probe the energy scale and the dynamics of inflation. This can be done directly through measurements of the running of the spectral index (defined below), the relative amplitude of gravitational wave fluctuations relative to density fluctuations and through deviations from non-Gaussiniaty. The temperature and polarization of the CMB are the observables of choice for achieving this goal.

The Physics of Inflation

In what follows, we describe the simplest model of inflation based on a single scalar field ϕ having a potential $V(\phi)$- the description we present here can be easily generalized to a very broad class of models involving more fields. If we focus on the overall dynamics of the Universe, we have that the energy density in the scalar field is the sum of a kinetic and potential terms $\rho = \frac{1}{2}\dot{\phi}^2 + V(\phi)$, while its pressure is given by $p = \frac{1}{2}\dot{\phi}^2 - V(\phi)$. The energy and pressure of the scalar field drive the expansion of the universe according to the Einstein equations

$$H^2 \equiv \left(\frac{\dot{a}}{a}\right)^2 = \frac{8\pi G}{3}\rho - \frac{k}{a^2}, \qquad \frac{\ddot{a}}{a} = -\frac{4\pi G}{3}(\rho + 3p) \tag{2}$$

where $a(t)$ is the scale factor of the Universe (i.e., the homogeneous component of the metric of space time $ds^2 = g_{\mu\nu}dx^\mu dx^\nu$). To obtain an epoch of inflationary expansion, we consider a *slow-roll* regime, $p \approx -\rho \approx -V(\phi)$,. From eqn. 2 we observe (for $k = 0$) that the expansion accelerates, with the scale factor evolving as $a(t) \propto e^{Ht}$ where $H^2 = (8\pi G/3)V$.

¿From this simple one-field model we can extract some key consequences. The geometry of the Universe is closely tied to the fractional energy density of the Universe, $\Omega \equiv \rho/\rho_C$, where $\rho_C = (3/8\pi G)H_0^2$ is the critical energy density, and H_0 is the Hubble constant today. During an inflationary period we have that $|1 - \Omega| \propto \exp(-2Ht)$ and which implies that $\Omega \to 1$ corresponding to a Euclidean geometry. A period of inflation also resets the initial state of the observable Universe, as a patch of space that undergoes inflation becomes exponentially stretched and smoothed. Both predictions- that Ω is close to 1 and the Universe is smooth to 1 part in 10^5 on large scales- have been born out by measurements of the CMB.

Observing Inflation

As mentioned above, one of the striking predictions to arise from inflation is a mechanism for seeding large scale structure from quantum fluctuations in the primordial Universe. The statistical properties of the large-scale structure imprinted during inflation depend on the form of the potential $V(\phi)$ for the scalar field ϕ driving inflation. It is convenient to define the following dimensionless *slow-roll* parameters: $\epsilon \equiv \frac{M_{Pl}^2}{2}\left(\frac{V'}{V}\right)^2$ and $\eta \equiv M_{Pl}^2\frac{V''}{V}$ where $M_{Pl} = (8\pi G)^{-1/2}$ is the reduced Planck mass. Both parameters must be small during inflation and in the discussion below we shall assume the slow-roll approximation $\epsilon, \eta \ll 1$.

Scalar perturbations arising from inflation imprint irregularities in the energy density of the Universe, which can be described as a Gaussian random field with amplitude A_S (i.e., $\left\langle \delta^2 \right\rangle = 2\pi^2 A_S^2/k^3$) that depends on the wave number k where $A_S(k) = \frac{2}{5}\mathcal{P}_R^{1/2}(k) \approx= \frac{1}{5\sqrt{3}\pi}\left(\frac{V^{1/2}(\phi)}{M_{pl}^2}\right)\epsilon^{1/2}$ Here k is the co-moving wave number, and the fluctuations are imprinted as that scale "crosses the horizon". The amplitude will depend on scale and we can define a scalar spectral index through $n_S \equiv 1 + \frac{d\ln A_S^2(k)}{d\ln k} \approx 1 + 2\eta - 6\epsilon$. In the extreme slow roll limit, the spectrum of density perturbations is almost scale invariant, with $n_S \approx 1$.

Inflation also generates *tensor perturbations*; transverse traceless perturbations in the metric of space time $g_{ij} = a^2(t)(\delta_{ij} + h_{ij})$. They can be described in terms of two spin-2 polarization states h_+ and $h_\times$ which obey the equations of a massless scalar field and are therefore called gravity waves. Their amplitude and spectral index are given by $A_T(k) \approx \frac{1}{5\sqrt{6}}\frac{V^{1/2}}{\pi M_{Pl}^2}$ at horizon crossing and $n_T \approx -2\epsilon$ where A_T is defined so that $A_T^2/A_S^2 = \epsilon$ to lowest order. The relative contribution of gravity waves to curvature perturbations is given by the *tensor-to-scalar* ratio

$$(T/S) \equiv 16\frac{A_T^2}{A_S^2} \approx 16\epsilon. \tag{3}$$

Using the COBE normalization $A_S = 1.91 \times 10^{-5}$, we find that $V^{1/4} = 3.3 \times 10^{16}\,(T/S)^{1/4}\,\mathrm{GeV}$, relating (T/S) to the energy scale of inflation.

Models of Inflation

There is a wide range of models of inflation. The simplest class is that of single-field inflation that satisfy the Lyth relation, $\frac{\Delta\phi}{M_{\rm Pl}} \simeq \left(\frac{(T/S)}{0.01}\right)^{1/2}$ where $\Delta\phi$ is the variation in the inflaton field between the end of inflation and the time at which CMB-scale perturbations were generated. The Lyth relation implies that tensor modes may be detectable if inflation involves a large field variation. It is therefore convenient to classify single-field models into two broad categories, namely, large-field ($\Delta\phi \gtrsim M_{\rm Pl}$) and small-field models ($\Delta\phi < M_{\rm Pl}$).

One of the most widely studied type of large-field models is the monomial potential $V(\phi) \propto \phi^\alpha$. The case when α is a positive integer is typical of the "chaotic" inflation scenario, in which inflation began with a chaotic initial condition. In particular, the model with $\alpha = 2$ is generally regarded as the simplest and best motivated model which continues to be consistent with observation. Other models include those in which α is a negative integer or a fraction, as in the case of some string-inspired models. In general, this class of models will be severely constrained if no tensor modes are detected at a level $(T/S) \sim 0.1$. Small-field inflation models are much more difficult to rule out via the tensor amplitude, with most models generically predicting $(T/S) < 0.01$ and may be constrained more effectively by the measurements of the spectral index and its running. Hence, a measurement of tensor amplitude in the CMB will be invaluable in discriminating and ruling out a large class of single-field models.

String theory contains an abundance of light scalar fields which may be responsibe for Inflation. A simple example is the "hybrid" inflation in which the inflaton field ϕ slow-rolls until it reaches a critical value set by a "waterfall" field χ, thus ending inflation suddenly. Hybrid models generally produce a negligible tensor amplitude and $n_S > 1$, rendering them incompatible with the current observational constraint on n_S. More complicated multi-field models can be constructed with a large number of fields (possibly of order 10^3 as in the case of "assisted" or $\mathcal{N}$-flation), all of which may evolve along separate potentials. These additional degrees of freedom inevitably lead to a broad spectrum of predictions for the amplitude of tensor modes. The prospects for constraining multi-field inflation therefore appear extremely challenging.

Nevertheless, in recent years the so-called "curvaton" model of multi-field inflation has been a subject of considerable interest. This model involves two fields, one playing the role of the inflaton and an additional field which generates perturbations. The curvaton model generically produces a smaller tensor amplitude than a single-field model (for example, $(T/S) \approx 0.3$ in the single-field ϕ^4 model, but $(T/S) \approx 0.08$ when a curvaton field is included). This effectively validates large-field inflationary mechanisms which would have been ruled out otherwise. Unlike a single-field model, the curvaton generically produces isocurvature perturbations and large non-Gaussianities. In the simplest case, an interesting consistency

relation exists between (T/S) and the local non-Gaussianity parameter, $f_{\rm NL}$,

$$f_{\rm NL} = \frac{5}{4(T/S)} - \frac{5}{3} - \frac{5}{6}(T/S).$$

Thus, if tensor modes remain undetected, the curvaton may be constrained by a potentially very large non-Gaussianity.

Again, in the context of string theory, extremely flat potentials needed for inflation are problematic since they are associated with very light, unstable fields. A solution is to introduce a non-standard kinetic term in the Lagrangian. One particularly successful scenario of this type is the so-called Dirac-Born-Infeld inflation in which a 3-dimensional brane moves along a "throat" generated by flux fields in a higher-dimensional spacetime. An interesting consequence of the non-canonical kinetic term is that perturbations propagate at a speed, c_s, which may be less than the speed of light. The usual consistency relation for single-field inflation, $(T/S) = -8n_T$ is now replaced by $(T/S) = -8c_s n_T$. A surprising aspect of DBI inflation is that there exist both upper and lower bounds on (T/S). An upper bound, derived by Baumann and McAllister, is given by $(T/S) < \mathcal{C}\left(1 + \frac{1}{3f_{\rm NL}}\right)$, where $\mathcal{C} \ll 1$ depends on the geometry of the throat.

Observational Constraints

CMB temperature and polarization anisotropies are the most promising route to explore the physics behind inflation. Recent measurements by the Wilkinson Microwave Anisotropy Probe (WMAP) satellite seven-year mission [**?**], combined with the ground-based and balloon-borne experiments such as BOOMERanG [**?**], QUAD [**?**], ACBAR [**?**], and BICEP [**?**] have sharpened our knowledge of some key inflationary parameters. With regard to the dynamics of inflation, a hotly debated question is whether the case of $n_S = 1$ is significantly excluded by current observations (see *e.g.,* Refs. [**?**]-[**?**]). The scalar spectral index, n_S, has been recently constrained to the value $n_S = 0.963 \pm 0.014$ at 68% c.l. by the WMAP seven-year dataset (WMAP7) [**?**], disfavoring the value of $n = 1$ at about two standard deviations. A combined analysis with galaxy clustering data gives $n_S = 0.963 \pm 0.012$ at 68% c.l., ruling out $n = 1$ at more than three standard deviations ([**?**], [**?**]).

Compelling evidence that $n_S \neq 1$ would be quite revealing for two reasons. First, as it is well known, a scalar spectral index with an exact value of $n_S = 1$ corresponds to the phenomenological model proposed by Harrison, Zel'dovich, and Peebles [**?**]. While one can construct inflationary models that give $n_S = 1$ either approximately [**?**] or exactly [**?**], they are less than compelling. In fact, observations pointing to n_S exactly unity may indicate that the origin of cosmic perturbations lies in some unknown fundamental process and may not arise from inflation. Secondly, as we discussed in the previous section, in many models of inflation the amplitude of the tensor perturbations are proportional to $|1 - n_S|$. Thus, the larger the departure of n_S from unity, the more likely tensor perturbations would be within observational reach.

Let us now quantify the probability of detecting tensor modes a bit more precisely by considering a variety of functional forms for $V(\phi)$, consistent with current data. As we will see, the amplitude of the IGW background is large enough to be detectable by next-generation experiments in a broad family of inflation models consistent with current data.

We consider three classes of inflationary models [**?**, **?**, **?**]: (1) *Power-law* inflation is characterized by an inflaton potential $V(\phi) \propto e^{\phi/\mu}$, where μ is a mass scale. In this potential, there is a relation, $r = 8(1 - n_s)$, between the tensor-to-scalar ratio and the scalar spectral index. (2) *Chaotic* inflation features an inflaton potential $V(\phi) \propto (\phi/\mu)^p$. In theoretically attractive models, p is a small integer. Experimentally, $p \lesssim 10$ if $n_s \gtrsim 0.9$ [**?**], but p can empirically be arbitrarily small. We consider values of p between $p = 0.1$ and $p = 8$ in our numerical work. In these models, $r = 8[p/(p + 2)](1 - n_s)$. (3) *Spontaneous symmetry-breaking (SSB)* inflation features an inflaton potential $V(\phi) \propto [1 - (\phi/\nu)^2]^2$. The precise model is specified by two parameters: ν and N_e, the number of e-foldings of inflation between CMB scales and the end of inflation. A conservative range for N_e is $47 \lesssim N_e \lesssim 62$, corresponding to an inflationary energy scale in the range of an MeV to 10^{16} GeV, the current upper bound. The n_s-r relation for SSB models cannot be written in a simple way. To obtain it, we use the algorithm given in Eqs. (38)–(41) of Ref. [**?**]. We show in Fig. 2 the corresponding regions in the n_s-r parameter space.

One could also consider hybrid-inflation models, which generally feature multiple fields. Their phenomenology can usually be modeled, though, as a single field with the addition of a non-zero cosmological constant at the inflaton-potential minimum. What distinguishes these models phenomenologically is that

they usually produce $n_s > 1$. Since the working assumption of this paper is that $n_s < 1$, we do not consider these models further, but simply note that if n_s is indeed greater than unity, than these models allow for much smaller IGW amplitudes than the single-field models we consider here.

We therefore re-analyze the CMB data for the power-law, chaotic, and SSB models, imposing the consistency relations between n_s, r, and n_t. To do so, we use the Markov chain Monte Carlo (MCMC) package `cosmomcmc` [**?**] to run a set of chains, imposing these consistency relations. We use only the latest WMAP results. The likelihood is determined using the October 2010 version of the WMAP likelihood. The likelihood are obtained after marginalizing (with flat priors) over the baryon and cold-dark-matter densities, the ratio of the sound horizon to the angular-diameter distance at decoupling, and the optical depth to reionization.

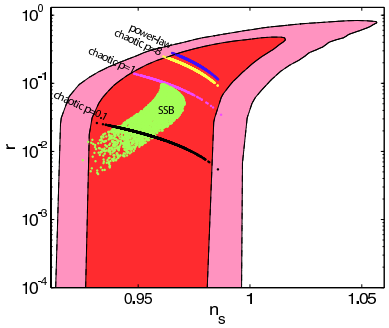

Figure 2: The WMAP (red shaded areas) constraints to the n_s-r parameter space. The outer (inner) contours are the 2σ (1σ) contours. We also plot the models within $\Delta\chi^2 = 1$ (1σ) from the best fit for power-law and chaotic models, and at $\Delta\chi^2 = 2.3$ (also 1σ) for the SSB models. The curves, from top to bottom, are for power-law and for chaotic $p = 8$, $p = 1$, and $p = 0.1$. The (green) points are for the SSB models.

In Table 1, we list the current constraints to n_s and r from WMAP obtained using each class of inflationary models as a prior. As expected, the tabulated values and the plots indicate that tensor modes are required for exponential, power-law, and small-field scenarios.

Our analysis provides a likelihood, from CMB data, for each point along the curves associated with each class of inflationary models. We than thus plot in Fig. 3 the percentage of models with a tensor amplitude above a threshold value r. As shown, almost all of the exponential and power-law models have a tensor amplitude $r > 2 \times 10^{-2}$, while small-field models predict $r > 2 \times 10^{-3}$. If experiments were to probe values of r well below 2×10^{-3} without finding any evidence for gravitational waves, then it would rule out a large class of single-field inflationary models.

We now estimate the fraction of models in each class of models that can be detected by a given experiment.

We consider here four experimental configurations: eight years of WMAP; the Planck satellite [**?**]; and CORE. Since the amplitude of the Galactic foregrounds for polarization is still not determined by observations, we remove channels below 40 GHz and above 250 GHz, as these are likely to be contam-

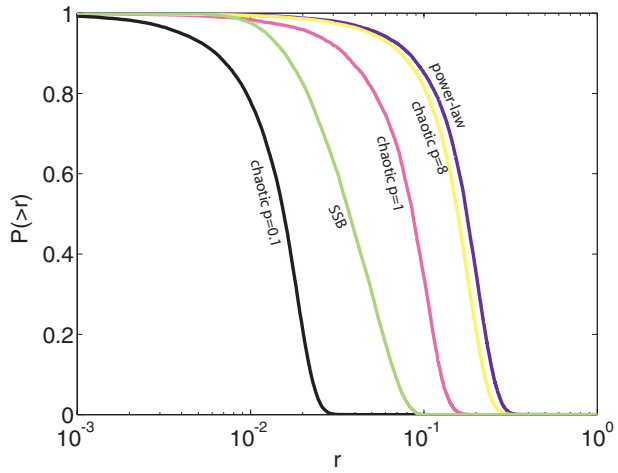

Figure 3: Percentage of inflationary models with a tensor-to-scalar ratio above a threshold value r, for the various inflaton-potential classes considered in Fig. 2. From right to left, the models are power law, chaotic $p = 8$, chaotic $p = 1$, SSB, and chaotic $p = 0.1$.

Model	n_S	r
Power Law	$0.980^{+0.005}_{-0.005}$	$0.16^{+0.04}_{-0.04}$
Chaotic p=1	$0.970^{+0.008}_{-0.008}$	$0.080^{+0.020}_{-0.041}$
Chaotic p=8	$0.978^{+0.011}_{-0.011}$	$0.14^{+0.07}_{-0.07}$
Chaotic p=0.1	$0.964^{+0.019}_{-0.018}$	$0.014^{+0.004}_{-0.007}$
SSB ($N_e = 47 - 62$)	$0.957^{+0.006}_{-0.020}$	$0.042^{+0.010}_{-0.014}$

Table 1: The 68% C.L. limits on the spectral index n_s and the scalar-tensor ratio r from WMAP, assuming the n_s-r relation for each class of inflationary models.

inated by synchrotron and dust emission, respectively. The parameters assumed for these missions are summarized in Table 2.

Our results are reported in Table 3 for detections with 2σ and 5σ significance. Our results suggest that eight years of WMAP data are unlikely to detect IGWs. The Planck satellite, on the other hand, stands a good chance to measure the IGW background at the 5σ confidence level only in power-law models. This forecast, however, may be optimistic, since it assumes perfect foreground removal and full use of 6 channels for cosmology. To understand these effects better, we show forecasts in Table 4 for Planck, assuming first a smaller number of channels and then a more pessimistic configuration where no EE or BB power spectra are used. While we found only a small degradation in decreasing the number of channels from 6 to 4, using one channel only, or just using TT and TE spectra alone, will not be able to produce more than an indication for tensor modes. With the CORE high-precision CMB polarization measurements, we find that the full set of single-field inflationary models we have considered can be explored. If no tensor modes are detected after one of these missions, then it is very likely that inflation cannot be described by a single field that rolls to a minimum with zero cosmological constant. The alternative would then be more complicated models, such as chaotic inflation with an unusually small p ($p \lesssim 0.01$), models with multiple fields, string models, or models with extra dimensions.

Experiment	Chan.	FWHM	$\Delta T/T$	$\Delta P/T$
WMAP	40	$28'$	8.2	11.6
$f_{\rm sky} = 0.65$	60	$21'$	11.0	15.6
	90	$13'$	18.3	25.9
Planck	44	$23'$	2.7	3.9
$f_{\rm sky} = 0.65$	70	$14'$	4.7	4.7
	100	$9.5'$	2.5	4.0
	143	$7.1'$	2.2	4.2
	217	$5.0'$	4.8	9.8
	353	$5.0'$	14.7	29.8
CORE	40	$116'$	0.032	0.047
$f_{\rm sky} = 0.65$	60	$77'$	0.018	0.039
	90	$52'$	0.0077	0.025
	135	$34'$	0.0073	0.036

Table 2: Experimental specifications for the satellite missions considered in this work. Channel frequency is given in GHz, FWHM in arcminutes, and noise in 10^{-6}.

Model	WMAP8yr	Planck 6ch	CORE
Power-law	0.45/0	1/0.98	1/1
Chaotic p=1	0/0	0.99/0.67	1/1
Chaotic p=8	0.30/0	1/0.97	1/1
Chaotic p=0.1	0/0	0.60/0	1/1
SSB ($N_e = 47 - 62$)	0/0	0.78/0.09	1/1

Table 3: Percentage of models in agreement with the WMAP observations and with an IGW background detectable at $2\sigma/5\sigma$ confidence levels by the experimental configurations listed in Table 2.

5.1.3 New Part

5.1.4 Preamble

The following text – or a polished version thereof – needs to be slotted into the version circulated by Pedro. Motivated by the news that the people on the panel are all astronomers, who might not know what an inflaton is, we think it is imperative that the conceptual and observational successes of (simple) inflation are clearly explained before diving straight into considerations of models. It seems prudent to (0) Explain the idea of inflation briefly as an accelerating phase in the expansion of the universe which requires an exotic origin (akin to dark energy), and introduce the idea of a scalar field in a potential without specialising the potential further (1) highlight the observational successes of (simple) inflationary models (2) say why the tensor measurement is a crucial and unique signal in moving beyond generic predictions of the paradigm to pinning down the physics (3) make model independent statements about what we would learn from the tensor measurement.

The reference list is also rather selective - it seems in particular to ignore Baumann

Model	4ch	100GHzch	allchT+C
Power Law	1/0.97	0.99/0.30	0.81/0.02
Chaotic p=1	0.99/0.61	0.92/0	0.25/0
Chaotic p=8	1/0.96	0.99/0.16	0.81/0
Chaotic p=0.1	0.50/0	0/0	0/0
SSB ($N_e = 62 - 47$)	0.77/0.07	0.36/0	0/0

Table 4: Planck Only. Percentage of models in agreement with the WMAP observations and with a GW-background detectable at $2\sigma/5\ \sigma$ by the Planck experiment in function of the channels available for cosmology. The $T + C$ does not include the polarization channels but just the temperature and the cross temperature-polarization spectrum.

et al, where a large number of theorists around the world, including a big fraction from Europe, collaborated to produce a document which is a very current theoretical consensus on inflation. Other than this work, it seems sensible to highlight more the work of experimental (CMB) collaborations more than is done currently, as well as the foundational theory papers on inflation.

the numbers will change: only got tonight the first foreground numbers...

The standard Big Bang cosmology is fantastically successful at explaining the basic characteristics of the observed universe. This has been further highlighted by the avalanche of cosmological data in the past decade.

However, the standard Big Bang cosmology leaves open key conceptual puzzles, including the flatness problem, the horizon problem and the origin of perturbations. Inflationary cosmology elegantly solves all of them by the same mechanism.

something about the fact that inflation is really a paradigm with many models some more complicated than others, with deep links to fundamental physics

Since inflation happened in the very early universe, observational tests of inflation offer a window at extremely high energy scales: the physics of inflation is far out the reach of terrestrial experiments. Thus cosmological tests of inflation offer a unique opportunity to learn about ultra-high energy physics.

The simplest inflationary scenarios where inflation is driven by a single field make the following observational predictions:

- 1. Flat geometry.
- 2. Gaussianity of the primordial fluctuations.
- 3. Nearly but not exactly scale-invariant power spectrum of fluctuations
- 4. Adiabaticity
- 5. Super-horizon fluctuations.
- 6. Stochastic background of gravity waves.

Current measurements confirm predictions 1 to 5 at the % level. **maybe quantify and report numbers or just add refs**. However no present or planned experiment is expected to be able to address point 6.

say something of why we can't forget 6 and just confirm inflation based on 1 to 5.

Inflation so far is in essence a paradigm; items 1–5 are generic predictions of that paradigm. To go beyond this generic picture and actually test the physics of inflation (and thus Grand Unified Theory–scale physics) requires the unique "smoking gun" signature provided by point 6. By measuring or constraining point 6 it is possible to start quantitatively ruling in or out specific models i.e. implementations of inflation and thus shed light on the specific connections to the underlying physics.

say something about non simplest models, which type of experiments will test them must that be cmb polarization or would it be something else happening independently? We can indicate that for more complicated models there will be other observational signatures : non gaussianity, running, etc. which can be addressed by different type of experiments not necessarily only a cmb polarization one

stress the importance of being model independent, given the uncertainty in model space we have at the moment

5.1.5 Model-independent expectations for inflationary gravitational waves

We propose to replace the current model dependent discussion in the draft proposal, in particular the highly prior dependent section on the "fraction of inflationary models" with the following model independent considerations

In this section we focus our discussion on a generic and model-independent connection between the expectations for inflationary gravitational waves from the simplest models of inflation (which have passed a larger number of observational tests) and the ultra-high energy physics of the inflationary era. In the

next section we survey some of the leading models of inflation an indicate their predictions for CMB observable and their accessibility by COrE.

Crucial clues about the mechanism of inflation tied to B-mode polarization are:

1. The energy scale of inflation.
   The measurement of the amplitude of the scalar power spectrum implies the following relation between the energy scale of inflation $V^{1/4}$ and the tensor to scalar ratio on CMB scales r:

$$V^{1/4} = 1.06 \times 10^{16}\ \mathrm{GeV} \left(\frac{r}{0.01}\right)^{1/4} \tag{4}$$

   A tensor amplitude $r > 10^{-3}$ would demonstrate that inflation occurred at energy scales comparable to that of Grand Unification Theories (GUTs).
   some more words about what happens if not and on the importance of such a connection. what are the options for the energy scale of inflation?

2. Excursion of the scalar field driving inflation.
   Inflation requires a form of stress-energy which sources a nearly constant Hubble parameter. This can arise via a truly diverse set of mechanisms with disparate phenomenology and varied theoretical motivations. It is, however, possible to characterize, in a model-independent way, single field models of inflation, including "hybrid" models where, although more than one field is involved, the generation of primordial perturbations is still governed by a single scalar field.

   It has been shown that in these cases there is a model-independent relation between the excursion of the field during inflation ($\Delta\phi$) and the amplitude of tensor modes. This is a generalization of the well known Lyth bound [**?**].

$$\frac{\Delta\phi}{m_{\rm Pl}} \sim 0.2 \left(\frac{r}{0.01}\right)^{1/2} \quad \text{for} \quad \frac{\Delta\phi}{m_{\rm Pl}} \ll 1, \tag{5}$$

$$\frac{\Delta\phi}{m_{\rm Pl}} \sim 4\, r^{1/4} \quad \text{for} \quad \frac{\Delta\phi}{m_{\rm Pl}} \sim 1 \tag{6}$$

   where $m_{\rm Pl} = 1.2 \times 10^{19}$ GeV denotes the Planck mass. The second line is a fit to the relation shown in Fig. 4.

Fig. 4 shows extracts from a 2-million point Monte-Carlo simulation of the inflationary flow equations (adapted from [**?**]). In this approach one starts from Hamilton-Jacobi formulation of inflationary dynamics, expressing the Hubble parameter directly as a function of the field ϕ. Then one reformulates the exact dynamical equations for inflation as an infinite hierarchy of flow equations described by the generalized Hubble Slow Roll (HSR) parameters. In practice one has to truncate the infinite hierarchy at some finite order. Secondly, the choice of slow roll parameters for the Monte-Carlo process necessitates the assumption of some prior ranges. Fortunately the results of the simulations do not depend strongly on these choices once known observational constraints (on n_s and $dn_s/d\ln k$) are imposed. This observation is what makes the conclusions of this section model-independent. While the results from these simulations cannot be interpreted in a statistical way, they show that models do not cover the observable parameter space uniformly and they show significant concentrations of points with significant tensor/scalar ratio.

From these considerations, it is clear that a value of $r > 10^{-3}$ would imply that inflation occurred at energy scales comparable to GUT scales and that there was a super-Planckian field variation. Therefore $r \sim 10^{-3}$ is a natural target for a CMB polarization experiment. An experiment that can detect $r > 10^{-3}$ will be able to discriminate between small field and large field models. The implications for such results can be understood as follows.

At a phenomenological level, an inflationary model consists of an effective action for one (or more) scalar fields, together with couplings of those scalars to known particles. A more fundamental description of the same system would involve a "top down" derivation of this phenomenological effective action, which is consistent with our understanding of quantum field theory and gravity. Inflation is thus sensitive to the physics that unifies quantum mechanics and gravity: the ultraviolet completion of gravity.

HVP to LV: the following is WAY too complicated to explain in a proposal to astronomers. I think already using the word "action" we crossed a certain line

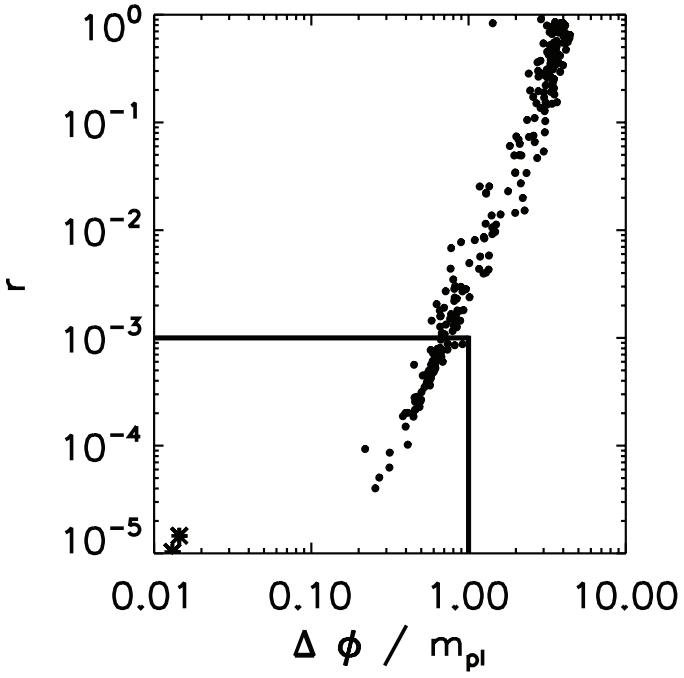

Figure 4: The absolute value of the range traversed by the scalar field ϕ over the final 55 e-folds of inflation, $\Delta\phi$, plotted against the tensor-to-scalar ratio r. Points are taken from 2 million Monte-Carlo realizations of the generic behavior of the Hubble parameter during inflation. Planck priors have been applied to n_s and $dn_s/d\ln k$, assuming a WMAP 7 LCDM model and imposing at least 55 e-foldings. Note that for $r > 10^{-3}$ all models are large field ($\Delta\phi/m_{\rm Pl} > 1$).

In this approach all inflationary model-building can be classified in two classes depending on the symmetries in the ultraviolet (UV) limit of the underlying particle theory. In particular the two cases are: approximate shift symmetry for the inflaton under which $\phi \to \phi + const$ or lack of it.

In the absence of shift symmetry, it has been shown (e.g., [**?**] and references therein) that only small field inflation ($\Delta\phi/m_{Pl} << 1$) can be supported. Thus in this case one expects $r << 10^{-3}$ and therefore unaccessible even for an ideal experiment.

In the presence of shift symmetry the system can robustly support large-field inflation [**question for discussion: how contrived is it to have small field in this case?**]. In this case $\Delta\phi/m_{\rm Pl} > 1$ arises and thus values $r > 10^{-3}$ detectable by COrE.

taken from Baumann verbatim: Such an experiment has the potential to probe important aspects of the scalar field space and the symmetry structure of quantum gravity, and to distinguish very different mechanisms for inflation.This is an astonishing opportunity.

5.1.6 Specific and/or non-simplest models

to be written if needed

5.1.7 Conclusions

The measurement of a primordial gravitational wave contribution to cosmological fluctuations is the "holy grail" of CMB measurements. A detection of primordial tensor perturbations $r > 10^{-3}$ would probe physics at an energy that is a staggering twelve orders of magnitude larger than the center-of-mass energy at the Large Hadron Collider. Of equal importance is the fact that a detection or constraint on the tensor-to-scalar ratio r at this level will answer a fundamental question about the range $\Delta\phi$ of the scalar field excursion during inflation as compared to the Planck mass scale. The quantity $\Delta\phi/m_{\rm Pl}$ is sensitive to the physics behind inflation, including the ultraviolet completion of gravity.

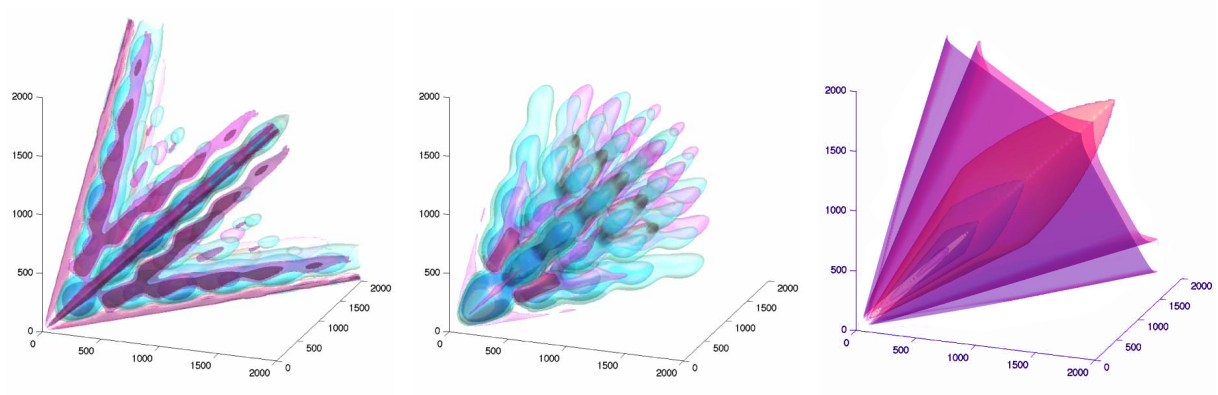

Figure 5: Distinct fingerprints of CMB bispectra $b_{l_1 l_2 l_3}$ plotted with positive (cyan) and negative (magenta) isocontours [66, 38]. From left to right, these are the local model (e.g. multifield inflation), equilateral model (e.g. DBI inflation) and cosmic strings.

5.1.8 Non-Gaussianity Wandelt, Matarrese,...

The study of primordial non-Gaussianity (NG) in the CMB has emerged as a powerful new probe of the origin of cosmic structures in the very early Universe and their subsequent evolution (see, for example, reviews in [32, 33, 34, 35, 36]). It is already the most stringent test of the standard model of inflation, the canonical slow-roll single field model, which predicts negligible primordial non-Gaussianity [41, 40]; the COrE satellite would take this confrontation to a new level, testing Gaussianity to around one part in 10^5. However, there are many alternative inflationary scenarios for which an observable non-Gaussian signal is quite natural, including models with multiple fields, interactions, non-canonical kinetic energy, or remnants of a pre-inflationary phase. There are also more exotic paradigms which can create NG with cosmic (super-)strings [37, 38] or a contracting phase with a subsequent bounce [39]. Each of these scenarios leaves a distinct NG fingerprint, essentially the "shape" of the higher order correlators. This fingerprint can break the degeneracy between the many different inflationary models which are compatible with the CMB power spectrum alone. It can also be robustly distinguished from the late-time or spurious NG fingerprints left by weak lensing, foregrounds and instrumental noise. Therefore, probing primordial NG is a direct test of physics beyond the simplest models of inflation, while offering the prospect of dramatic new insight into fundamental physics.

Non-Gaussianity is typically characterised by the parameter $f_{\rm NL}$, which is the amplitude of the three-point correlator or bispectrum for the so-called "local" model (the best-motivated case which we will describe below). The equivalent amplitude parameter for the local four-point correlator or trispectrum is $g_{\rm NL}$, supplemented by a second parameter $\tau_{\rm NL}$ (for single-field inflation, we have $\tau_{\rm NL} = (6f_{\rm NL}/5)^2$, but not in general). Inflation predicts negligible primordial NG ($f_{\rm NL} \ll 1$) if the following minimal conditions are satisfied [42]: i) a single field is responsible for driving inflation and generating the quantum fluctuations which are stretched on superhorizon scales to become the seeds for structure formation; ii) such a field has canonical kinetic energy so that its fluctuations propagate at the speed of light; iii) the inflaton obeys slow-roll, that is, it evolves slowly relative to the Hubble timescale; iv) all pre-inflationary state information has been erased during inflation. The violation of any of the above conditions can lead to the generation of a large detectable non-Gaussian signal. Each physical effect produces its own recognizable fingerprint (see fig. 5).

Models with field interactions generate "local" primordial NG which peaks in "squeezed" triangles (see, e.g., [57, 58, 59, 60]); models with non-canonical kinetic term [45] (as, e.g., DBI [46] and ghost inflation [47]) generate "equilateral" NG, while trans-Planckian effects generate NG which peaks for "folded/flattened" triangles; inflationary models violating slow-roll can generate more complicated shapes (see, e.g., [50, 51, 52]). A linear combination of these shapes can also be realized [48]. All these models can naturally predict value of $f_{\rm NL} \gg 1$ and whether the different shapes are observationally distinguishable can be determined by their cross-correlations, reducing the search categories [66]. Important tests of

inflation include the following: • *A detection of any such primordial signal would rule out all standard slow-roll models of single-field inflation.* • *Even more striking is the fact that a detection of local non-Gaussianity would rule out all classes of single-field (slow-roll) inflationary models* [54]. • *Consistency conditions between the bispectrum and trispectrum which can be used to rule out standard multifield inflation* $\tau_{\rm NL} \geq (6f_{\rm NL}/5)^2$ [58]. Beyond these special cases, general estimators have now been developed to efficiently search for arbitrary shapes in the CMB data, allowing *any* model or mechanism to be directly tested [68]. Another interesting prediction of various non-standard models of inflation is that the non-linearity parameter $f_{\rm NL}$ which can have a significant scale-dependence, parametrized in terms of a running NG index $n_{\rm NG}$ as $f_{\rm NL} = f_{\rm NL}(k)(k/k_*)^{n_{\rm NG}}$ (see, e.g. [55, 45, 56, 60, 61, 62]).

Only a high resolution polarization CMB mission such as COrE can provide the detailed bispectrum fingerprinting to detect and distinguish the NG shapes. In fact one can show that the polarization maps contain more information about these NG fingerprints than the temperature maps (though the best constraints arise from combining the two). To construct a figure of merit to compare the predicted impact of COrE on these physical forms of NG we compare the predicted constraint volume in bispectrum space spanned by the local, equilateral and flattened bispectra. While Planck will reduce the constraint volume by a factor of 70 compared to WMAP, COrE would improve it by another factor of 50. Considering the constraint volume only based on the polarization maps (which can be used as an independent check on the temperature constraints) the improvement from Planck to COrE is a factor 950.

Moreover in the presence of a high signal-to-noise detection a satellite like CorE would be able to determine $n_{\rm NG}$ with a 1-σ uncertainty of $\Delta n_{\rm NG} \simeq$???? (for $f_{\rm NL}^{\rm local} = 50$) and $\Delta n_{\rm NG} \simeq$???? (for $f_{\rm NL}^{\rm equil.} = 50$). **Need to update these numbers based on new instrument model.**

Important further information can be obtained by estimating the trispectrum (especially in combination with the bispectrum). As before, different inflationary scenarios predict distinct trispectrum fingerprints, higher dimensional analogues of the "local" and "equilateral" shapes in fig. **??** (for a review of theoretical possibilities see, for example, ref. [53]). Despite this added complexity, general estimator methods have been developed which are tractable at COrE resolution [**?**]. The forecast precision with which local trispectrum parameters could be measured with COrE temperature data alone are $\Delta g_{NL} = 3 \times 10^4$ and $\Delta \tau_{NL} = 1 \times 10^4$, which could be improved further by using polarization data. **Need to update these numbers based on new instrument model.** A significant trispectrum measurement satisfying $\tau_{\rm NL} < (6f_{\rm NL}/5)^2$ would rule out large classes of multifield inflation models (as well as single field), necessitating a fundamental reassessment of the standard field theory picture of inflation. There are also models with a negligible bispectrum and a large bispectrum, including inflation with a parity symmetry [49] and cosmic strings [38]. In the latter case, it is clear that the trispectrum will provide a significantly stronger constraint on the string tension than the power spectrum or bispectrum [38], though it will also be efficient to search for cosmic defects NG using specially tailored methods or templates [37].

What if there is no detection of primordial NG? This would be interpreted, first, as a remarkable achievement of the standard inflation model. However, the increased sensitivity of COrE would also rule out a number of alternative scenarios whose natural parameter space result in high values of the NG parameters such as $f_{\rm NL}$, while rendering many other early universe mechanisms cosmologically irrelevant. Examples include DBI inflation models typically predicting $|f_{\rm NL}| > 5$ and competitors to inflation like ekpyrotic/cyclic models predicting measureable $|f_{\rm NL}| \sim 10^1$ [63].

"Agnostic" NG searches: The much larger number of resolved modes in the COrE data allows detailed model-independent searches for anomalies in the temperature and polarization maps, which may signal new physics. The addition of high signal-to-noise polarization information with COrE allows for significant cross-checks since any model explanations of candidate anomalies seen in temperature data can be checked against the polarization data COrE will provide. This will offer significant discovery potential for relics of physics beyond the standard model of cosmology in the early universe. In summary, the exquisite data quality expected to be delivered by the COrE-satellite together with ever more refined analyses methods will bring the investigations of primordial non-Gaussianities into a new era of precision.

Guaranteed NG as probes of dark energy: Beyond searches for primordial NG, COrE will unavoidably (and with a significance of 20 σ) detect the presence of non-Gaussian features imprinted on the CMB maps by structures in the late Universe (due to the Integrate Sachs-Wolfe/Rees-Sciama/lensing correlation). These again appear as specific fingerprints and can be exploited to yield the strongest constraints from the CMB alone on the physical properties of the dark energy. There would also be ancillary signatures of second-order gravitational effects at observational levels, testing the standard cosmology and constraining modified gravity alternatives.

[**?**].

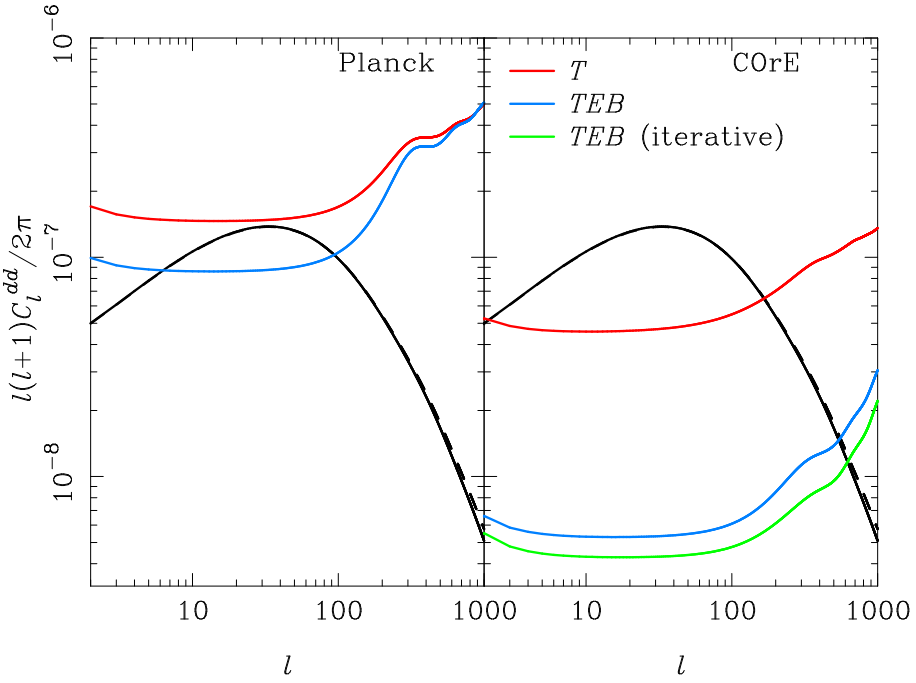

Figure 6: Reconstruction noise on the deflection power spectrum for an extended Planck mission (four surveys; left) and COrE (configuration A; right) using temperature alone (red) and temperature and polarization (blue). For COrE, we also show the approximate noise level (green) for an improved iterative version of the reconstruction estimator following Ref. [**?**]. The deflection power spectrum is also plotted based on the linear matter power spectrum (black solid) and with non-linear corrections (black dashed). **Fixme: this uses the v3 noise figures assuming the quoted sensitivities are for temperature. The configuration B reconstruction noise is similar (but a little worse).**

5.2 Full sky lensing (2) Challinor , Bucher, Lesgourgues, Perroto, Melchiorri

5.2.1 Physics of CMB Lensing

To a first approximation, the observed temperature and polarization anisotropies of the CMB offer a snapshot of the universe at $z \approx 1100$ when the helium and hydrogen recombined to render the universe transparent to the now microwave photons. According to this caricature, observing the CMB is looking at a two-dimensional screen located at the last scattering surface. The effect of later cosmic history on these anisotropies can be encapsulated into a few numbers, such the angular diameter distance and the reionization optical depth. Of course, there are a number of corrections to this simplistic depiction. Reionization erases the anisotropies on smaller scales, by an almost constant factor, and provides a big boost in the E and B polarizations at the lowest multipoles. This breaks the degeneracy between A and τ and provides a powerful lever arm to render manifest the primordial GWs through the previously discussed reionization bump.

An interesting and useful wrinkle to this picture is the gravitational lensing of the in principle almost perfectly Gaussian CMB primary anisotropies imprinted on the last scattering surface. As the photons propagate from the surface of last scatter to us today,the gravitational field induced by the intervening large-scale structures deflects them. The distortion thus introduced by gravitational lensing breaks the degeneracies of the two-dimensional projection described above and provide a new window for probing new physics, in particular neutrino masses too small to have an observable effect on what happened at and before last scatter and also dark energy which affects the evolution of the growth factor and hence the amplitude and shape of the lensing spectrum.

While lensing studies using CMB primary anisotropies as a background conceptually have much in common with present and planned studies of weak lensing of galaxies at diverse redshifts, a number of important differences distinguish the two probes. The CMB is much farther removed in terms of co-moving distance. Hence the degree of distortion is larger and the window function peaks at higher

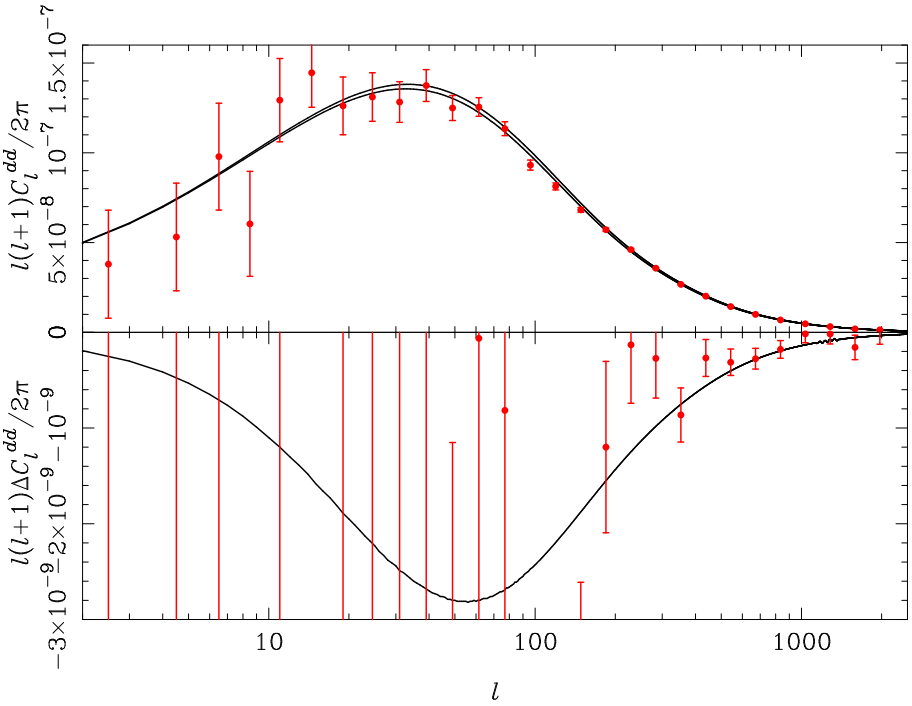

Figure 7: Simulated deflection power spectrum from COrE (configuration A) assuming an inverted hierarchy of neutrino masses with the minimum total mass allowed by oscillation data ($m_1 \approx m_2 = 0.05\,\mathrm{eV}$ and $m_3 = 0\,\mathrm{eV}$). In the upper panel, the solid lines are the theory power spectrum for this scenario (lower) and for three massless neutrinos (upper). The difference between these spectra is plotted in the lower panel illustrating how COrE can distinguish these scenarios from C_l^{dd} in the range $l > 200$. **Fixme: this uses the v3 noise figures assuming the quoted sensitivities are for temperature. Technical note: the simulation is based on simulating a Gaussian d_{lm} so ignores non-Gaussianity of the reconstruction errors. It is for $f_{\rm sky} = 0.7$. Would a linear scale for l (and linear bands) be better here to emphasize region where constraint is coming from? The plot, of course, hides the issue of degeneracies with other parameters.**

redshifts, where the density contrasts are smaller, so that linear theory calculations (improved by the best available non-linear corrections) are more reliable. Moreover, there are no issues of intrinsic alignment of galactic ellipticity to worry about. The fact that the window functions are different renders to two measurements complementary, and cross-correlations should be able to provide interesting new results.

5.2.2 Measurement and interpretation of the CMB lensing signal

As first explained by Hu and Okamoto, the CMB lensing spectrum can be reconstructed by forming optimal linear combinations of primordial CMB products of observables—that is T, E, and B—whose wavenumbers do not add up to zero. [REF] For an idealized survey, combinations are formed in harmonic space, and it is the shortest wavelength modes, at the limit of resolution of the survey, that contribute the bulk of the statistical weight. Estimators adapted to less idealized situations and the effects of possible contaminants have been extensively reviewed in the literature, and an analysis of the CMB lensing signal from the Planck data is presently underway. (See [REF] and references therein for a useful review of CMB lensing.) The main impediment to a more precise lensing reconstruction is the cosmic variance of the primary CMB anisotropies, and this is why looking at polarization provides a particularly powerful way to improve on expectations from Planck. Assuming that r is not large, virtually no B modes will be present other those originating from E lensed into B, at the expected $\approx 5\mu K \cdot$ arcmin level. Hence for a low noise experiment such as COrE, cosmic variance has a much smaller effect. This improvement is borne out in the forecasts carried out, as shown if Fig. 6. Fig. 7 shows how much COrE will improve on the expected PLANCK measurement of the lensing deflection angle power spectrum.

5.2.3 Neutrino masses as a unique probe of physics beyond the standard model

Experimental high-energy physics underwent a golden age following World War II, with the discovery of new elementary particles at an astounding rate. In fact the pace was such that theorists could not keep up, and at that time it was feared that to zoo of hadronic excitations (also interacting 'weakly'), because of the strongly coupled physics at play, might not find an elegant and astoundingly successful theoretical explanation of the sort found by Feynman, Schwinger, and Tomonoga for Quantum Electrodynamics. This fear turned out to be unfounded when building on the quark-parton ideas of Gell-Mann and Feynman, Glashow, Weinberg, and Salam put forth an electroweak field theoretic model, later shown to be renormalizable by 't Hooft and Gross, Politzer, and Wilczek through asymptotic freedom introduced QCD to explain the strong interaction on a fundamental level. In fact this theory has been so successful that high-energy experiment has not been able to keep up, and despite formidable advances in accelerator technology brought about through massive investment and ingenuity. Despite great expectations for the LHC, the fact is that accelerator experiment in the last two decades has not been able to provide any truly telling clues on how the Standard Model should be extended, despite compelling theoretical reasons that the Standard Model cannot be the last word.

One area of particle experiment stands out as a exception to the lack of recent progress–the exploration of the neutrino sector. While the standard model as first proposed implies that there are three exactly massless chiral neutrinos, an abundance of evidence has accumulated proving that neutrinos cannot be massless, for otherwise they could not undergo flavor oscillations. Starting with the work of Ray Davis and John Bahcall on the Homestake experiment, experimenters have observed neutrinos change flavor in flight over a variety of energy ranges. Solar neutrinos, atmospheric neutrinos (emanating from terrestrial cosmic ray showers), neutrinos from nuclear reactors, and neutrinos from particle beams have all been used to probe the matrix (Δm^2). The data indicate differences among the eigenvalues of this matrix: $\Delta m^2_{12} = (7.59 \pm 0.20) \times 10^{-5}\ eV^2$ to explain the solar neutrino data, and $\Delta m^2_{23} = (2.43 \pm 0.13) \times 10^{-3}\ eV^2$. The evidence for neutrino masses is overwhelming (the 2002 Nobel Prize in physics was awarded to Raymond Davis Jr. and Masatoshi Koshiba for this discovery). However neutrino oscillation experiments are not able to probe the absolute mass scale of the neutrinos, and laboratory experiments cannot (absent some unexpected breakthrough) reach the most probable mass range. If we take the mass and mixing matrix for the charged leptons and quarks as a guide, we would conclude that the most probable values for the neutrino masses would fall into two possible hierarchies: a *direct hierarchy* with $m_1, m_2 \ll m_3$ or a so called *inverted hierarchy* with $m_3 \ll m_1, m_2$. In both cases the smaller mass difference explains the solar neutrino data and the larger the atmospheric oscillation data. For $\sum m_{\nu_i}$ one expects either 0.05 eV or 0.10 eV, respectively, and smallier values are excluded although in principle the entire spectrum could be uplifted.

While it is satisfying to have a natural target for neutrino mass searches, the present laboratory experiments despite much sustained effort are not within range of this target. Measurement of the neutrino masses (or more precisely the sum of the neutrino masses) using observations of the effect of neutrinos on large-scale structure through CMB lensing can reach this target. Laboratory neutrino experiments probe neutrino masses in two ways. Firstly, one may search for neutrinoless double beta decay, which is forbidden unless neutrinos have mass. This kind of search is sensitive only to Majorana masses. Secondly, one may observe the extreme tail of the electron energy spectrum in nuclear β decay, usually of ultra-cold gaseous tritium. A massive electron neutrino alters the electron spectrum shape cutting off the quadratic tail in a linear way for the few most energetic electrons. The current limit is $m_\nu < 2\ eV(95\% confidence)$ (according to the Particle Data Group compilation), and the KATRIN experiment which has been in the planning for a decade will achieve the state-of-the art, with a projected sensitivity to $m = 0.30\ eV$ at 3σ. However at present proposals on how to qualitatively improve the β decay mass determination are lacking. The inherent obstacle is the large ratio between typical neutrino energies from nuclear β decay, (tens of KeV) and the much smaller expected neutrino mass.

The Early Universe, however, offers an alternative probe neutrino masses where there is no such hierarchy between the energies of the neutrinos involved and the expected neutrino mass. In the standard Big Bang cosmology, the CMB photons are accompanied by neutrinos, with a fixed and calculable ratio in density. If neutrinos are massless, they leave no measurable imprint on the matter power spectrum; however, massive neutrinos contribute to the power spectrum of large scales (where they behave much like cold dark matter) but not on small scales because there they behave essentially as massless particles. While at the time when the bulk of the CMB anisotropies have been imprinted ($z \approx 1100$) neutrino masses in the interesting range have virtually no effect, their effect on the matter power spectrum can be measured precisely through the lensing of the CMB anisotropies described in the previous section. While there are proposals to search for neutrino masses through weak lensing of galaxies, and also through

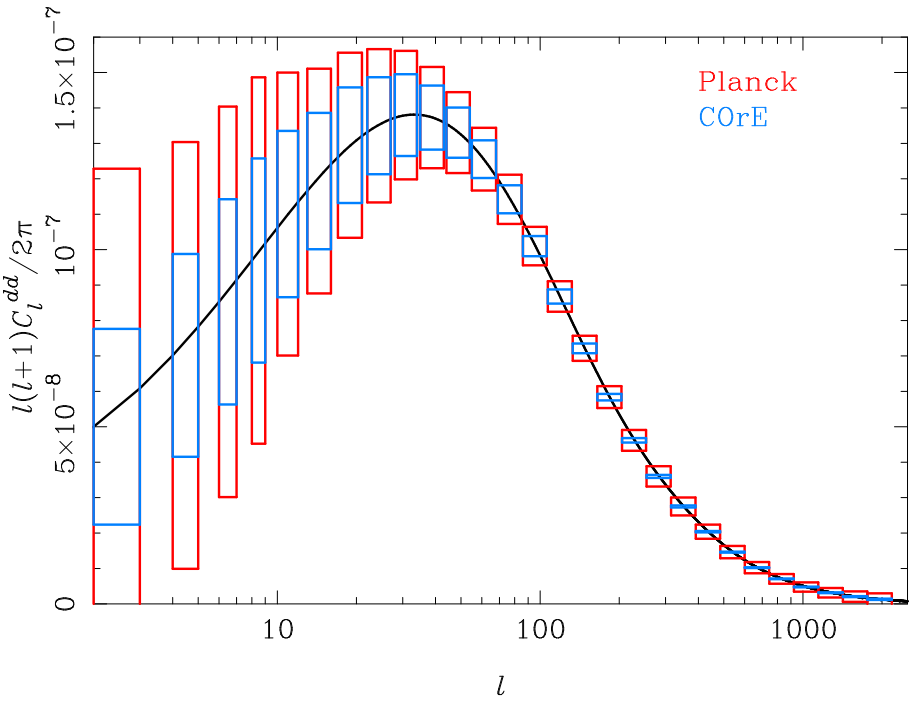

Figure 8: Bandpower errors on the estimated deflection power spectrum from an extended Planck mission (four surveys; red) and COrE (configuration A; blue) using lens reconstruction with temperature and polarization (no iteration). With COrE, the power spectrum is cosmic-variance limited to $l \approx 500$. **Fixme: this uses the v3 noise figures assuming the quoted sensitivities are for temperature.**

analyzing other large-scale structure data galaxies, the use of CMB lensing stands out for its cleanliness. Since the CMB primarily anisotropies are by far the most distant objects for which lensing can be analyzed, the role of nonlinearity is minimal and can be corrected for in a reliable way.

Under the see-saw mechanism, right-handed neutrinos, which carry no nontrivial electro-weak model quantum numbers and hence should naturally have large masses around the GUT scale M, couple to the standard model left-handed neutrinos with characteristic electroweak coupling, characterized by a mass m. In this picture, the light neutrino mass eigenstate has a explicably small mass, of order m^2/M. We see that probing the low-energy neutrino masses provides a unique means of providing experimental constraints for GUT/Planck model building. Fig. 8 illustrates show how COrE would be able to distinguish the inverted hierarchy from a model with all massless neutrinos.

5.2.4 Other aspects of CMB lensing

There is a lot that could be added here, but the section is already too long.

5.3 The Dusty Magnetized Interstellar Medium – Boulanger + Bernard

5.3.1 Role of the magnetic field

The CORE survey will uniquely address this question by mapping the structure of the Galactic magnetic field across the diffuse interstellar medium and molecular clouds. It will provide the combination of sensitivity and angular resolution required to continuously map the Galactic magnetic field within interstellar clouds, over their full extent down to the sub-parsec scales where pre-stellar cores are formed. No other experiment offers such a capability. *Planck* data will provide much information on the Galactic magnetic field on large scales, but does not have the required sensitivity to map the field in clouds. Stellar polarization observations will continue to develop, but they are intrinsically limited to a discrete set of sight lines. Ground based telescopes at sub-mm and millimeter wavelengths including ALMA will target compact sources, but they are not effective at mapping polarization from diffuse emission.

It has long been recognized that polarization studies are important for diagnosing basic properties and structure of the ISM, because they provide relatively direct access to the elusive but dynamically important magnetic field (Ostriker et al. 2003 in Turbulence and Magnetic Fields in Astrophysics). The importance of the magnetic field for interstellar matter energetics and star formation was quickly recognized, but 60 years after the discovery of the Galactic magnetic field, most questions remain quantitatively open due to the paucity of data on its small scale structure.

Star formation is at the center of much of contemporary astrophysics. Star light is our primary tracer of the structure and evolution of the universe. It is thus of central importance in astrophysics to understand how stars form? We summarize the present understanding of star formation borrowing from extensive reviews of the physics of star formation (Larson 2003 Reports on Progress in Physics, Volume 66, Issue 10, 165; McKee and Ostriker 2007 ARAA 45, 565).

Star formation occurs as a result of the action of gravity which is counteracted by thermal and magnetic pressure, and interstellar turbulence. In the diffuse interstellar medium, upstream from the formation of star forming molecular clouds, the kinetic energy from interstellar turbulence, and the magnetic energy are comparable. Both are much larger than the clouds gravitational binding energy and the gas internal energy. For stars to form, gravity must become, locally, the dominant force. This occurs where the gas turbulent energy has dissipated and matter has condensed without increasing the magnetic field flux in comparable proportions. How this occurs and with what frequency? This question is key to our physical understanding of what regulates the efficiency of star formation.

Star formation can be locally efficient, but it is, on a global scale in Galaxies, an inefficient process. To one end, the formation of bound stellar clusters such as those observed in e.g. the Antennae galaxies (Whitmore et al. 1999, AJ 118, 1551) requires that locally a large fraction ($\sim 30\%$) of the giant molecular clouds mass $\sim 10^7\,M_\odot$ is transformed into stars within a few Myr. To another end, the consumption timescale of the molecular gas in normal galaxies such as the Milky Way, $\sim 10^9$ yr, is 2 orders of magnitude larger than the dynamical timescale of giant molecular clouds (i.e. their cloud crossing time). The first scenario proposed to regulate star formation combines long cloud lifetimes, and a low star formation efficiency. In this picture, molecular clouds are prevented to collapse on large scales by turbulence and magnetic pressure, while star formation is locally controlled by the rate at which material can escape from the field lines by ambipolar diffusion (Mouschovias 1991 ApJ 373, 169; Bertoldi and McKee 1992 ApJ 395, 140).

Observations and numerical simulations are challenging this view. On the one hand, molecular cloud complexes in the solar neighborhood are found to be associated with recently formed stars. The ages of the stellar populations in these clouds are typically $< 2\,$Myr, while stellar associations with ages $> 10\,$Myr are away from molecular clouds (Hartmann et al. 2001, ApJ 562, 852). On the other hand, numerical simulations show that MHD turbulence damps within one cloud crossing time, even in the presence of a strong magnetic field (Stone et al. 1998 ApJ 508, L99). There is thus increasing consensus that the lifetime of molecular clouds is much less than has been previously assumed, and that molecular clouds form, produce stars and disperse all within a few dynamical timescales (Ballesteros-Paredes et al. 2007, in Protostars and Planets V), without the need for a continuous regeneration of turbulence over many dynamical time-scales. Within this second paradigm, molecular clouds are transient, dynamically evolving gas concentrations produced by compressive motions. Star formation occurs in sheets and filaments created by turbulent magnetic flows where gravity becomes locally dominant. Removal of magnetic support, for a sufficient fraction of the gas is necessary to account for star formation within a time span much shorter than the ambipolar diffusion timescale.

This second scenario changes the way we view star formation in two important ways: (1) the stellar initial mass function is determined primarily from cloud structure at its formation rather than from internal cloud dynamics including feedback from newly born stars, and (2) the inefficiency of star formation on a Galactic scale results from an inability of most molecular gas to form stars at all (Elmegreen 2000, ApJ 530, 277). Star formation would thus be directly linked to the formation of molecular clouds out of the diffuse interstellar medium. This stresses the importance of understanding how the interplay between turbulence and magnetic field set the initial conditions of star formation? Without CORE our understanding of the role magnetic field plays in star formation will only be addressed through numerical simulations, without direct validation from observations which could settle the open question: How gravity and with what frequency gravity initiates star formation?

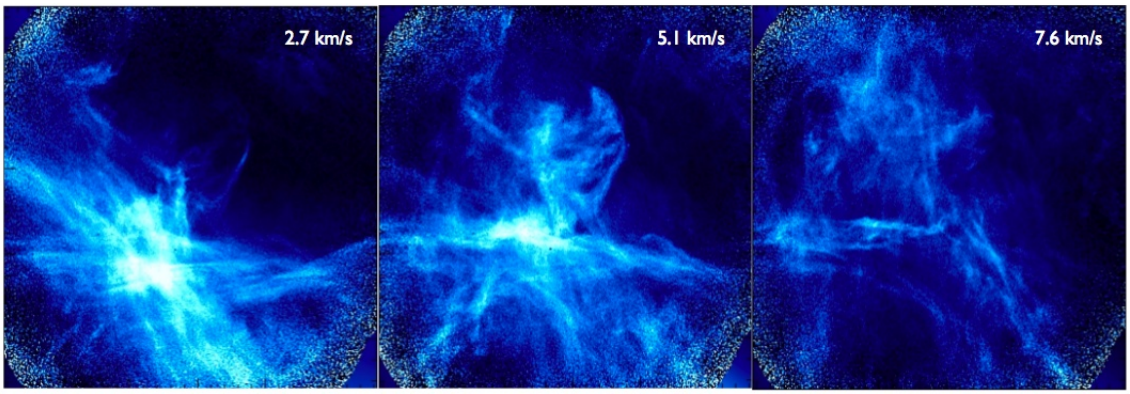

Figure 9: The CORE data will allow us to map the turbulent component of the Galactic magnetic field, and thereby to characterize the role it plays in shaping the diffuse Interstellar medium, and regulating star formation. The interstellar medium filamentary structure is illustrated here with HI spectroscopic observations obtained with the Dominion Radio Astrophysical Observatory. The three images correspond to three different velocity channels of one $4^\circ \times 4^\circ$ field (data from the Planck Deep Field HI survey, PI Peter Martin).

5.3.2 Processes driving the evolution of interstellar dust

The unique combination of spectral and spatial information provided by the CORE survey will open a new dimension to our understanding of dust, its nature and evolution within interstellar space. Understanding interstellar dust evolution is a major challenge in astrophysics underlying key physical and chemical processes in interstellar space (such as e.g. the formation of H_2), the interpretation of infrared observations from the Galaxy to high redshift galaxies, and, most importantly for CORE, the component separation in CMB polarisation experiments.

The Galactic interstellar medium is dusty. Large dust grains (size > 10 nm) dominate the dust mass. Within the diffuse interstellar medium, they are cold ($\sim 10 - 20$ K) and emit at far-IR to millimeter wavelengths. Dipolar emission from smaller dust particles is a main emission component at longer wavelengths. Both dust components are relevant to CORE observations.

"Interstellar dust is not star dust" (Draine 2009 in Cosmic Dust - Near and Far). Behind this statement lies the idea that the composition of interstellar dust reflects the action of interstellar processes, which contribute to break and re-build grains over timescales much shorter than they are renewed by stellar ejecta. If there is a wide consensus on this conclusion, the processes that drive dust evolution in space are still poorly understood.

Dust properties (size, temperature, emissivity) are found to vary from one line of sight to another within the diffuse interstellar medium and molecular clouds. These observations indicate that dust grains evolve through the interstellar medium. They can grow through the formation of refractory or ice mantles, or by coagulation into aggregates in dense and quiescent regions. They can also be destroyed by fragmentation and erosion of their mantles under more violent conditions. Dust evolution modifies the optical properties of dust grains, as well as the efficiency of the mechanism that tends to align their rotational axis along the magnetic field lines. Therefore, the polarization of the dust emission is related to the grain properties (size, shape and magnetic susceptibility), and the efficiency of grain alignment, which both depend on local physical conditions (gas density, radiation field).

The physical processes which couple dust grains and their alignment with local physical conditions make the separation of the Galactic and CMB polarisation intrinsically difficult. These physical couplings break the simplest assumption by which the spectral frequency dependence of the Galactic polarisation and its angular structure on the sky are separable. The physics of dust evolution raises several questions we need to answer to characterize the spectral dependence of dust polarisation and achieve the required accuracy in component separation for B-modes detection. Which dust components are polarized? What is the impact of dust evolution and interstellar environment on dust polarisation? How to account for grain alignment, and what is its dependence on local physical conditions? The wide spectral coverage and the large number of spectral bands are unique assets of the CORE project to answer these questions.

5.3.3 The galactic center Colafrancesco

Text

5.4 Characterizing Extragalactic Sources – de Zotti, Colafrancesco, Bonaldi + Toffolatti, Burigana

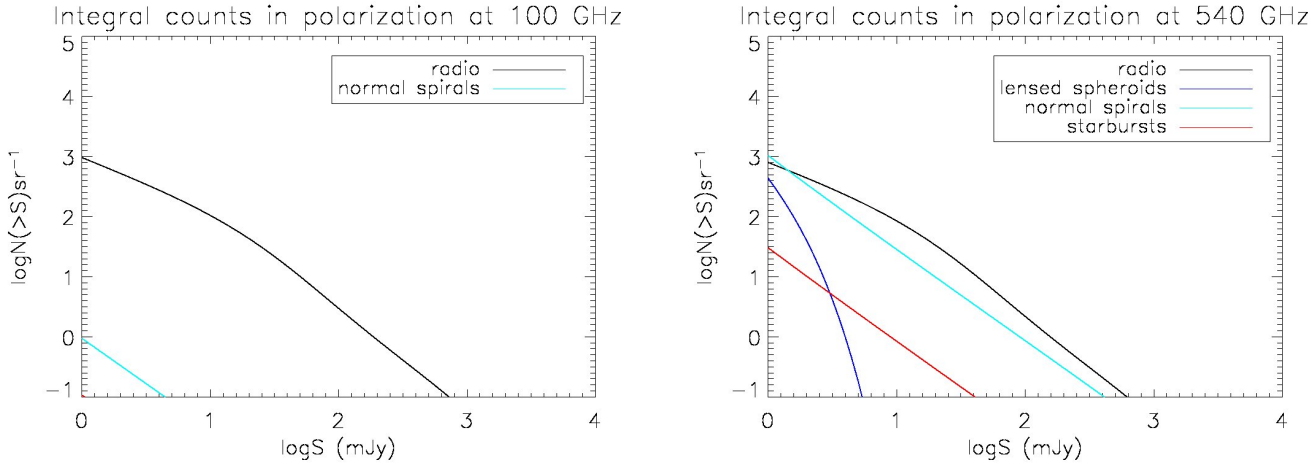

Figure 10: Expected integral counts, as a function of the polarized flux, of radio sources and of different populations of dusty star-forming galaxies, at 100 and 540 GHz.

Measurements of the polarization properties of radio sources at mm and sub-mm wavelengths provide important insights into the physical properties (and in particular into the structure of magnetic fields) of the innermost compact regions of relativistic jets in AGNs. These measurements will be also essential to assess the point sources contamination of CMB polarization maps. In fact, at high Galactic latitudes, radio sources are expected to be the main contaminant on scales $\lesssim 0.5^\circ$ up to frequencies of a few hundred GHz [de Zotti et al.1999, Tucci et al.(2004), Tucci et al.(2005)].

The only blind polarization surveys presently available are those produced by WMAP [Wright et al.(2009)]. [López-Caniego et al.(2009)] have detected in polarization, with a significance level greater than 99.99% in at least one WMAP channel, 22 objects, five of which, however, do not have a plausible low radio frequency counterpart and are therefore doubtful. We estimate that PLANCK can double the number of detections.

Most studies of polarization properties of radio sources have been carried out by following-up samples drawn from surveys in total intensity. In spite of recent efforts [Jackson et al.(2010), Agudo et al.(2010)] polarimetric data at mm wavelengths are limited, and essentially non-existent at sub-mm wavelengths.

The most extensive polarization information on complete samples selected at high radio frequencies was obtained at $\simeq 20$ GHz [Ricci et al.(2004), Massardi et al.(2008), Jackson et al.(2010)]. Radio sources are found to be significantly polarized (up to $\gtrsim$30% [Shi et al.(2010)] although the median polarization degree is approximately 3%).

Polarized emission in giant radio galaxies is an exceptional tool to understand the origin of relativistic particles, the ultra high-E cosmic rays, and magnetic fields, see e.g. [Kronberg(1994)]. In regions of the RG lobes where shocks are strongest, the inflation of the lobe is likely accelerating particles to very high energies, producing also quite flatter synchrotron spectra, see e.g. [Croston et al.(2009)], and relatively high-polarization (20-40%) intensities/degrees that could be observed with COrE in many nearby objects. In addition, Inverse Compton scattering of CMB photons in giant radiogalaxy lobes produce an SZ effect [Colafrancesco(2008)], whose spectrum (both in intensity and polarization at a level of 10-20 %) is best observed at high frequencies where it shows a maximum and a flat spectrum in the range 500-1000 GHz that could be observed with COrE in a dozen of nearby extended objects. The combination of polarized synchrotron and SZ effect in giant radio lobes offers the unique opportunity to disentangle efficiently the distribution of the relativistic electrons from that of the magnetic field and to provide, for the first time with an experiment like COrE, a complete 3D tomography of the atmospheres of these cosmic structures.

Very little is known about the polarization of dusty galaxies, that dominate the counts in total intensity above $\simeq$ 100–200 GHz, but there are indications that it is probably be weak, $\leq$ 1% [Greaves & Holland(2002), Seiffert et al.(2007)], as expected because of the complex structure of the magnetic field, resulting in very diverse polarization directions.

The spectacular increase in sensitivity of COrE, compared to PLANCK, will allow us to obtain the first large sample of sources blindly selected in polarization. Because of the polarized flux is, on average, a small fraction of the total flux, source confusion is far less of a problem in polarization than in total intensity. In high Galactic latitude regions where polarized diffuse emission are low, and assuming that the CMB can be efficiently removed, we find that COrE polarization surveys are expected to be confusion limited up to $\simeq$ 100 GHz. Specifically, adopting an average polarization degree of 3% for radio sources and of 1% for dusty star-forming galaxies, and using the model by [de Zotti et al.(2005)] for the former population and the model by [Negrello et al.(2007)] for the latter, we find that an rms confusion noise of 4 mJy at 60 GHz and of 1.4 mJy at 100 GHz. At higher frequencies the instrumental noise dominates.

As illustrated by Fig. 10, at 100 GHz we expect to detect the polarized flux of $\simeq$ 170 radio sources per sr above the 5σ confusion limit of $\simeq$ 7 mJy. At higher frequencies also the polarized dust emission from dusty star-forming galaxies should be detectable. Under the above assumptions, we have $\simeq$ 15 radio sources and $\simeq$ 6 normal spiral galaxies per sr with polarized flux larger than the 5σ detection limit of $\simeq$ 21 mJy at 540 GHz in the case of the Configuration A (or $\simeq$ 33 mJy at 555 GHz in the case of the Configuration B).

5.4.1 The origin of magnetic fields

Text

5.4.2 Physical properties

Text

5.4.3 Lensed sources Blain

Text

5.5 Challenging the cosmology paradigm (1) Bucher

Text

5.5.1 Parameters Melchiorri, Battye, Garcia- Bellido

Parameter uncertainty	Planck	COrE config. A		COrE config. B	
$\sigma(\Omega_b h^2)$	0.00011	0.000033	(3.3)	0.000034	(3.3)
$\sigma(\Omega_c h^2)$	0.00087	0.00036	(2.4)	0.00037	(2.4)
$\sigma(H_0)$	0.0039	0.0014	(2.8)	0.0014	(2.8)
$\sigma(\tau)$	0.0040	0.0022	(1.8)	0.0022	(1.8)
$\sigma(n_s)$	0.0027	0.0014	(1.9)	0.0014	(1.9)
$\sigma(10^{10} A_s)$	0.18	0.09	(2.0)	0.01	(2.0)

Table 5: 68% c.l. errors on cosmological parameters. In the () we report the improvement factor (see text) in the confidence level for the corresponding COrE configuration respect to Planck.

In this section we forecast the constraints achievable on several cosmological parameters from the COrE satellite considering the two different configurations. In Table 5, we report the future constraints on the parameters of a "minimal" cosmological model. Together with the standard deviations on each parameter we also report, for the two COrE configurations, the improvement factor for each parameter defined as the ratio σ_{Planck}/σ where σ is the confidence level on the parameter expected from the corresponding COrE configuration and σ_{Planck} is the constraint from Planck. As we can see in the Table,

Parameter uncertainty	Planck	COrE config. A		COrE config. B	
$\sigma(\Omega_b h^2)$	0.00017	0.000047	(3.6)	0.000049	(3.6)
$\sigma(\Omega_c h^2)$	0.0022	0.00072	(3.1)	0.00073	(3.1)
$\sigma(H_0)$	0.011	0.0033	(3.3)	0.0034	(3.3)
$\sigma(\tau)$	0.004	0.0022	(1.8)	0.0022	(1.8)
$\sigma(n_s)$	0.0056	0.0024	(2.3)	0.0025	(2.3)
$\sigma(10^{10} A_s)$	0.23	0.11	(2.1)	0.011	(2.1)
$\sigma(N_{eff})$	0.14	0.043	(3.3)	0.044	(3.3)

Table 6: 68% c.l. errors on cosmological parameters in the case of extra background of relativistic particles N_{eff}. In the () we report the improvement factor (see text) in the confidence level for the corresponding COrE configuration respect to Planck.

Parameter uncertainty	Planck	COrE config. A		COrE config. B	
$\sigma(\Omega_b h^2)$	0.00016	0.000048	(3.3)	0.000048	(3.3)
$\sigma(\Omega_c h^2)$	0.0009	0.00036	(2.5)	0.00036	(2.5)
$\sigma(H_0)$	0.0046	0.0015	(3.1)	0.0016	(3.1)
$\sigma(\tau)$	0.0040	0.0022	(1.8)	0.0023	(1.8)
$\sigma(n_s)$	0.0053	0.0023	(2.3)	0.0024	(2.3)
$\sigma(10^{10} A_s)$	0.19	0.1	(1.9)	0.1	(1.9)
$\sigma(Y_p)$	0.0083	0.0027	(3.1)	0.0027	(3.1)

Table 7: 68% c.l. errors on cosmological parameters considering variations in the primordial ^4He fraction abundance Y_p. In the () we report the improvement factor (see text) in the confidence level for the corresponding COrE configuration respect to Planck.

the COrE satellite will improve by a factor ~ 3 the constraints on the baryon density, H_0 and θ_s, while the constraints on parameters as n_s and τ are improved by a factor ~ 2. We have also considered, as additional parameters, the possibility of an extra background of relativistic particles, N_ν^{eff} and the Helium abundance Y_p. An additional background of relativistic (and non-interacting) particles can be parametrized by introducing an effective number of neutrino species N_ν^{eff}. This additional background changes the CMB anisotropies through time variations of the gravitational potential at recombination due to the presence of this non-negligible relativistic component (the so-called early Integrated Sachs Wolfe effect). The main consequence is an increase in the small-scale CMB anisotropy (see e.g. [24]). As recently shown by several authors ([27], [28], [29], [31]) the small scale CMB anisotropy spectrum can provide a powerful method for accurately determining the primordial ^{4}He abundance. Current astrophysical measurements of primordial fractional abundance $Y_p =^4 He/(H +^4 He)$ can be contained in the conservative estimate of $Y_p = 0.250 \pm 0.003$ (see e.g. [30]). In Tables 6 and 7 we report the future constraints on the parameters of a cosmological model that allows for variations in N_ν^{eff} and Y_p respctively. As we can see, COrE is expected to improve the constraints on these parameters by ~ 3 confidence levels.

5.5.2 Neutrino text from alessandro

Parameter uncertainty	Planck	COrE config. A		COrE config. B	
$\sigma(\Omega_b h^2)$	0.00012	0.000033	(3.6)	0.000034	(3.6)
$\sigma(\Omega_c h^2)$	0.0010	0.00046	(2.2)	0.00046	(2.2)
$\sigma(H_0)$	0.011	0.0044	(2.5)	0.0045	(2.5)
$\sigma(\tau)$	0.0040	0.0023	(1.7)	0.0023	(1.7)
$\sigma(n_s)$	0.0029	0.0015	(1.9)	0.0015	(1.9)
$\sigma(10^{10} A_s)$	0.19	0.1	(1.9)	0.011	(1.9)
$\sigma(\Sigma m_\nu)$	0.088 [eV]	0.033 [eV]	(2.7)	0.034 [eV]	(2.7)

Table 8: 68% c.l. errors on cosmological parameters including the possibility of a neutrino mass. In the () we report the improvement factor (see text) in the confidence level for the corresponding COrE configuration respect to Planck.

The detection of the absolute mass scale of the neutrino is one of the major goals of experimental particle physics. However, cosmology could provide an earlier, albeit model-dependent, detection. CMB power spectra are sensitive to a total variation in neutrino mass eigenstates Σm_ν (see e.g. [15, 16]) but can't discriminate between the mass of a single neutrino flavour (see e.g. [17]) because of degeneracies with other parameters. Inclusion of massive neutrinos increases the anisotropy at small scales because the decreased perturbation growth contributes to the photon energy density fluctuation. Moreover, gravitational lensing leads to smoothing of the acoustic peaks and enhancement of power on the damping tail of the power spectrum; the amount of lensing is also connected to the neutrino mass (see e.g.[18]).

Current oscillation experiments provide essentially two mass differences for the neutrino mass eigenstates: $\Delta m^2_{solar} \sim 8 \times 10^{-5} eV^2$ and $\Delta m^2_{atm} \sim 2.5 \times 10^{-3} eV^2$ (see e.g. [19] and references therein). An inverted hierarchy in the neutrino mass eigenstates predicts a lower limit to the total neutrino mass of about $\sum m_\nu \geq 0.10 eV$ while a direct hierarchy predicts $\sum m_\nu \geq 0.05 eV$. The goal for CMB experiments is therefore to have a sensitivity better than $\sum m_\nu \leq 0.10 eV$ for possibly ruling out the inverted hierarchy and better than $\sum m_\nu \leq 0.05 eV$ for a definitive detection of neutrino mass.

We have therefore performed a Fisher matrix analysis to forecast the future constraints from the COrE satellite. In Table 8 we report the future constraints achievable on cosmological parameters including the neutrino mass $\sum m_\nu$ from the two configurations of the COrE satellite. We also report the constraints expected from the Planck satellite. Together with the standard deviations on each parameter we also report, for the two COrE configurations, the improvement factor for each parameter defined as the ratio σ_{Planck}/σ where σ is the confidence level on the parameter expected from the corresponding COrE configuration and σ_{Planck} is the constraint from Planck.

5.5.3 Primordial magnetic fields Rubino-Martin, Finelli + Giovannini?

Synchrotron emission and Faraday Rotation (FR) measurements provide increasing evidence that the largest (and early) astrophysical systems in the Universe are pervaded by measurable magnetic fields: galaxies, galaxy clusters, Ly-α forest and intergalactic and intercluster regions [1, 2]. These observational facts suggest that galactic fields of the order of 10 μG are not reached in galaxies through standard galactic dynamos and that we should look for earlier magnetogenesis mechanisms.

Primordial magnetic fields (hereafter PMF) generated in the early Universe are a possible explanation of those large scale magnetic fields [3, **?**, **?**, 7]. If that is the case, an important consequence of those pre-recombinational magnetic fields is that they could produce detectable features in the CMB anisotropies.

Current limits on PMF have been derived from three kinds of datasets: CMB, nucleosynthesis and large scale structure. From all these three sources of information it is temptative to summarize that magnetic fields below few nG could be present at the last scattering surface.

CORE will provide data with unprecedent accuracy, which could allow the possible detection of PMF based on different mechanisms:

- The scalar, vector and tensor contributions to CMB anisotropies of inhomogeneous modes generated by a stochastic background of PMF leaves uniques features in the angular power spectrum of the polarization. In particular, the BB signal induced by vector perturbations has a characteristic peak around $\ell \sim 2000$, which is only slightly dependent on the initial PMF spectrum (n_B), and has a shape very different from either the inflationary gravitational waves or the lensing signal [8, 9]: as can be seen from the left panel of Fig. 1, CORE has the capabilities to probe such BB signal. CORE will improve constraints based on either present CMB or future Planck data [**?**], bringing the constraints below the nG threshold, as can be seen from the right panel of Fig. 1.

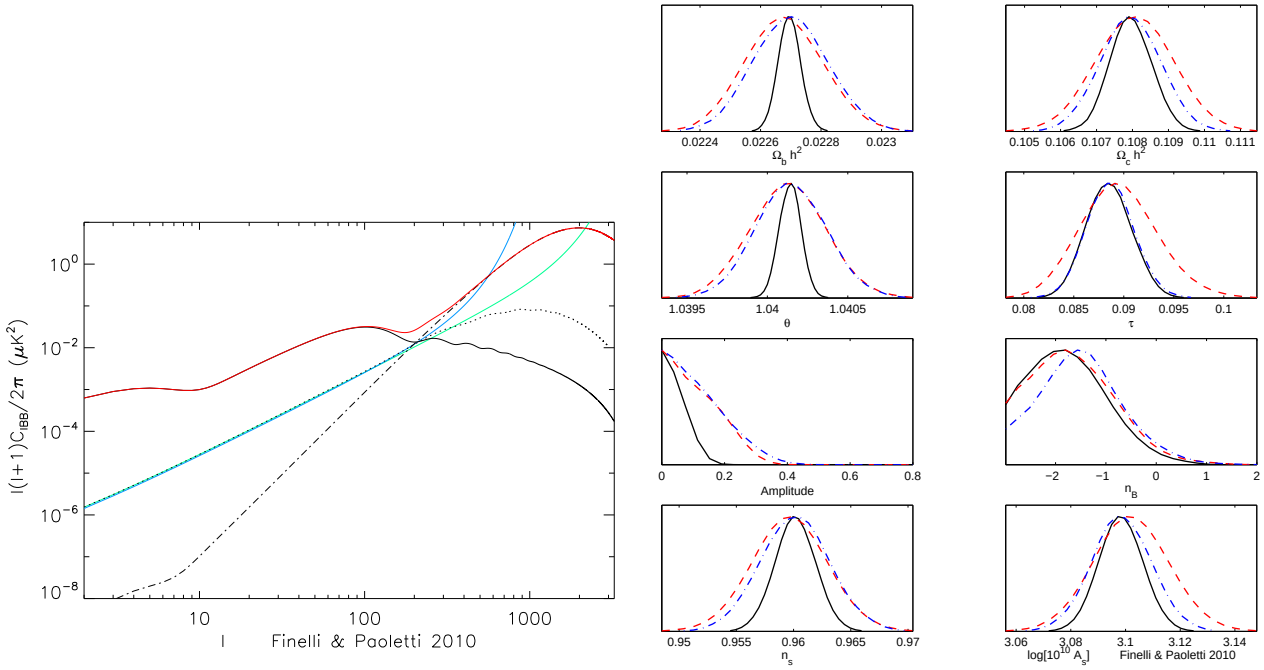

Figure 11: Left Panel: Comparison among the BB signals generated by the vector contribution due to PMF - $n_B = -2.5$ and $B = 10\,\mathrm{nG}$ -, by the inflationary gravitational waves and by the lensing. Right Panel: comparison between constraints by CORE and by Planck.

- The lowest CORE frequency channel plays a crucial role in constraining the existence of PMF by means of the impact of the induced Faraday rotation of the CMB polarization maps. This effect can be observed both on small scales (for stochastic PMF) and large scales (for homogeneous PMF). Faraday rotation alters the overall polarization pattern by mixing E- and B-modes in a characteristic frequency-dependent behavior. The effect is usually described in terms of the (time-independent) parameter F, given by

$$F = 0.7\Big(\frac{B}{10^{-9}\ G}\Big)\Big(\frac{10\ GHz}{\nu}\Big)^2. \tag{7}$$

For the case of stochastic PMF, a BB power spectrum signal is generated, which scales as F^2 [10]. This signal can be used to constrain the amplitude, coherence scale and the shape of the primordial magnetic-field power-spectrum (e.g. [11]). However, for the case of homogeneous PMF, the Faraday rotation induced by such field will produce, in addition to the BB signals, a non-zero EB and TB correlations (e.g. [12, 13]), which will now scale as F. Therefore, CORE would allow to improve the Planck constraints significantly, reaching also in this case sensitivities to PMF smaller than 1 nG.

5.5.4 Reionization history of the Universe – Burigana

One of the most striking contributions of the WMAP space mission was its measurement of the reionization optical depth, τ of the microwave photons through its characterization of the E mode polarization on very large angular scales. According to their 7yr analysis [Larson et al.(2010)], the current uncertainty on τ is $\simeq \pm 0.015$, almost independently on the specific model considered. Under various hypotheses (simple ΛCDM model with 6 parameters, inclusion of curvature and dark energy, of different kinds of isocurvature modes, of neutrino properties, of primordial helium mass fraction, or of re-ionization width) the best fit of τ lies in the range 0.086–0.089. On the other hand, allowing for the presence of primordial tensor perturbations or (and) of a running in the power spectrum of primordial perturbations the best fit of τ goes to 0.091–0.092 (0.096). *Planck* will certainly put new light on this topic thanks to its high sensitivity to E mode polarization, but this underlines the relevance of carrying out a combined analysis of the re-ionization of the Universe and of primordial tensor perturbations, firmly possible only through high accuracy measurements of both E and B modes. Re-ionization results from ionizing radiation emitted by very first structures formed in the high-redshift Universe – either by very massive stars or by quasars – and a better characterization of the full re-ionization history as a function of redshift would provide important clues for understanding the scenarios of structure formation and radiative feedback processes [Burigana et al.(2008)] resulting in a different suppression of star formation in low-mass haloes. The precise polarization data that COrE will provide at very low multipoles will be invaluable to this endeavor. The principal component analysis can be used to provide model-independent constraints on the re-ionization history of the Universe [Mortonson & Hu(2008)] from CMB polarization data at low multipoles. Furthermore, the COrE resolution up to some arc-minutes will allow to constrain alternative (double-peaked or very high redshifts) re-ionization models, invoking non-standard processes such as evaporation of mini-blackholes or particle decays/annihilations, manifesting themselves also at high multipoles [Naselsky & Chiang(2004)]. Analogously, COrE will permit to constrain key parameters of patchy reionization, such as the duration of the patchy epoch or the mean bubble radius [Dvorkin & Smith(2009)].

5.5.5 Topological defects Battye et al.

The end of inflation can be induced by a phase transition and this can lead to additional observational signatures; such models are known as Hybrid Inflation models [69]. Topological defects may form during this phase transition if the vacuum manifold has non-trivial topology. Cosmic strings created during the breaking of a $U(1)$ symmetry or textures from the breaking of a global $O(N)$ symmetry are the most commonly studied, although more complicated defects such as semi-local strings are also possible. The amplitude of CMB anistropies created by the defects is $\sim (\eta/M_{\rm pl})^2$ which is naturally $\sim 10^{-5}$ if the symmetry breaking transition is near the GUT scale, $\eta \sim 10^{16}$GeV. Often inflationary models that produce topological defects predict low values of r and hence their detection presents another potential window on the epoch of Grand Unification.

An important feature of defect models is that they will create B-mode polarization and the expected spectrum will be significantly different that from due to the gravitational wave background created during inflation. This is because the perturbations created by the defects create a superposition of scalar-vector-tensor modes with a fixed amplitude and, in particular, the contribution from vector modes can have a similar, or larger, amplitude to that from scalar modes. The detailed spectrum is an active area of research, but the main qualitative features are a bump at low ℓ due to reionization and a white noise portion rising to a peak somewhere between $\ell = 500$ and 1000.

We have performed an analysis of the prospects of detecting this background using COrE. For definiteness we will use spectra for cosmic strings computed using the Abelian Higgs model approach [70] (see ref. [71] for alternatives which would lead to different but qualitatively similar results) for which a 7-parameter (the standard 6 plus the fraction of cosmic strings) fit to the WMAP5 data yields a limit of $G\mu/c^2 < 7 \times 10^{-7}$. The simulated fit includes the standard 6 parameters, r and $G\mu/c^2$ and takes into

account residual foreground errors and the gravitational lensing background as described in ref. [72]. We find significant discovery potential for both r and $G\mu/c^2$ corresponding to a simultaneous lowering of current limits to $r < 10^{-3}$ and $G\mu/c^2 < 2 \times 10^{-8}$. Similar detection opportunities apply to other defect models such as textures.

5.6 Scientific requirements (3) PdB, Delabrouille, Burigana

Text

5.6.1 Angular resolution

Text

5.6.2 Sensitivity

Text

5.6.3 Polarization purity & robustness

Text

5.6.4 Spectral coverage for science targets and for components separation – Delabrouille, Bonaldi, Ricciardi, Basak, Peiris,Verde, Baccigalupi, Burigana, Dickinson, Bucher

The multi-component sky

Several astrophysical emission processes contribute to the total sky brightness in the frequency domain of interest for COrE. Significant progress in the understanding of these emissions has been driven by past CMB observations. The Planck satellite has just completed its nominal sky survey. The ongoing analysis is expected to yield significant further knowledge about the sub-millimeter polarized sky.

Emission from the Galactic interstellar medium is usually split into few 'components': synchrotron, free-free, line emission from molecules, thermal emission from dust. Additional emission associated to spinning dust grains has been identified. These ISM emissions constitute the main foreground on large angular scales, where primordial CMB B-modes are expected to be detected with COrE.

Galactic and extragalactic compact objects of various types contribute a complex background of blended sources, correlated in pixel space as well as across observing frequencies. A few thousands of strong sources, can be picked out of this background (removed or masked), but the impact of the rest of faint blended sources must be taken into account in the design of COrE and its data analysis.

Among foreground emissions, some are known to be significantly polarized (at the several percent level). This is the case for synchrotron, dust, and some individual point sources. Others are weakly polarised, or unpolarized to first order. This is the case for free-free, and point source backgrounds (due to statistical depolarisation).

The total emission from Galactic and extragalactic foregrounds is significantly stronger than the target level of primordial B-modes to be observed with COrE at all frequencies. This holds even after 30% of sky is masked. Therefore, as illustrated in Fig. 12, the measurement of primordial CMB B-modes on large scales requires the ability to suppress the contamination by such foreground emission by several orders of magnitude. However, CMB polarisation from E-modes has been shown to be stronger than foregrounds on small patches [**?**].

Observing frequencies

Except for the unpolarised kinetic SZ effect, only the CMB has an emission law equal to the temperature derivative of a 2.725 K blackbody. This unique property permits, in presence of foregrounds, to identify the CMB contribution unambiguously using observations of the sky at different frequencies. This property has been used by previous experiments to validate the cosmological origin of observed sky temperature fluctuations at high Galactic latitude. This is illustrated by the WMAP team in [**?**].

The color of the polarized CMB across frequencies, however, can only be checked after contamination by polarized foregrounds has been reduced. This requires using observations at additional frequencies, used as foreground monitors. There is, at present, no external data set with enough sensitivity to clean

Figure 12: Level of emission of the various foregrounds and of polarised CMB as a function of frequency in the frequency range probed by COrE.

Figure 13: Level of emission of the various foregrounds and of polarised CMB as a function of ℓ, and the measurement of the power spectrum.

polarised emission at the level required for COrE. Hence, COrE must have channels to observe and subtract polarised foregrounds, and be left with enough clean maps to check that there is emission with the CMB color.

The quality of CMB cleaning relies heavily on the level of correlation of foreground components across channels. Perfectly correlated components can be represented with one single template. Completely uncorrelated components behave as additional noise, the level of which should be lower than the targeted sensitivity. Real life foregrounds are partly correlated across channels, and can be represented as a superposition of main templates, first or second order corrections, and residuals which are uncorrelated between observing frequencies.

A proper choice of frequency channels for COrE should comprise the following:

- A set of CMB channels, in which there is enough sensitivity to measure the CMB B-mode spectrum and check that the corresponding CMB has the appropriate colour;
- Two or three low frequency channels for monitoring polarised synchrotron emission (one channel for synchrotron amplitude, one for pixel-dependent spectral index, and possibly one for the running of the spectral index);
- Three to six channels to monitor polarised dust (for amplitude, spectral index, and temperature of one or two dust components).

The COrE baseline design uses channels at 45, 75 and 105 GHz for synchrotron monitoring. Channels between 315 and 795 GHz monitor dust. Six channels between 135 and 285 GHz are left, to measure the CMB and face surprises in the complexity of the polarised emission of the sky, if any. This baseline is also appropriate to analyse temperature data with additional unpolarised foregrounds.

Component separation

A complete review of component separation methods is not possible here. Usual methods include:

- masking of the most contaminated regions;
- template fitting (when appropriate external templates are available);
- physical modeling and subtraction of foreground emissions (which requires detailed insight about polarisation properties of the foregrounds);
- inversion of a linear system (if the data can be modeled as a well defined linear mixture of emissions);
- blind component separation methods.

Ultimately, the COrE data analysis will make use of all methods available. At present, we simply show how the COrE design permits to measure, in a robust way, the CMB B-modes in presence of foregrounds comprising polarised synchrotron with sky-varying spectral index, a two component polarised dust emission, and a background of polarised point sources. The component separation method is based on the needlet ILC method used for temperature in [**?**]. Two separate ILC are performed on two independent sets of maps, obtained each from half of the COrE data at all frequencies. Fig. 13 shows the quality of the recovery of the CMB B-mode power spectrum with this simple technique, for $r = 5 \times 10^{-3}$, for the baseline COrE.

Comment the figures.

Forecasts

The precision with which the CMB B-mode power spectrum is measured translates into constraints on the measurement of the tensor to scalar ratio r.

5.7 Why space? (1) PdB, Jaffe

Balloon experiments such as EBEX and SPIDER along with ground-based telescopes such as PolarBear and SPT[1]) are just now reaching levels of instantaneous sensitivity with thousands of detectors in one or two frequency bands and sufficiently long integrations which give white-noise levels of $3\mu K$ per arcminute at a single frequency, arguably sufficient to reach $r \simeq 0.05$ in the absence of contaminating systematics, with angular resolutions varying from ten arcmin to one degree. These experiments have already shown us the technical feasibility of measuring the CMB with thousands of detectors.

However, the full science goals that we have outlined above require an unprecedented sensitivity to cosmological and astrophysical polarization over a wider range of angular scales and frequencies. To achieve this sensitivity in practice further requires control of systematics at a level that cannot be achieved in suborbital experiments. A satellite experiment like *COrE*is therefore a necessary next step: it will observe the full sky; it will have multiple bands over more than a decade of frequency; it will take data for very long integration times in the very quiet environment of the L2 point.

5.7.1 Full sky coverage

COrE's science goals require high sensitivity over the full sky. This will enable measurement of the reionization signal in polarization, crucial for confirmation of the last-scattering B-mode signal at medium scale. Moreover, it will build up sufficient signal-to-noise on the non-Gaussian signal, constrained by the number of independent triples (or quadruples, etc.) available. This will be crucial if we want to go beyond detection of $f_{\rm NL}$ to detailed non-Gaussian models of the higher-order moments. **Refer to figures in science sections above.**

Situated between the strongly-radiating ground and sun, suborbital experiments are highly constrained in the amount of sky that they can observe as well as the way that they can observe it: they must scan at constant to avoid rapidly-changing ground pickup whilst simultaneously avoiding the sun. Hence, these experiments can typically observe a maximum of a few thousand square degrees with only mild cross-linking of different scans, with details strongly dependent upon the location of the experiment.

5.7.2 Wide frequency coverage

In order to take advantage of the full CMB sky requires cleaning the large-scale foreground to white-noise levels on the very largest scales. The atmosphere remains a strong source of microwave emission. Although it is largely unpolarized, it adds to the photon shot noise making necessary longer integration times. Moreover, Zeeman splitting due to the Earth's magnetic field leads to both linear and circular polarization. The linear polarization may be small ($\approx$ 10nK), but the circular polarization is much larger ($\approx 10^2\mu$K), and great care must be taken to avoid conversion into linear polarization within the instrument [Keating et al., astro-ph/9710087; Hanany & Rosenkranz, astro-ph/0307052]. Another effect leading to significant polarization is the back-scattering of thermal radiation from the hot ground by the atmosphere. This component results primarily from large ice crystals (i.e., 100 – 1000 μm) in high-altitude ice clouds, often optically quite thin (along with a smaller effect from molecular scattering). Simulations demonstrate that at both the South Pole and in the Atacama desert such polarized emission will likely swamp the B mode signal [L. Pietranera et al., "Observing the CMB polarization through ice," MNRAS 346, 645 (2007)].

5.7.3 Benign environment (especially L2)

Even with highly-constrained constant-elevation scans, suborbital experiments would need to reject far sidelobes from the 250 K $\times 2\pi$ *textrmsr* ground at a level of roughly 10^{-10} to remain below the desired noise on large angular scales. From the L2 orbit proposed for *COrE*, the earth will subtend an angle of only 0.5°, reducing its emission by 10^5. Moreover, at L2 the Earth, like the sun, can be more easily shielded, limiting the emission from both to diffraction around the shielding. Temperature variations in the shielding will be converted into a polarization signal by diffraction, are similarly suppressed.

These same considerations apply to temporal variations in the ambient temperature, which can be up to several degrees per day at midlatitudes, compared to the nearly completely stable L2 environment. For *COrE*, any change in thermal loading is due to the behaviour of the cooler itself and can be strictly controlled and monitored, as well as kept to specific times during the mission.

[1]for an up-to-date list of suborbital experiments, see http://lambda.gsfc.nasa.gov/product/suborbit/su_experiments.cfm

The L2 environment also allows much longer integration times than can be achieved from balloons (even Ultra-Long Duration balloons have a limit of roughly 40 days at present) and a higher duty cycle than ground-based experiments.

Only from space can an experiment like *COrE*achieve its simultaneous goals of full-sky measurements of astrophysical polarization over a decade in frequency and an angular resolution of 6 arcmin, and μK $\cdot$ arcmin sensitivity coupled with thermal stability and 10^{-5} sidelobe rejection.

6 Mission profile proposed to achieve these objectives (2 pages) PdB, FRB

To achieve the science objectives, a surveyor with full sky coverage in 15 bands with an angular resolution of the order of few arcminutes and an integrated sensitivity of 1 μK $\cdot$ arcmin is proposed. Based on the SAMPAN and B-Pol feasibility studies and on the *Planck* and *Herschel* experience, we propose the following mission profile.

6.1 Launcher requirements.

The rejection of parasitic signals from the side lobes pick-up of the Moon, Earth and Sun emissions, together with the need of a full sky coverage, lead to the choice of an L2 orbit for *Planck*. The same applies to *COrE*. A Soyuz launcher that would take off from Kourou offers the best fare compatible with instrument requirements. In fig. 14, we present the accommodation of *COrE* inside the fairing of a dual-payload type-S bay.

6.2 Orbit requirements.

An 500000/800000 km ◄ **TBC** ► orbit around L2 (similar to Herschel) has been selected, to save payload mass, taking advantage of the lower Δv with respect to the *Planck* orbit.

The mission would last 4 years: the extended lifetime has been achieved with the use of a cryogenic system free of consumables (see § **??**). The transfer from Earth to L2 would last 2 to 4 months. The Calibration and Performance Verification Phase will last 2 months.

To achieve optimal sky coverage and redundancy (both in terms of hits per pixel and angular coverage), *COrE* will scan the sky as described in § 8.1

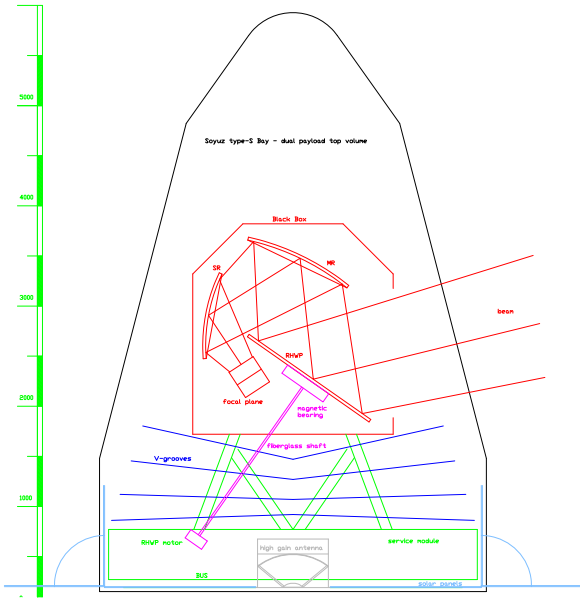

Figure 14: Fairing acomodation of *COrE*.

6.3 Ground segment requirements

The payload will host a single, very homogeneous survey instrument. The mission concept is thus very simple in terms of operations and Ground Segment. The most important operational constraint is the stability of the system for as long as possible during the mission.

Every day the instrument will simply survey the sky for 24 hours according to the predefined program, spinning at 0.5 rpm and producing a raw data-rate around 18 Mbits/s; we know from *Planck* that this can be compressed to 4.5 Mbits/s for transmission. The data will be stored on-board and will be dumped to the Earth via a high-gain antenna ◄ **TBC** ► aligned to the spin axis for 3-4 hours ◄ **TBC** ► per day, during which the spin axis will be directed to the Earth. The instrument will continue its survey during the downlink.

The high redundancy given by the nutation/precession scanning strategy will be the most powerful tool to deal with any data discontinuities and downlink problems without the requirements of fast reaction

to events as in the case of *Planck*. So the number of operations and procedures will be very limited after the end of the Calibration & Performance Verification Phase.

6.4 Special requirements

This is a cold payload ($\sim$ 30K for the telescope, $\sim 0.1K$ for the focal plane), which should be kept in the shadow of the solar panels and V.grooves for the whole mission. The satellite is a re-orientable spinner, whose spin axis will be at all times at $\lesssim 15°$ ◄ **TBC** ► from the anti-sun direction, basically pointing the earth to easy downlink communications. The re-orientation of the spin axis will be synchronized to the orbit period (a few months). ◄ **To be confirmed by orbit simulations, F. Piacentini is working on it** ►. We also require to be able to change the spin rate (nominally around 0.5 rpm) by $\pm 10\%$ at 6 months time scales, which provides a powerful check for (spin-synchronous) systematic effects.

7 Model payload to achieve the science objectives (9 pages) PdB, Maffei, Masi, Piat, De Petris, Withington

7.1 Overview of all payload elements and description of the measurement technique

Based on the exceptional results from the Planck mission and on its actual performances we are now in a better position to optimise a new satellite design. In comparison to Planck, our aim is now to increase the instrument sensitivity by a factor **[XXX]** through the use of large arrays of feedhorn coupled dual-polarised detector. The foreground subtraction and the emphasis on Galactic and extra-Galactic studies will be insured by a large frequency coverage divided in 8 spectral channels. The polarisation modulation will be achieved through the use a unique rotating reflective half-wave plate (RHWP) which will operate over the large spectral coverage needed but will restrict the bandwidth of each spectral channel to 20 GHz.

The instrument (fig 15 left) is based on an off-axis reflective telescope able to accept a large focal plane area (fig 15 right) with limited aberrations and cross-polarisation. The RHWP will be located at the entrance aperture of the telescope so that the instrumental polarisation systematic effects can be more easily removed. The incoming radiation will then go through the telescope to be focused onto the horns that are coupled to Ortho-Mode Transducers (OMT) through a circular waveguide. Each branch of the OMTs separating the two linear polarisations will then be coupled to a Transition Edge Superconductor (TES) bolometer. The cold optics (feedhorns - OMTs - detectors) will be cooled at 100 mK and will be surrounded by a 4 K / 8 K temperature stage. The whole instrument will be enclosed in a passively cooled shield which should be at a temperature of about 35 K, based on in-flight data from the Planck mission. In this case, the telescope mirrors and the RHWP could be at a similar temperature.

7.2 Description of the measurement technique

The combination of orbit and scanning strategy for CORE must ensure that all the frequency channels will cover the full sky with adequate sampling and redundancy, while minimizing environmental systematic effects. The optimization of the CORE scanning strategy will be carried out during the detailed study phase, however, CORE will inherit many of the features successfully implemented for the Planck mission.

The choice of a far-Earth orbit, such as a halo or a quasi-periodic Lissajous orbit around the Sun-Earth Lagrangian point L2, is a mandatory feature for CORE in order to minimize straylight contamination from sidelobe pick-up. Requirements for far-sidelobe rejection are extremely tight for CORE. Because the broad features of the beam pattern at large off-axis angles are essentially the same for all detectors at a given frequency, the required rejection must be calculated against the total sensitivity per frequency channel. Using Planck as a guideline [92], and assuming a factor of 10 better sensitivity for CORE in an L2 orbit, we need roughly -110dB rejection for Sun contamination, -100dB for the Earth, and -80dB for the Moon. Stringent, highly frequency-dependent rejection requirements will be imposed also by straylight from Galactic diffuse emission on intermediate sidelobes. While challenging, straylight rejection limits for CORE can be achieved with very careful optical design and can be tested with a moderate extrapolation of the state-of-the-art technology developed by ESA for the Planck mission. Furthermore, the excellent thermal stability of the L2 environment is ideal to minimize thermal systematic effects on the CORE instrument. The experiences of both WMAP and Planck have demonstrated exquisite thermal stability for small changes in the solar aspect angle, with very small and slow residual thermal drifts. During the first-year Planck survey, in particular, the measured in-flight temperature of the passively cooled stage at

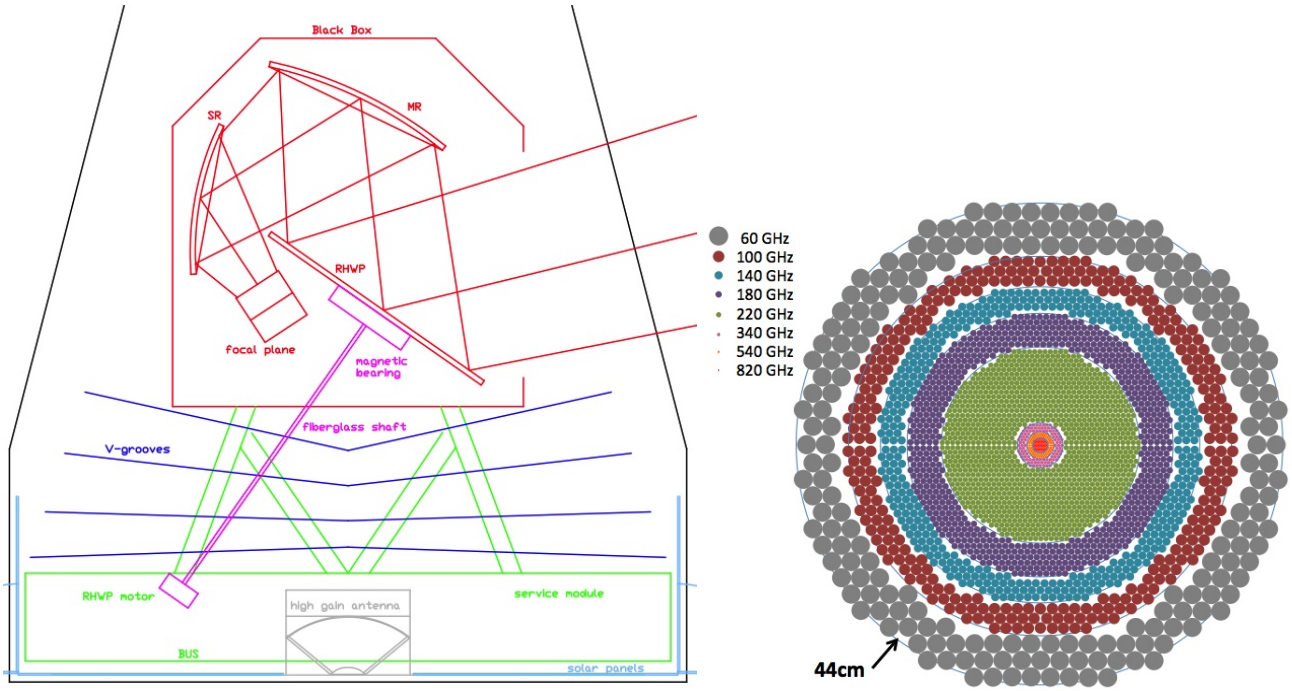

Figure 15: Overall design of the COrE experiment - **Figures need updating**

50K was stable at XXX mK/day, while the Planck-HFI 0.1 stage was stable at ∼YYY ??K/day.[THIS MAY BE SENSITIVE INFORMATION - CHECK WITH PLANCK SCIENCE TEAM].

From the data analysis point of view, it must allow for full sky coverage, optimize the redundancy per map pixel and the variety of time scales involved in the re-visit of a given pixel. This helps to reject "naturally" the statistical noise and most common systematics. Another constraint that is proper to polarization measurements is the need for wide variety of measurement angles per pixel. Indeed, even an infinite number of hits per pixel would give poor polarization determination if they were all done with the same (or close) polarization direction. Another extreme case would be a pixel observed under a uniform distribution of polarization angles but at the expense of redundancy: the reconstructed Stokes parameters would be perfectly uncorrelated but with a very poor signal to noise ratio. In the first B-Pol proposal, all the polarization modulation efforts were put on the payload motion. This led to a sophisticated (but feasible) scanning strategy and set tight constraints on sunshielding. For COrE, the addition of a HWP modulator relaxes these requirements and allows to assume a scanning strategy *à la* Planck and WMAP, with only a precession and a nutation. Let's therefore assume the COrE spacecraft to be a spinner with spin rate $\dot{\mu}$ and with bore-sight telescope angle β. The spin rate $\dot{\mu}$ needs to be fast enough to ensure redundancy for minimizing the effect of $1/f$ noise and thermal fluctuations, and slow enough to be compatible with the bolometer time constants. Based on the Planck experience, we anticipate something of the order of 0.1 to a few rpm, or a step and point approach like in Planck, with similar depointing parameters $\Delta\phi$ of 1 to a few arcmin avery few tens or circles and therefore maintain the nearly anti-solar configuration ($\Delta\phi/\Delta t \sim 1°$/day). This would yield sufficient redundancy in sky circles and, simultaneously, good sampling of the sky for each single beam up to 220 GHz, i.e. in all the main CORE cosmological channels. At higher frequencies, where the angular resolution is $\theta_{FWHM} < 4$ arcmin , adequate sampling would be ensured by proper staggering of the feeds in the focal plane.

Further constraints are imposed on the scanning parameters by thermal and straylight effects, and by telecommunication requirements. The maximum excursion α of the spin axis from anti-Sun direction must be limited, typically within about 15° in order to avoid thermal effects and straylight contamination from the Sun and Moon, and to rule out power-modulation due to asymmetries in the spacecraft or shadowing effects on the solar panels. Also, the angle of the spin-axis to Earth angle must be limited within 20° to ensure good visibility of a fixed medium gain antenna for TM/TC activity. While steerable antenna designs are possible, we do not favor their use since they would complicate the design and increase the risk. The choice for β is coupled to that of α through the requirement of full-sky coverage. Depending on the dynamical constraints and attitude control capabilities, modulation of the spin axis can be set either

Parameter	Definition	Range	Potential criticalities
β	telescope axis to spin axis angle	$75-85°$	$>85°$: straylight, polarization angle redundancy $<75°$: excessive excursion α angle required
$\dot{\mu}$	spin rate	$0.1-2$ rpm	<0.1 rpm : $1/f$ noise, thermal fluctuations >2 rpm : bolometer time constant
$\Delta\phi$	Depointing angle	1−few arcmin	<1: redundancy in sky circles; thrusters lifetime >2: insufficient sky sampling
α	Solar aspect angle	$5-20°$	<10: coupling with β and full-sky requirement >20: thermal effects, straylights
ψ_{Earth}	Maximum Earth aspect angle	$10-20°$	<10: coupling with α >20: TM/TC requirements
$\dot{\phi}$	Precession frequency	1-24 weeks	polarization angle redundancy, destriping thermal effects

Table 9: Scan parameter definitions and allowed variration ranges. See also, fig. 16

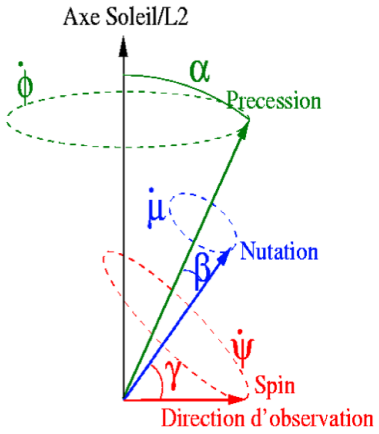

Figure 16: Scanning strategy parameters. α is the precession angle around the anti-solar axis. The associated precession speed is $\dot{\phi}$. β is the nutation angle with associated nutation speed $\dot{\mu}$. This proposal does not include the final spin $\dot{\psi}$ of the payload around the boresight axis. See Tab. 9 for details.

by precession (with the advantage of maintaining a constant solar aspect angle) or with cross-ecliptic excursions at an angle $\alpha = 90 - \beta$. The optimal configuration will be determined via simulations that include polarization angle redundancy, destriping efficiency, and figures of merit for straylight and thermal effects. In Table 9 we summarize a possible baseline based on the Planck experience. Figures 17 and 18 illustrate the performances of two among the allowed configurations and compare them to the previous B-Pol scanning strategy. For simplicity and illustration purpose, we chose typical Planck parameters ($\alpha = 5°$, $\beta = 85°$, $\dot{\mu} = 1$ rpm) with a continuously rotating (1Hz) or stepped HWP. For these simulations, we took standard white and/or $1/f$ noise with $f_{knee} = 0.1$Hz and a $NET = 10\mu$K.sec$^{1/2}$. The associated angular power spectra are presented on Fig. 18.

A detailed optimization of scan parameters (angles and precession/nutation frequencies) could be done in a second step. For this work, suffice is to say that the addition of a HWP enables CORE to relax previous constraints on sunshielding and scanning implementation. In light of these one detector simulations, a continuous rotation of the HWP seems to better reject $1/f$ noise than a stepped HWP. However, we wish to insist on the fact that (1) the $1/f$ rejection can be addressed via performant destriping algorithms such as those developed in the context of Planck; (2) stepping the HWP enables to fine tune the angular coverage and can represent an important technical simplification.

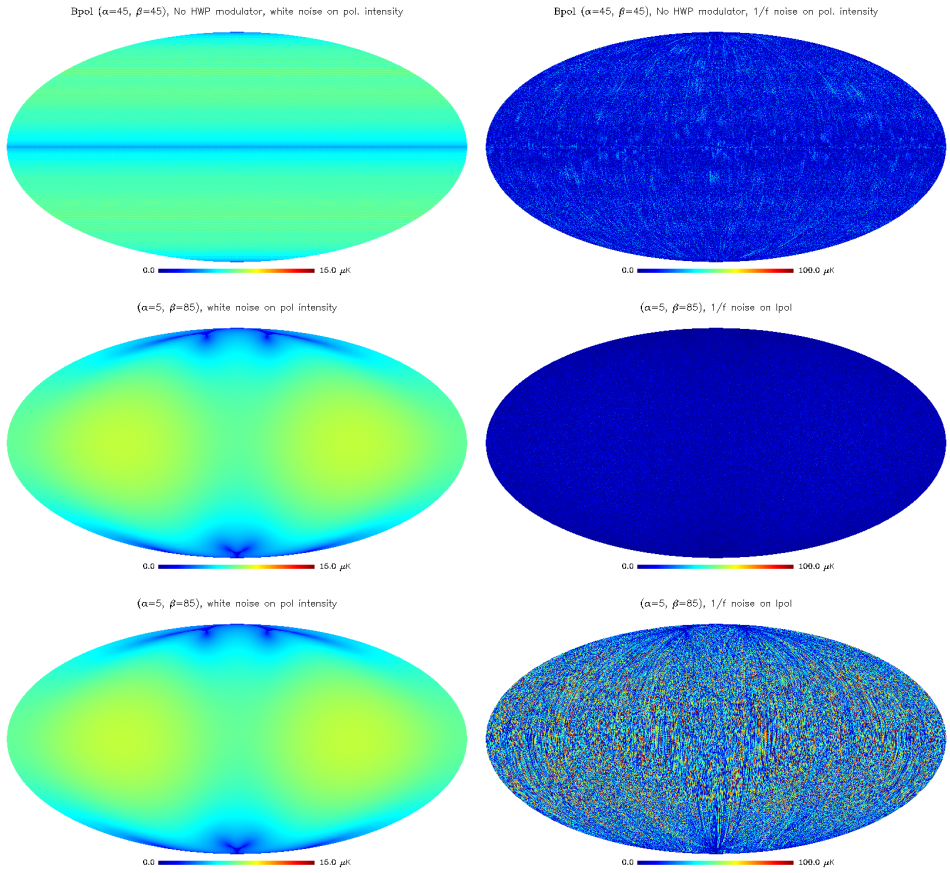

Figure 17: Noise on the reconstructed polarized intensity due to white noise only (left column) or to $1/f$ noise (right column) for the B-Pol scanning strategy (no HWP modulator, top row), for a Planck like scanning strategy with a continuously rotating HWP at 1Hz (middle row) or a HWP stepped by 11.25° every 7 rings (bottom row). Optimizing the HWP steps improves sensitivity and allows for perfect decorrelation of the reconstrued polarization but continuous HWP rotation improves the rejection of $1/f$ induced striping. These maps are for one detector only and we have not run any destriper.

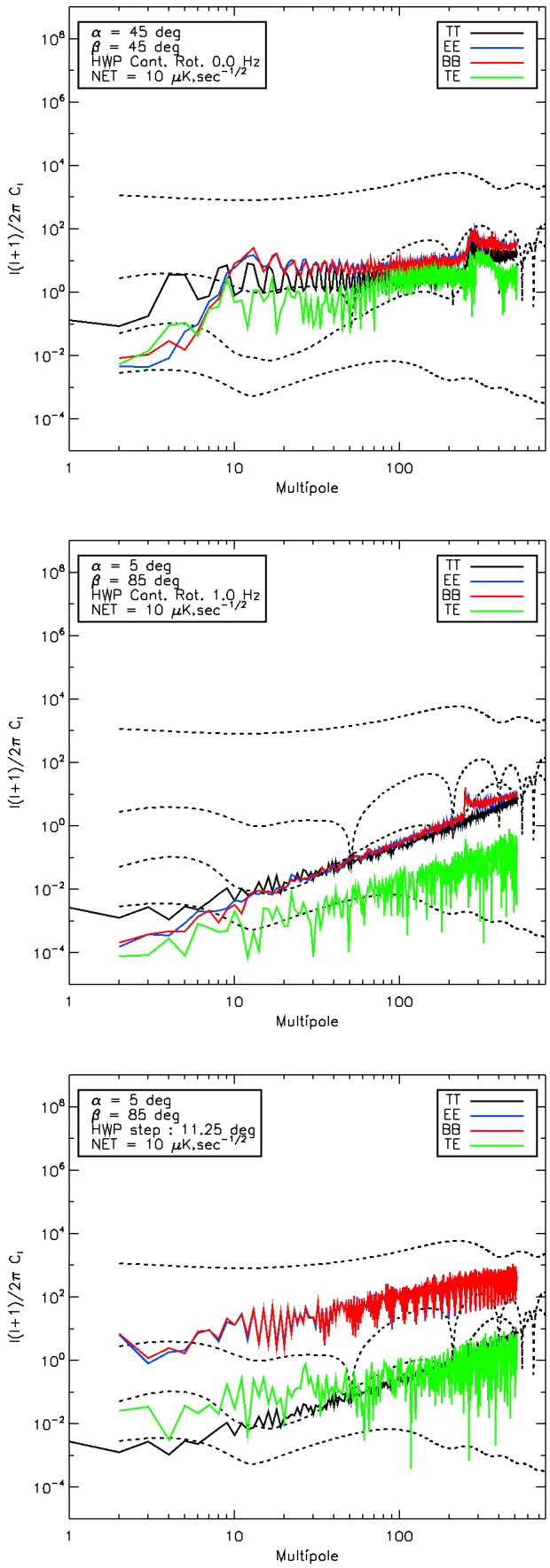

Figure 18: Angular power spectra of the $1/f$ noise timelines projected on maps of Fig. 17 : B-Pol (top), Planck and continuously rotating HWP at 1Hz (middle), Planck and stepped HWP (bottom).

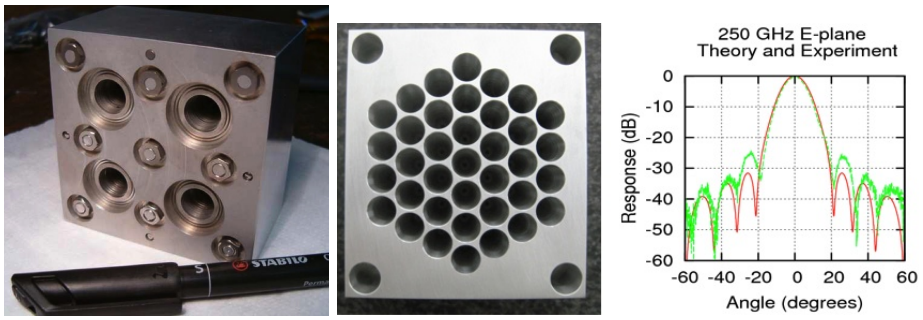

Figure 19: Left: Array of platelets horns - Italy. Centre: Array of drilled smooth walled horns - Oxford University. Right: beam pattern of one of the smooth horn.

7.3 Instrument conceptual design and key characteristics

7.3.1 Optical configuration

A sub-set of the specifications (resolution, spillover, beam ellipticity $< 1\%$, cross-polarisation < -30 dB) needed to achieve scientific goals of the mission are directly relevant to the optics design. Others, such as the background noise on the detectors are a consequence of various sub-systems (optics and thermal chain). In order to meet our requirements with high TRL technology and within the dimension and weight budgets of a Soyuz launcher, we have chosen to base the payload on a unique reflective off-axis compact test range telescope configuration (Clover, QUIET) following the Dragone-Mitsugushi condition. Used In conjunction with feedhorn coupled detectors this design will allow for a large focal plane with limited aberrations needed to fulfil the scientific requirements. This technology is already rated TRL 9. However, because of the large number of detectors that will be included, current areas of research are looking for the possibility to simplify the manufacture to reduce the costs and the mass of feedhorns and more generally waveguide components while retaining their exceptional RF performances. Such developments include drilled smooth walled horns (Fig 19), platelet corrugated horns (Fig 19) and corrugated horns made from metal coated plastic. No doubt that within a few years these techniques will be at a level of maturity allowing their inclusion in the instrument design.

In order to limit the dimensions of a focal plane that will contain all the detectors required to reach the targeted sensitivity, the horn aperture will need to be small, resulting in a fast optical system as shown in figure 20. The resulting configuration has a 1.2m projected diameter making use of F 2 horns, each having a 3λ aperture diameter. Taking into account an array filling factor of 0.8 and leaving enough spacing for the spectral filtering, the overall focal plane unit diameter would be smaller than **40 cm**. The whole optical system will be enclosed in a cavity formed by a shield at 35K with the RHWP acting as a cold stop. It is expected that the telescope could reach a temperature as low as 30 K with passive cooling (compared to 50 K on Planck).

While the performances of this optical first iteration concept is already producing good performances, improvement will be needed during a Phase A study. Attention will have to be paid in order to improve the beam ellipticity of the edge pixels which could be improved with a lengthier optimisation of the telescope / RHWP design as well as a re-shaping of the focal plane array (curved instead of flat surface as assumed so far). Also the possibility of having a colder RHWP will need to be investigated in order to reduce the spillover contribution and to limit the effects of its emissivity (see RHWP section).

7.3.2 Polarisation separation

Following the feed horn transmitting the full intensity of the incoming radiation through its circular waveguide, the two linear polarisation separation is performed with an Ortho-Mode Transducer (OMT). The assembly Horn-OMT will set the minimum cross-polarisation achievable between the two branches that conduct each polarisation to the detector. Waveguide OMTs are the best devices: Return loss and Isolation of the order of 20 dB and 50 dB respectively have been already achieved at 100 GHz on a 30% bandwidth [96], and 40 and 70 dB at 30 GHz [97]. Although further development is underway **(see section xxx)**, with the present technology (TRL 9), these are potentially heavy and managed to have similar performances only for frequencies below 150 GHz.

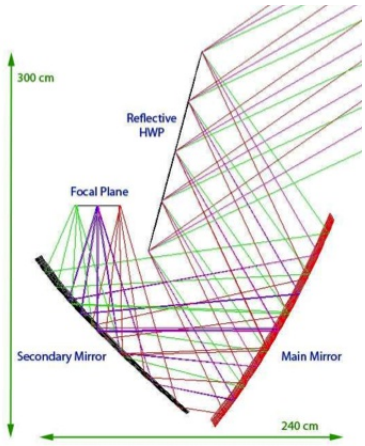

Figure 20: Telescope configuration with ray-tracing

Baseline design: Because of the large number of OMTs in the focal plane, the use of planar technology is preferred. For planar OMTs the two polarizations are extracted by microstrip probes and made easily available to the bolometers. Microstrips circuits are more compact and more suitable for mass production than waveguide devices. A completely symmetric planar OMT can be realised using four probes inside a circular waveguide which are then recombined. Broadband four probes antennas OMT has been realised and tested in the L-band: in a 30% bandwidth the measured return loss and cross-polarisation were respectively around 20 dB and -40 dB [95]. Higher frequency OMTs have been developed for Clover (150/225 GHz). **Performances??**. However development is required in order to reach similar performances for frequencies up to 800 GHz although this technology could in principle be scaled fairly easily.

7.3.3 Detectors and readout electronics

7.3.4 Polarisation modulator

As mentioned earlier, in order to cover the full COrE spectral range, we have chosen to use a Reflecting Half-Wave Plate (RHWP). It consists of a free-standing wire grid polariser kept at a specific distance d from a flat mirror (Fig.21). The RHWP rotates around an axis orthogonal to its surface and passing through its centre. Assuming the RHWP oriented as in Fig.21, depending on the angle of incidence ϕ (dictated by the optical setup) the RHWP will introduce a phase-shift between the two orthogonal s and p polarisations, respectively orthogonal and parallel to the plane of incidence. When the phase-shift is equal to 180^0 and the RHWP rotates with angular velocity ω the overall effect is a rotation of the reflected linear polarisation at a frequency 2ω. This happen only when the path difference between the two waves is equal to π, i.e. at the following frequencies:

$$\nu_n = (2n+1) \text{ with } \nu_0 = \frac{(2n+1)c}{4cos(\phi)d}$$

The modulation efficiency vs. frequency is sinusoidal with maxima at the frequencies ν_n. If no spectral filtering is adopted, the average modulation efficiency is of the order of 0.5. Adding spectral filtering, higher efficiencies can be achieved in narrower bands. As an example, a reduction of 50% bandwidth around one of the peaks implies an efficiency increase of up to 80%. However, this requires additional filtering to be implemented.

Figure 21: Free-standing RHWP

Absorption: The absorption is due to the power dissipated on the metal and on the wires. In a flat metal there is always a slightly different absorption between the s and p polarisations, the latter being

the lossier. The losses increase with the frequency but they can also be reduced decreasing the device temperature. For a room temperature copper RHWP used at $\phi = 45^0$ incidence, assuming an ideal wire-grid, the absorption values integrated across the (0-1) THz frequency range are: $A_s = 1.3 \times 10^{-3}$, $A_p = 2.6 \times 10^{-3}$. More sophisticated and accurate calculations can be carried out using finite-element analysis (Ansoft HFSS) taking into account of the real behaviour and the losses of the wire-grid.

Manufacture: The manufacture of this device would be certainly challenging considering that the required diameter is greater than 1 meter. The mechanical structure of the free-standing wire-grid must be able to guarantee constant spacing between the wires and constant distance from the mirror all across its surface. However, to our knowledge, the biggest device of this type ever built so far has a diameter of 0.5 m [94]. Because of the above problems we are investigating the alternative option that follows.

Dielectric substrate RHWP.

In order to solve the free-standing RHWP manufacture problems we propose to use dielectric materials and photolithographic techniques. The air-gap between the wire-grid and the mirror can be replaced by a dielectric substrate and the wire-grid can be realised directly on one of the substrate surfaces (Fig.22).

Figure 22: Dielectric substrate RHWP

Manufacture: Commercially available dielectric laminates used in microwave engineering to build planar microstrip circuits could be used to build our device. These laminates come in different sizes, thicknesses, refractive indices and they have copper depositions on both sides. The idea is to use one metallic side as a mirror and photolithographically etch the other side of the substrate in order to realise metallic strips that will behave like a wire-grid. The resolution required for the mask production in our frequency range is achievable with commercial large size printers. The laminate can be joined to a thick metallic flat surface to increase the structure stiffness. Note that the main problems of the free-standing RHWP are now solved: the constant spacing between wires is guaranteed by the high accuracy of the photolithographic techniques adopted whereas the constant distance mirror-wires comes directly from the accurate constant thickness of the laminates that is required in microstrip circuits.

Modulation efficiency: The addition of a dielectric substrate has the effect of introducing frequency-dependent standing waves (multiple reflections) within it. Their amplitude will also depend on the type of polarisation s or p travelling through it. A transmission line code has been developed to evaluate the performance of this device at any angle of incidence. The resulting modulation efficiency deteriorates with increasing the substrate refractive index. Using a substrate with n=1.2 the efficiency drops down to 0.4. Also in this case, spectral filtering can improve it. More accurate calculations can be performed using again finite-element analysis.

Absorption: Using a lossless substrate with n=1.2 the absorption values change slightly depending on the RHWP orientation. These additional losses, due to resonances, appear at frequencies corresponding to the device efficiency peaks. However, for a copper made RHWP the values are within the following ranges: $A_s = 1.3 - 1.8 \times 10^{-3}$, $A_p = 2.6 - 2.7 \times 10^{-3}$. (This means that the s/p components of an unpolarised background signal will be modulated at 2? with relative amplitudes $5 \times 10^{-4}/10^{-4}$ respectively **TBC**)

Additional spectral filtering

As mentioned above, the modulation efficiency of the high frequency channels can be increased using broader bands in combination with sub-band selective filtering around the peaks. This can be achieved for example using multilayer dielectrics that act as dielectric mirrors. There are specific recipes that allow to reject radiation at periodic intervals as shown in the example in Fig 23.

Figure 23: Sub-band filtering

7.3.5 Polarisation modulator rotation mechanism

The RHWP will need to be rotated. While a step and integrate rotation could be considered, a continuous rotation at about **0.1 to 1 rpm** would be preferable both for the observation strategy and in

order to avoid affecting the rotation of the satellite. Such a strategy has been adopted on the balloon borne experiments Maxima and EBEX [91] for which a superconductive magnetic bearing has been developed. It is able to rotate the HWP at a few Hz with low friction dissipation **[check dissipation]**. This is a crucial parameter as the RHWP will have to operate at the lowest temperature possible (30K for this instance) in order to reduce the systematic effects related to its emissivity. The rotation will be insured by a fibreglass shaft linked to a step motor operated at a higher temperature within the service module with a higher cooling power (see fig 15). Rotation mechanisms have already been used for space application. In our case the difficulty resides in having to rotate a HWP of **1.7 m** diameter, weighting approximatively 25 kg including its support structure while been kept at 30 K.

7.3.6 Cryogenic chain

Architecture
Passive cooling: V-grooves, a system of light-weight panels with a V-shape, offer an elegant solution to a first passive cooling stage. They have been used in Planck to radiate some power into free space but laterally to the spin axis. These V-grooves can also provide cooling to intermediate stage electronics. An inner V-groove temperature of **50 K** is currently achieved in orbit with an available power of the order of 1 W for Planck. With further optimisation and with an addition of a fourth V-groove, we expect that a temperature of about **35 K** could be achieved for COrE inner V-groove.
Active cooling - Mechanical coolers

- Pulse Tube from 35 to 20K
- JT 20K- to 4K idem Planck

To allow a continuous science mission, the coldest temperature at detector level (0.1K) will be continuously provided by a Close Cycle Dilution Refrigerator (CCDR). This system is an evolution of the flight-proven Open Cycle dilution Refrigerator (OCDR) of Planck. The re-circulation of the helium isotopes (He-3 and He-4) of this system allows theoretically to have no limitation on lifetime. Contrary to the OCDR, the CCDR requires a pre-cooling stage around 1.7K in order to evacuate the heat from thermalisation of He-3 and He-4 gas flows and from condensation of He-3 (a fraction this heat is used for the evaporation of He-3 but not all of it). As the close cycle dilution system requires a circulation of helium-3, there is no more high pressure storage tank like on Planck; therefore it is not possible to produce a 1.7K stage with a He-3 Joule-Thomson expansion within the dilution system. As a consequence, the 1.7K stage is produced by a dedicated helium sorption cooler similar to the one used on Herschel.

7.3.7 Spectral filtering

Bolometric detectors being sensitive to a very wide spectral range, their spectral band definition requires special attention. Any millimetre/submillimetre instrument designed for CMB polarisation studies requires that the in- band transmission is high (>80%) whilst the rejection of optical/NIR power is at a level whereby, if detected it presents a signal much smaller than the expected anisotropy power in the polarised signal component. In short the rejection must be better than $\approx 10^{-12}$ while a rejection of $\approx 10^{-6}$ is enough in the FIR. Low frequency rejection can be easily achieved through the horn waveguide design. Typical horns will have an in-band return loss of -25dB. While The high frequency band definition will require several multilayer mesh filters in series located on the different temperature stages also limiting the thermal power reaching the ultra-cold stages. Similar schemes, making use of dielectric embedded interference filters, have been used in sub-orbital instruments (e.g. QUaD, Clover and Spider - all large aperture B-mode CMB anisotropy experiments) and in several space missions already (Planck, Herschel). This technology allows for use with mixed frequency array by arranging their geometry to suit the shape of the sub-array. It is also conceivable to make a unique filter made of several regions. However, special attention will have to avoid potential straylight in between regions/filters and cross-talk.

7.4 Performance assessment with respect to science objectives

The performances of COrE is given in Table 10.

Table 10: COrE performances - assuming a 15GHz BW and a 50% value for detection chain efficiency

Central Frequency (GHz)	45	75	105	135	165	195	225	
Number of detectors	64	300	400	550	750	1150	1800	
FWHM (arcmin)	23.3	14	10	7.8	6.4	5.4	4.7	
Unpolarised sensitivity (μK.arcmin)	5.2	2.7	2.7	2.6	2.6	2.6	2.6	
Q & U sensitivity (μK.arcmin)	9.0	4.7	4.6	4.5	4.6	4.5	4.5	
Central Frequency (GHz)	255	285	315	375	435	555	675	795
Number of detectors	575	375	100	64	64	64	64	64
FWHM (arcmin)	4.1	3.7	3.3	2.8	2.4	1.9	1.6	1.3
Unpolarised sensitivity (μK.arcmin)	6.0	10.0	26.6	67.8	147.6	787	4573	27923
Q & U sensitivity (μK.arcmin)	10.4	17	46	117	255	1360	7904	48257

7.5 Resources: mass, volume, power, on board data handling and telemetry

The resources have been established by the COrE team in collaboration with CNES [93] and are essentially based upon the Planck mission. COrE mass and power breakdown is given in table 11. We can note that the total estimated mass (1832 kg) and power (1279 W) are lower than for the Planck mission (1974 kg and 1342 W).

The overall volume is similar to the Planck payload volume. Stored under the Soyuz fairing the maximum diameter is 3.8 m and about 4 m tall. With the solar panels fully deployed the diameter will reach about 5.9 m.

Data storage capacity : a mass memory of 518 Gbits is needed (instead of 32 Gbits for Planck).

The data rate at instrument output is assumed to be 6 Mbits/s (compression included) to be compared to 130 kbits/s on Planck.

Table 11: Table with mass, volume and power - From CNES [93]

Sub-system	Mass	Power	Sub-system	Mass (kg)	Power(W)
Other payload parts					
(Structure, V-grooves Sv. mod etc)	1365	577	20K PTC	26	250
30K Cold Box and telescope supports	180		4K J-T cooler	21	102
RHWP + Telescope	60		1.7K Sorption cooler	10	20
Rotation Mechanism	20		0.1K Dilution	30	30
Focal Plane Unit		300	Cryo Harness	50	
Horns, OMTs, Detectors	50				
Read out electronics	20		**Total**	**1832**	**1279**

7.6 Pointing and alignment requirements

The beam of the instrument ranges from typically 23 arcmin to about 1 arcmin at the highest frequency. The most stringent requirement will come from the CMB channels (45 to 225GHz) for which the ability to recover pointing information must be less than 1% of the beam FWHM. This means a pointing accuracy of 3 arcsec. The telescope axis, horn axes directions, and polarimeters main axes will be determined with respect to the satellite reference system to within 0.5 degrees during the calibration phase. This measurement will be repeated independently during the verification / validation / calibration phase at the beginning of the mission.

7.7 Operating modes

After the verification phase the instrument will operate in a single survey mode.

7.8 Specific interface requirements: configuration needs, thermal needs

Similarly to Planck, COrE will be launched warm and will be cooled during its travel to the L2 orbit.

7.9 Calibration and other specific requirements

In order to keep the instrument simple and without single point failure, no on-board calibration system will be implemented. COrE calibration will rely on ground calibration sequences and astrophysical sources that will have been thoroughly studied by Planck and follow-up observations. Systematic effects affecting the polarisation purity of the incoming signal will be mitigated by the use of the HWP in front of the telescope. However, the HWP will introduce systematic effects on the beam shape and they will vary with its orientation. Dedicated calibration procedures will be needed to characterise these effects.
The ground calibration will be composed from complementary laboratory test campaigns.

Sub-system level: (detectors, reflective optics, cold optics, RHWP, cooling system)

Focal plane level: spectral response of each pixel, dark and illuminated detector tests for different focal plane temperatures.

Warm RF test in anechoic chamber: representative test of a few horns, OMTs and warm detectors (heterodyne instead of TES) associated with the telescope, shields and the RHWP in order to measure the main beam and far sidelobes. Similar test conducted during the Planck ground calibration campaigns have been extremely beneficial in order to understand the systematic effects caused by the telescope (alignment and surface accuracy) and the feedhorns. Emphasis will be on the measurement and modeling of the Ssystematic effects introduced by the RHWP.

Dedicated calibration facility reproducing the cryogenic and radiative environment expected during the mission. A large vacuum chamber instrumented with a 2K cryogenic chain and with a full beam source will be prepared. The chamber will allow the operation of the full instrument, observing a 2.7K load and a polarized source modulated and oriented as needed. This setup will allow the precise determination of the polarimetric parameters of the instrument (polarization efficiency and main axis angles) and of the responsivity and noise of all the detectors for different radiative loading conditions. The proposers inherit considerable experience from similar calibration facilities they built for Archeops and BOOMERanG, but also through the calibration campaign performed on Planck at CSL-Liége.

7.10 Current heritage and Technology Readiness Level (TRL)

TRL levels associated to COrE sub-systems as well as their heritage is given in table 12.

Table 12: default

Sub-system	TRL	Heritage
Telescope	9	WMAP, Planck
Horns	9	COBE, WMAP, Planck
Waveguide OMTs	9	Clover, WMAP, Planck
Planar OMTs	6	Clover, PAPPA
RHWP	??	
Rotation mechanism	8 or 9	Maxima, EBEX, Any Space mission ?
Interference filters	9	Herschel, Planck
TES detectors + Readout	6	SCUBA, GBT, CLOVER
Mechanical coolers	9	Planck
Sorption cooler	9	Herschel
Close cycle DF	4, 5 within 2 years	
ADR	9	XRS on ASTRO-E2

7.11 Proposed procurement approach

We propose a standard procurement approach: the service module, the launch and the operations will be provided by ESA, while the instrument, including the telescope and the scientific ground segment will be provided by a consortium of national space agencies. The consortium of participating institutes will be in charge of the developments, in strict coordination with industrial partners selected for experience, reliability, and geographical returns. The share of cost and provision of subsystems by the interested international (non-ESA) partners is to be defined during phase-A.

7.12 Critical issues

Critical issues with the payload sub-systems are developed in more details in **section xxx**. These are:
OMTs: While high performance waveguide OMTs have been developed at 100 GHz and could be developed with a high level of confidence to 200 GHz, it might be an issue at even higher frequency.
RHWP: Problems linked with the size of the waveplate. Low TRL.
Rotation mechanism: Dissipation, microphonic vibrations affecting the detectors.
Close cycle dilution fridge: While the ADR option is already at TRL 9, a Close Cycle Dilution fridge would be preferable but needs further development.

8 System requirements and spacecraft key factor (5 pages) PdB, FRB

The *COrE* mission is composed by a single instrument on-board a single spacecraft, in orbits around the second Lagrangian point (L2) of the Sun-Earth system on a 500000/800000 km orbit ◄ **TBC** ►. It is a survey instrument able to cover up to 50% of the sky in a few days. Due to Sun incidence angle constraints, a minimum of six months are required to cover the full sky.◄ **Need to be verified w. all constrains.** ►

8.1 Attitude and orbit control

The Lissajous orbit can be controlled by a 10 hours manoeuvre session per month.

The angular resolution of the instrument is similar or better (for half the channels) than the one of *Planck* (FWHM $\lesssim$ 5 arcmin at $\nu \leq 220\,\mathrm{GHz}$). The strong requirement on the maximum ellipticity of the beams is such that the pointing accuracy is driven by the necessity to avoid a fake beam ellipticity induced by asymmetric pointing noise. Given a 1% requirement in the beam ellipticity, the ability to recover pointing information must be less than a few % of the beam FWHM. The requirement in the accuracy in pointing reconstruction is then of about one arcsecond. A *Planck* like system is suitable to match this requirement. The ability to point to a specific direction in the sky is much reduced with respect to the pointing recovery value, and is needed to point towards specific astronomical objects within the size of each array. The requirement is set here of the order of an arcminute, one tenth of the smallest array.

In addition to the classical compromise between survey size and sensitivity, *COrE*has to account of the directivity of polarization. It is both an additional constraint on the system and a lever arm against systematic effects. Let us recall here the key ideas behind polarization measure.

Polarization is usually described in terms of the Stokes parameters I, Q and U. I is the total intensity of the incident radiation, Q is the difference between intensities measured in two orthogonal directions. U is the same as Q but with two other orthogonal directions rotated by 45° with respect to the previous ones. In *COrE* we propose to implement a rotating *p*olarization modulator made of a rotating Half-Wave Plate (hereafter RHWP) which modulates simultaneously all the detectors in the focal plane, so that each detector measures $m = 0.5(I+Q\cos 4\alpha+U\sin 4\alpha)+n$ (1) where n is the noise and $\alpha = \omega t$ is the orientation of the RHWP. Each measurement is the linear combination of three independent parameters. Three independent measurements, each at a different angle α, are therefore required (at least) to determine the polarization state. In the absence of a polarization modulator, these measurements would require to rotate the detector. However, that approach mixes beam-shape and detector-related effects with real polarization signals. The use of the modulator has simplified very significantly the measurement and scan strategy: the satellite does not need to be rotated, and the sky scan can be very similar to the one used in *Planck*: the continuous rotation of the RHWP, at a frequency not commensurate to the spin frequency, provides the required change in α for each re-observation, after each scan, of the same sky

Figure 24: here include figure TBD from F. Piacentini

Figure 25: here include figure TBD from N. Ponthieu

pixel. The basic idea behind the latter is that equation (1) shows that *polarization is modulated at* 4α when the modulator is rotated by α, *whereas most systematic effects are fixed* in the instrument reference frame. Rotating the modulator with respect to the incoming polarization and providing sufficient angular coverage is therefore analogous to a lock-in detection that selects polarization and cancels out systematic effects. The rotation frequency of the modulator is around $0.1 \div 0.5$ Hz, slow enough to avoid microphonic effects.

Those requirements lead to a scanning strategy based on a 0.5 rpm sky scan along a large circle (semi-aperture 85^o), with a slow precession around the anti-Sun axis (about 15^o off-axis, with a period of a few months, synchronous to the orbit).

The results of detailed simulations of this scan / modulation strategy are summarized in fig. 24 and 25. The improvement with respect to the *Planck*survey (which had not been optimized for polarization measurements) is very significant.

The attitude control of the payload will be done with a star tracker and reaction wheels and three axes system. Preliminary studies recommend 4 wheels without redundancy consideration. No specific difficulty was identified since it is quite recurrent from Hershel/*Planck*.

8.2 On board data handling and telemetry

Data are partially treated on-board by a dedicated Data Processing Unit that compresses the data produced by the readout electronics. Data are then transferred to the Service Module for storage and download. The on-board data storage system should be able to save a few days of data in order to cope with downlink problems due to contingencies in the telecommunication system. A strategy will be defined to optimize the data downlink after those events. Detectors currently used for CMB observations are already photon noise limited, which means that to increase the instrumental sensitivity, one has to increase the number of detectors. This directly impacts on the telemetry requirements. Based on *Planck* experience, we request 16 bits per scientific data sample. For an instrument equipped with 6000 detectors, and with a sampling rate matching the scan speed and the FWHM of the beam for each frequency channel, this leads to 18 Mbps, which are reduced to 4.5 Mbps by compression (as successfully

demonstrated with *Planck*). This calls for a medium or high-gain antenna ◄ **TBC** ►. In our system the antenna is fixed and aligned to the spin axis of the satellite, with the satellite axis is constantly aligned to the Earth, thus allowing data downloads as long as needed. ◄ **here include more details on the telemetry and ground station** ►.

Assuming the telemetry is done with a 35m antenna (e.g. Norcia), the full cost of the ground segment for a 4 year mission with a 2 month transfer, including $\sim 20\%$ margins and CNES participation is less than ..... Meuros.◄ **TBC** ►

8.3 Mission operation concept (Ground Segment)

The Ground Segment operations are greatly simplified with respect to *Planck*. The payload will host a single survey instrument, with high redundancy in sky coverage. As a baseline, after downlink the data will be sent to the Instrument Team for analysis of the Housekeeping data and detection of anomalies. The Mission Operation Control will take care of pointing reconstruction. The Instrument team will take care of the first analysis of the quality of the data and of the data storage.

The pointing strategy will be defined well in advance and the Mission Operation Control will operate the spacecraft according to the pointing law, ensuring respect of the constraints.

8.4 Estimated overall resources (mass and power)

Based on *Planck*experience, we estimate that the Service Module would weigh about 580 kg ◄ **TBC** ► and the payload module about 590 kg (without margins, ◄ **TBC** ►). Including 150 kg of propellant ◄ **TBC** ►, this would lead to 1500 kg ◄ **TBC** ► satellite.

Power ◄ **TBD** ►

8.5 Specific environmental constraints (EMC, Temperature, cleanliness)

The environmental constraints are very similar to the ones applied in the *Planck*mission. In addition to that, the readout system based on SQUIDs generates specific problems of magnetic compatibility. This issue is resolved internally in the instrument, by proper magnetic shielding already demonstrated in other instruments.

8.6 Special requirements

The proposed scan and orbit allow for a very constant solar illumination of the satellite. The absence of important dissipation in the cold instrument makes us confident that a stable operation temperature of 30K can be reached using the solar panels as shields for the SVM, and *Planck*-like V-grooves shielding the cold instrument section. The passive cooling V-groove systems has therefore a TRL of 9.

8.7 Current heritage (assumed bus) and TRL

The service module is similar to the Hershel/*Planck*one, with only minor modifications required to fit in the Soyuz vector. ◄ **TBC** ►. The spacecraft TRL is high for most of the component, that have been already used in previous missions, or will have been at the time of the mission.

◄ **TRL table to be done** ►

8.8 Proposed procurement approach

We propose a "standard" procurement approach: the service module, the launch and the operations will be provided by ESA, while the instrument will be provided by a consortium of national space agencies. The consortium of participating institutes will be in charge of the developments, in strict coordination with industrial partners selected for experience, reliability, and geographical returns. The share of cost and provision of subsystems by the interested international (non-ESA) partners is to be defined during phase-A.

8.9 Critical issues.

◄ what follows is to be confirmed and modified after we have a final word from CNES ►

The scanning strategy of the payload sets constrains on the AOCS, in particular the spin about the bore sight axis. Although not new, the involved technologies are considered critical. A specific study is needed once the payload configuration and mass are designed to dimension these systems and their performances and impact on the other subsystems, through micro-vibrations and magnetic coupling for instance. These studies must also account for the presence and evolution of liquids in the payload during the operation and the associated dissipations and mass distribution variations.

Planck PF has a small interference with the Soyuz launcher, driving the bottom panel for SA to be redrawn / scaled down (from 4220 to 3820). This is a minor modification due the principal structure is not modified (the principal structure stays within a diameter of 3780 mm).

Planck PF interface with launcher is a circle of a diameter that is 2420 mm. This shall be modified into an interface at 2100mm. New adapter development is needed.

*Planck*PF has onboard 2 LGA and 1 MGA; the data rate from L2 is nominally 1.5 Mbps (maximum 2.25). This drive the mission to have a ratio of observation to communication times about 2 to 3 (i.e. 7 h of communication and 17 h of observation) with nominal DR. However, a more recent transponder (example DST BepiColombo) will easily provide a 3 Mbps datarate, allowing a 4 h of communications and 20 hours of survey ratio. **◄ TBC ►**

Other problem may concern the need for HGA antenna and its locations (in the sampan study there was a reflector antenna located inside the adapter - in *Planck* this place is occupied by a part of SAs). And relocation of MGA/LGA (the latter creates interference with Soyuz fairing in the actual position)

Modification of thermal radiators and thermal control due the new implementations has to be studied in detail.

Modification of SA position (scaling down the baseplate, removing/not removing SA from the inside adapter, addition of SA on sides) has to be studied in detail.

Criticalities for the instrument have been detailed in §**??**.

9 Science operations and archiving (2 pages) FRB, Stompor, Natoli

NB: text to be amended to take into account that 2 years of data taking should rather be 4 years, 2000 detectors should be 4000 (ie mult by 4 data volume) 6 maps is in conf A, we are likely to be in config B (TBC), with about twice many bands (ie about twice the number of maps, 4 timesthe number of cross correlations). Also, in the 1st phase of DA, one also uses special phasse, like ground and in-flight calibration period, planets, other calibration sources (CRAB?), etc, ie not only redundancy. Additionaly , we need to give more thoughts to teams structure... Anyway, here follows the 1st very rough draft.

As mentioned in the proposal, operations are particularly simple for this proposed survey mission. This is also reflected in the science operation plan, in which the most relevant part is given by the data analysis issue, in view of the large amount of data collected and the high accuracy and redundancy needed to avoid contamination in the results due to systematic effects.

9.1 Science Operations Architecture and proposed share of responsibilities

We emphasize that the COrE data analysis and data analysis organization effort will benefit greatly from experiences derived from the on-going work on the Planck data set. This fact stems from the specific involvement of some of the key-members of the Planck team in the COrE proposal. More in general, by the time COrE might fly, the community will certainly have developed a rich expertise in handling and interpreting data sets of a comparable complexity and quality.

This is extremely important as data analysis is a crucial step in ensuring the efficient and effective scientific exploitation of any data set and the hands-on experience is invaluable, providing the best assurance that the exploitation of the COrE data will be timely and efficient and its goals indeed reached.

The level of involved difficulty depends however on the size and complexity of the data set as well as the amplitudes of the signals which are to be determined from the data. Both these aspects will make the analysis of the COrE data set (hereafter, COrE DA) a challenging undertaking, unmatched by any of the past and current efforts in the CMB field and, at least in some aspects, by many of the currently considered future ones. Undoubtedly, the COrE DA will require a well coordinated team of dedicated researchers, an organized long term effort undertaken in parallel and in close interaction with

the instrument development, and substantial (super) computing resources. We argue below that, allowing for the presence of such resources, the COrE DA, though significant, is totally feasible and will pave the way to achieving all its major scientific goals. In the following we outline some aspects of the challenge and describe a blue-print for a plausible analysis of the COrE data. COrE will scan the sky for at least two years with a sampling rate of $\approx 2\,$ms. A single datum taken by the instrument can be modelled as,

$$d(t) = [1, \cos 2\phi_t, \sin 2\phi_t](B(\hat{\gamma}_t, \hat{\gamma}) * \hat{I}(\hat{\gamma})) + \sigma_t + n_t,$$

where $\hat{I}$ is a vector of the three Stokes parameters (I, Q, U, the first describing the intensity sky signal, the other two linear polarization), $\hat{\gamma}_t$ denotes the observation direction, ϕ_t the polarimeter orientation in the sky coordinates, $B(\hat{\gamma}_t, \hat{\gamma})$ the matrix-valued experimental beam and n_t (σ_t) the instrumental noise (systematic effects) at time t. The symbol $*$ stands for a sky convolution. The data analysis task breaks up then into four major steps. First, using the redundancy of the measurements, estimate the instrumental parameters, such as beam shapes, $B(\hat{\gamma}_t, \hat{\gamma})$, systematic effects, σ_t, and the noise properties, n_t, together with the pointing, $\hat{\gamma}_t$, and calibration factors (i.e., pre-processing). Second, estimate the Stokes parameters of the pixelized sky at the instrument frequencies (i.e., map-making). This can be achieved with minimum variance method that are also robust towards systematic effects. In a CMB field oriented further analysis, the single-frequency sky estimates (hereafter, maps) are subsequently used to obtain a foreground-cleaned CMB map (i.e., component separation) which is then subjected to statistical analysis (e.g., power spectrum/2-point correlation function estimation). The foreground maps are subject to separate investigation, depending on the specific science goal. The CMB power spectra and maps for each frequency band, as well as the maps of astrophysical components, constitute the major products of the COrE mission. They will provide a manageable starting point for further scientific exploitation of the data, to be mined for years to come. The quality and accuracy of the COrE data products will crucially depend on a careful, science-oriented optimization of the experimental set up (beam sizes, polarization modulation, frequency bands, etc.) and its operations (calibration strategy, scan pattern, etc.). Such optimization, performed at the interface between the data analysis and instrument teams, will also aid and simplify the data processing for COrE. Each of the DA steps, listed above, poses its own challenges, principally due to the sheer volume of the time-ordered data and the required precision needed to detect and characterize B-mode polarization fluctuations. In the time domain the COrE data set is expected to contain $\mathcal{O}(10^{14})$ total time samples collected by its $\approx$ two thousand detectors. In the pixel domain, the data set will be composed of six single-frequency maps each containing $\mathcal{O}(10^7)$ beam-size (i.e., ~ 5 arcmin at 220 GHz) pixels.

In the time domain the COrE data set will be thus two to three orders of magnitude larger than the anticipated Planck data set. In the pixel domain, however, it will be roughly comparable to Planck when frequency maps are considered, and at least an order of magnitude more when accounting for single detector maps, which will form the basis of cross correlation analysis, an analysis strategy very robust to systematic biasing. The computational effort for the CoRE DA will likely be dominated by massive Monte Carlo runs which are needed by the statistical estimators to test the physical models and measure their significant parameters. It is likely to expect that such massive Monte Carlo runs will be mostly deployed at the map level, leading to significant savings in the total number of floating-point operations required for the analysis, with only a small fraction of the sheer simulations left for the traditional and more accurate, yet extremely time consuming, timeline to map approach. In this regard we will be able to capitalize on the many techniques, and their efficient implementations, that have already been developed and validated by the CMB community for the accurate processing and statistical analysis of maps. Efficient, high-precision techniques for the astrophysical component separation and map cleaning are of paramount importance for the success of the mission. At present, this is a high-priority, dynamic area of a research which is driven, on one hand, by the needs and data of Planck, and on the other, by forthcoming sub-orbital experiments. As a result, several promising novel methods have been proposed (see Section **??** of this proposal) and, with continued development, these should be sufficient for the COrE analysis. In the time domain, the size of the COrE data set, though clearly dwarfed by the anticipated data volumes from other astronomical projects (e.g., LOFAR, SKA, LSST, ALMA[2], which will be operational on a time-scale similar to COrE), is large by current CMB standards. The existing methods and software tools relevant for the time-domain processing have been used to process data volumes which amount, at most, to a few percent of that expected from COrE (e.g., the Planck simulations, Ashdown et al, Astronomy & Astrophysics, 467, 761, 2007). Extrapolating the performance of these methods, we estimate that to produce all the single-frequency maps from two years of data from all COrE detectors would take several days on an average present-day supercomputer with $\sim 1,000$ processing units. The growing power of

[2] `http://www.lofar.org/, http://www.skatelescope.org/, http://www.lsst.org/, http://www.alma.nrao.edu`

parallel-computing platforms, combined with improvements in efficiency of massively-parallel algorithms and codes, should bring the estimated time to make maps down by at least an order of magnitude, permitting a repetitive processing of the entire data set. The forecasted performance of data storage and retrieval systems should also be capable, within a decade, of efficient handling $\mathcal{O}(1)$TB data objects while easily storing up to $\mathcal{O}(1)$PB of data – a high watermark for the volume of the raw and derived COrE data products created in the course of the DA. It is thus likely that, as is currently the case, it will be human time that is the real bottleneck for the time-domain processing efficiency. We thus envisage a significant need for automated data-processing tools and methods which will have to be developed by the time of the mission. Such tools have already been proposed for other experiments and the COrE DA will be able to benefit from, and contribute to, that on-going development.

9.2 Science Operations Architecture and Share of Responsibilities

Organizationally, the DA effort will be focused around the COrE Data Processing and Exploitation Center (DPEC). Though structurally centralized, the DPEC will need to be geographically distributed. It will be composed of two closely interacting and partially overlapping teams, referred to as the Infrastructure Developement (ID) and Algorithm Development (AD) teams. The ID team will be primarily responsible for the development of the data analysis framework and infrastructure. It will consist of dedicated programmers with an addition of a few supporting scientists, some of which will belong to the AD team as well. The ma jor tasks of this team will include work on databases for storing and retrieving diverse data products as well as a high performance Input/Output layer. Closer to the launch it will be also responsible for creating and streamlining the DA pipeline assembled from the building blocks provided by the AD team. The AD team, will take a responsibility for the development of the DA algorithms and software tools relevant to all stages of the DA. Primarily, it will be composed of dedicated scientists covering broad range of skills relevant to the DA task. A single, focused team working on all the aspects of the pipeline will ensure a better exploitation of the team resources and coordination of work. The AT team will contribute to the groundwork for the infrastructure design, and later on, will become a primary tester and then user of the DPEC built pipeline. The overlap between the members of both teams will ensure the necessary level of coordination and communication between the teams. Both teams will work together on the DA of the COrE data set once those are available. The DPECs ID team will also manage the ma jor computational resources of the collaboration. We anticipate that at the peak of the DA those will amount to a dedicated, massively-parallel 1 PetaFlop/s platform supplemented by high performance and capacity (O(1) PB) storage.

9.3 Archive approach

The data will be stored as time ordered raw-data sets (one TORD per detector) during the survey. Cleaned, calibrated timelines will be processed from the TORD, and stored for the subsequent polarized map-making and spectral estimations.

9.4 Proprietary data policy

The data will be pre-analyzed by the DPEC in the two years following the end of the survey. The resulting data products will be calibrated maps of the Stokes parameters, one for each observed frequency. The DPEC will be in charge of producing a public data release together with the rst round of scientic publications on the results of COrE.

ESA will support the data legacy archive, to serve the scientic community to exploit the maximum prot from the extremely low noise and systematics free full sky data set.

10 Technology development requirements (2 pages) Withington, Pisano, et al.

10.1 Payload technology challenges and technology development strategy

10.1.1 OMTs

Include development on OMT arrays - platelets - stereolithography

10.1.2 RHWP

10.1.3 Rotation mechanism

For the torque transmittance between the motor and the mirror, a long fibreglass shaft is a good solution but two points should be hazardous for this solution:

A particular study would be made about mechanical properties for a glass fibres compound material at 30K. It may be very brittle. The other aspect is about the interface between compound material and metallic part due to different thermal expansion factors.

The other critical point could be the dynamical aspect of the shaft. The shaft diameter will be studied with the stress criteria (torque transmission) and the dynamic criteria (modes for launch and no torsional modes to not interfere with the motor) If the long shaft solution brings thermal problems to go from the motor to the mirror, it exists magnetic contact-less coupling devices. This kind of device should permit to reduce thermo-mechanical aspects for the shaft. During the launch phase, it is necessary to immobilise all the moving parts. A particular device will be proposed to immobilise the 1.2m diameter mirror during launch. This device will release all moving parts before the mission and without friction. During the mission, the bearing mechanism for the mirror will be studied for the lubrications problems. Attention with the lubrication at 30K during the entire mission (probabely a dry lubrication solution) The rotating assembly must be statically and dynamically balanced to minimise the motor torque at the beginning of the mission.

Dissipation, microphonic vibrations affecting the detectors.

10.1.4 Close cycle dilution fridge

To allow a continuous science mission, the coldest temperature at detector level (0.1K) will be continuously provided by a Close Cycle Dilution Refrigerator (CCDR). This system is an evolution of the flight-proven Open Cycle dilution Refrigerator (OCDR) of Planck. The re-circulation of the helium isotopes (He-3 and He-4) of this system allows theoretically to have no limitation on lifetime. Contrary to the OCDR, the CCDR requires a pre-cooling stage around 1.7K in order to evacuate the heat from thermalisation of He-3 and He-4 gas flows and from condensation of He-3 (a fraction this heat is used for the evaporation of He-3 but not all of it). As the close cycle dilution system requires a circulation of helium-3, there is no more high pressure storage tank like on Planck; therefore it is not possible to produce a 1.7K stage with a He-3 Joule-Thomson expansion within the dilution system. As a consequence, the 1.7K stage is produced by a dedicated small helium sorption cooler. The CCDR system also provides extra cooling power between 200mK and 600mK if needed (e.g. for thermalisation of mechanical supports or harnesses). Depending on the selected technology for the helium-3 re-circulation pump (ongoing trade-off), CCDR will also requires a 15mW heat lift at 15K (cryo pump solution) or a 100W heat lift at 300K (drag pump solution). Note that cryo pump uses a sorption-like principle (charcoal) and that the drag pump works around 1000-2000 Hz so the vibrations induced in both cases should not be important. Maturity level of CCDR is considered TRL 4, and should reach TRL 5 within 2 years with the ongoing developments at Air Liquide / CNRS Neel institute.

Back-up: the 0.1K stage could also be provided by an ADR cryocooler (e.g. from CEA SBT), also requiring at pre-cooling (e.g. at 1.7K and 4K on SAFARI/SPICA).

10.1.5 PTC

This stage is provided by a Pulse Tube cooler under development at Air Liquide/CEA (with a goal to reach 15K). Note that a 2-stage PT with a 300mW heat lift at 20K (with intercept) has already been demonstrated on the GSTP program 20-50K Pulse Tube (ESA contract 20497/06/NL/PA). Ongoing developments will allow to have more margin at the 20K stage. This 20K PT stage requires a pre-cooling at 80K with a heat intercept around 6W. Note that a pre-cooling at higher temperature (e.g. 120K) is possible, but with a slight decrease of the performance at 20K. This heat intercept can be provided either by a V-groove through thermal braids links for example (preferred solution), or by a dedicated 80K Pulse Tube. Maturity level of the 20K PT is considered TRL 4.

Back-up: the 20K could also be provided by a H2 JT with metal-sorption compressor from JPL (Planck) or a PT from NGST (US)

10.2 Mission and Spacecraft technology challenges

10.2.1 Data rate

COrE requires a data rate of 6 Mbits/s. Transmitting telemetry at such a high data rate requires a wide frequency bandwidth, by far above the 10 MHz maximum allowed by the ECSS standard in the frequency band allocated to L2 missions (8450-8500 MHz). Then the use of Ka band shall be considered as the baseline for the science telemetry transmission of the COrE mission. In order to achieve the link budget, the 35 m ground station located at New Norcia is required as for Planck operations. From on board side, a 0,5 m diameter high gain antenna pointing towards the Earth is required. Three configuration options are identified for the antenna: 1.Antenna pointing mechanism (existing) 2. Active antenna pointing (R&D study on-going) and 3. a fixed parabola antenna, pointed towards the Earth by the spacecraft. The conservative option 3 is taken as the baseline.

10.3 Payload technology challenges and technology development strategy

Text

10.4 Mission and Spacecraft technology challenges

Text

11 Programmatic and cost analysis (2 pages) PdB, FRB

Text

11.1 Overall proposed mission management structure

Text

11.2 Mission schedule drivers (technology developments, etc)

Text

11.3 Payload/Instrument Cost

Text

11.3.1 Assumed share of payload costs to ESA

Text

11.3.2 Estimated non-ESA payload costs

Text

11.4 Overall mission cost analysis

Text

12 Communication and Outreach (1 page) PdB, FRB

Text

13 Marco Bersanelli—Scanning strategy document

I am putting this document here because it is not immediately clear where and how to insert this text.

13.1 CORE Orbit and Scanning Strategy

The combination of orbit and scanning strategy for CORE must ensure that all the frequency channels will cover the full sky with adequate sampling and redundancy, while minimizing environmental systematic effects. The optimization of the CORE scanning strategy will be carried out during the detailed study phase, however, CORE will inherit many of the features successfully implemented for the *Planck* mission.

The choice of a far-Earth orbit, such as a halo or a quasi-periodic Lissajous orbit around the Sun-Earth Lagrangian point L2, is a mandatory feature for CORE in order to minimize straylight contamination from sidelobe pick-up. Requirements for far-sidelobe rejection are extremely tight for CORE. Because the broad features of the beam pattern at large off-axis angles are essentially the same for all detectors at a given frequency, the required rejection must be calculated against the total sensitivity per frequency channel. Using *Planck* as a guideline (Tauber et al 2010, A&A, 520, A2), and assuming a factor of 10 better sensitivity for CORE in an L_2 orbit, we need roughly 110 dB rejection for Sun contamination, 100 dB for the Earth, and 80 dB for the Moon. Stringent, highly frequency-dependent rejection requirements will be imposed also by straylight from Galactic diffuse emission on intermediate sidelobes. While challenging, straylight rejection limits for CORE can be achieved with very careful optical design, and can be tested with a moderate extrapolation of the state-of-the-art technology developed by ESA for the *Planck* mission. Furthermore, the excellent thermal stability of the L_2 environment is ideal to minimize thermal systematic effects on the CORE instrument. The experiences of both WMAP and *Planck* have demonstrated exquisite thermal stability for small changes in the solar aspect angle , with very small and slow residual thermal drifts. During the first-year *Planck* survey, in particular, the measured in-flight temperature of the passively cooled stage at 50K was stable at $\sim X$ mK/day, while the *Planck*-HFI 0.1 stage was stable at $\sim Y$ μK/day. **This may be sensitive information — check with *Planck* science team.**

An L_2 orbit is compatible with several options for the scanning strategy. A natural choice, described here as an example of a viable solution, is to follow the *Planck* scanning concept optimized to the CORE case. Let us assume the CORE spacecraft to be a spinner with spin rate $f_{\rm spin}$ and with bore-sight telescope angle $\theta_{\rm telescope}$. The spin rate $f_{\rm spin}$ needs to be fast enough to ensure redundancy for minimizing the effect of $1/f$ noise and thermal fluctuations, and slow enough to be compatible with the bolometer time constants. Based on the *Planck* experience, we anticipate $f_{\rm spin} \sim 0.3$ rpm. For a step-and-point approach, as in *Planck*, and given the natural constraint on the average de-pointing rate $\Delta\varphi/\Delta t = 1^\circ$/day to maintain nearly anti-solar configuration, we could set for example a de-pointing of $\Delta\varphi = 1.25'$every 10 circles in the sky. This would yield sufficient redundancy in sky circles and, simultaneously, good sampling of the sky for each single beam up to 220 GHz, i.e. in all the main CORE cosmological channels. At higher frequencies, where the angular resolution is $\theta_{\rm FWHM} < 4'$, adequate sampling would be ensured by proper staggering of the feeds in the focal plane.

Further constraints are imposed on the scanning parameters by thermal and straylight effects, and by telecommunication requirements. The maximum excursion $\Psi_{\rm SAA,Max}$ of the spin axis from anti-Sun direction must be limited, typically within about $\pm 15^\circ$, in order to avoid thermal effects and straylight contamination from the Sun and Moon, and to rule out power-modulation due to asymmetries in the spacecraft or shadowing effects on the solar panels. Also, the angle $\Psi_{\rm Earth,Max}$ of the spin-axis to Earth angle must be limited within $\sim 20^\circ$ to ensure good visibility of a fixed medium gain antenna for TM/TC activity. While steerable antenna designs are possible, we do not favor their use since they would complicate the design and increase the risk.

The choice for $\theta_{\rm telescope}$ is coupled to $\Psi_{\rm SAA,Max}$ through the requirement of full-sky coverage. Based on the *Planck* experience we can assume as a baseline $\theta_{\rm telescope} \sim 80^\circ$, which leaves ample margin of optimization for the way in which $\Psi_{\rm SAA}$ will be adjusted during the CORE surveys. Depending on the dynamical constraints and attitude control capabilities, modulation of the spin axis can be set either by precession (with the advantage of maintaining a constant $\Psi_{\rm SAA}$) or with cross-ecliptic excursions at an angle $\Psi_{\rm SAA} \leq 90^\circ - \theta_{\rm telescope}$. The optimal frequency of pointing modulations, $f_{\rm mod}$, will be determined via simulations that include polarization angle redundancy, destriping efficiency, and figures of merit for straylight and thermal effects. In Table 13 we summarize a possible baseline based on the *Planck* experience.

ENSSLIN SECTION

Parameter	Definition	Range	Potential criticalities
$\theta_{\rm telescope}$	Telescope axis to spin axis angle	75 – 85°	$> 85°$: Straylight: Polarisation angle redundancy, $< 75°$: Excessive excursion angle required to cover whole sky.
$f_{\rm spin}$	Spin rate	0.1 – 0.5 rpm	< 0.1 rpm: $1/f$ noise, thermal fluctuations, > 0.5 rpm: Bolometer time constant effects.
$\Delta\varphi$	Depointing angle	1' – 2'	$< 1'$: redundancy in sky circles: lifetime of thrusters, $> 2'$: insufficient sky sampling.
$\Psi_{\rm SAA,Max}$	Maximum solar aspect angle	10° – 20°	$< 10°$: coupling with $\theta_{\rm telescope}$ and full-sky requirement $> 20°$: thermal effects; straylight effects.
$\Psi_{\rm Earth,Max}$	Maximum Earth aspect angle	10° – 20°	$< 10°$: coupling with $\Psi_{\rm SAA,Max}$, $> 20°$: TM/TC reg's.
$f_{\rm mod}$	Modulation (precession) frequency	1 – 24 weeks	Polarisation angle redundancy; Destriping efficiency; Thermal effects.

Table 13: Main parameters and anticipated ranges for CORE scan strategy.

14 Statistical analysis of galactic magnetic fields with Planck LFI

The accuracy of Planck LFI polarization information on galactic magnetic fields provides a unique opportunity to study magneto-hydrodynamical turbulence and dynamo action in great detail within our Galaxy. An extension of the LFI operation would improve the reliability of the polarization data on small angular scales and thereby increase the spectral range of accurately probed magneto-hydrodynamical modes. Therefore, the detection potential for relevant plasma physical processes and their characteristic scales like turbulent energy injection and dissipation would be increased considerably. Furthermore, accurate galactic polarization data will be of eminent value for upcoming Faraday tomography measurements with telescopes like LOFAR, eVLA, ASKAP, and SKA.

14.1 Statistical analysis of galactic magnetic fields with Planck LFI

14.1.1 Faraday-rotation free polarization

The Planck LFI 30 and 44 GHz channels provide a very accurate, highly resolved and detailed view on the synchrotron emission of our own galaxy. The polarization data permits to study the morphology of galactic magnetic fields on global and local scales. CMB experiments measure at high frequencies and reveal there the original polarization structure. Planck will increase the angular resolution of such maps to a level comparable to ground based radio telescopes. All ground based radio-synchrotron measurements of galactic magnetic fields so far were at much lower frequencies. They therefore exhibit a large level of Faraday rotation and depolarization within the galactic plane hampering a direct analysis, whereas Planck LFI will show the Faraday-unrotated polarization structure (see Fig. 26). Having this unrotated polarization information with high precision will be of importance for at least two scientific research directions.

- Accurately measured fluctuations in the synchrotron flux in intensity and polarization provide insight into magnetic turbulence. Several characteristic statistical properties are encoded in this data, for example the energy and helicity spectra, as well as the spectrum of the magnetic tension force.
- Such data will also help Faraday rotation tomography measurements of our own galaxy, which will be pursued with upcoming instruments like LOFAR, eVLA, ASKAP, and SKA. Faraday tomography data can be expected to reveal further statistical information on Galactic fields, with a very promising potential for signatures of magneto-hydrodynamical processes to be explored.

Both research lines can and will be followed without a prolongation of the LFI operation. However, given that this will be the last chance for a long time to improve this polarization information further, the discovery potential should be fully exploited by obtaining the best possible galactic synchrotron data.

14.2 Magnetic spectra

The statistical properties of galactic magnetic fields imprint themselves on observables like synchrotron intensity, polarization and Faraday rotation measure. Methods to extract this information from observational data have been developed or are under construction. Quantities highly relevant for an understanding of galactic turbulence and dynamo processes were shown to be encoded in polarimetric data. Such are the magnetic

- **energy spectrum**, which is imprinted on intensity, polarization spectra and cross spectra [85, 86, 77, 78].
- **helicity spectrum**, which can be measured from polarimetric data in combination with extragalactic Faraday data [80, 81]. Magnetic helicity is a key quantity to understand the inner workings of large-scale galactic dynamos [73, 83, 84].
- **tension force spectrum**, which is encoded in polarimetry data alone, and is powerful in discriminating between different magneto-hydrodynamical scenarios [89].

More physical relevant information might be encoded in the data. The above examples are only the quantities that are known today, for which a reconstruction from Planck LFI data should be possible.

Due to our location within the galaxy, the angular fluctuations in observables correspond to physical magnetic field structures of different sizes. Disentangling those in order to separate different physical scales like turbulent injection scale (see e.g. [79]) or dissipative scales will be a challenge. Highly accurate polarimetric data, with an all sky view and calibration as Planck LFI will provide, will be of greatest value for this. The simultaneous probing of a large range of physical scales, however, in addition to the high angular resolution of Planck, will strongly increase the chance to catch signatures of the processes involved in galactic turbulence and dynamo theory.

14.3 Faraday tomography

Faraday tomography is a method to obtain three-dimensional information on magnetic fields and thereby restore some of the information lost in the line-of-sight projection involved in astronomical observations. The depth information of a synchrotron emitter is encoded in the rate of rotation of its polarization angle as a function of wavelength λ. For different sources at different physical depth, and therefore different Faraday depth, this rate differs. Mathematically, the observed polarization as a function of wavelength squared is the Fourier transformed polarized emission per Faraday depth [76].

An inverse Fourier transformation can therefore reveal the polarization per Faraday depth [74]. This technique was already applied successfully to radio data [75] and is extremely promising for upcoming radio telescopes. However, the problem for many of these measurements, especially for long wavelength telescopes like LOFAR, is that the full λ^2-space can not be examined. In particular, the negative part of this space is impossible to be probed by any instrument. However, information in the full λ^2-space would be required for a direct inversion of the Fourier relation. Therefore, inverse methods have to be applied which benefit from any available information, in particular close to the unaccessible negative λ^2 range. Thus, the information close to $\lambda = 0$ as it will be provided by Planck LFI will be of greatest importance for Faraday tomography.

Since the Farday tomographic data will provide much deeper insight into the details of Galactic magnetism than the two dimensional information discussed above, it is obvious that the scientific return will be even larger. Accurate all-sky Planck LFI data will be crucial for this technique to explore the richness of magnetic phenomena in the Galaxy.

14.4 CORE and Non-Polarized Point Sources

The sensitivity necessary for CORE to measure cosmological and other polarizations will also mean that it will be highly sensitive to non-polarized continuum sources. Indeed, even with a beam of 1.3 arcminutes at its highest frequency CORE will be so sensitive that source confusion will be the limiting factor in

its ability to detect extragalactic point sources. We can use galaxy counts from large area Herschel surveys (H-ATLAS and HerMES, Clements et al., (2010), Oliver et al., (2010)) at CORE wavelengths to determine the confusion limit for its beamsize and thus the number of sources that it will detect over the sky. Assuming a beam FWHM of 1.3 arcmin at 820GHz (Config. A), we find that the classical confusion detection limits of 20 and 40 beams per source correspond to flux limits of 49 and 41mJy respectively, substantially above the CORE sensitivity in this band of 7mJy. Assuming that CORE, like IRAS, is sufficiently free of galactic confusion above —b— $\sim$ 20, then this would correspond to a final extragalactic source catalog of 1.4 to 2.8 million sources for the different classical confusion limits.

Surveys of small areas of the sky are already available at 350μm with somewhat better angular resolution and comparable depth from Herschel. In Fig. ?? we show the 4x4 degree region surveyed by H-ATLAS (Eales et al., 2010; Rigby et al., 2010) smoothed to the 1.3 arcmin FHWM beam of CORE at this wavelength.

Amongst the brightest objects in this H-ATLAS image are five lensed background galaxies lying at z$\sim$2, which can easily be identified by their red far-IR colour and absence from radio surveys (Negrello et al., 2010). CORE will be able to use its longer wavelengths to provide a similar selection of high redshift lensed far-IR sources, but this will be possible over not the few 10s or 100s of sq. deg. possible with Herschel, but over the entire sky. Using updated versions of Negrello et al. (2007)'s models of the submm number counts, we estimate that CORE will be able to detect and identify $\sim$60000 lensed background dusty galaxies since the lensing fraction at these fluxes is predicted to be 2.5-4%.

References

[EXTRAGALACTIC SOURCES REFS] EXTRAGALACTIC REFS

[Agudo et al.(2010)] Agudo, I., Thum, C., Wiesemeyer, H., Krichbaum, T. P. (2010) "A 3.5 mm Polarimetric Survey of Radio-loud Active Galactic Nuclei", ApJS 189, 1

[Colafrancesco(2008)] Colafrancesco, S. (2008) "SZ effect from radio-galaxy lobes: astrophysical and cosmological relevance", MNRAS 385, 2041

[Croston et al.(2009)] Croston, J. H., et al. (2009) "High-energy particle acceleration at the radio-lobe shock of Centaurus A", MNRAS 395, 1999

[de Zotti et al.1999] de Zotti, G., Gruppioni, C., Ciliegi, P., Burigana, C., Danese, L. (1999) "Polarization fluctuations due to extragalactic sources", New Astronomy 4, 481

[de Zotti et al.(2005)] De Zotti, G., Ricci, R., Mesa, D., Silva, L., Mazzotta, P., Toffolatti, L., González-Nuevo, J. (2005) "Predictions for high frequency radio surveys of extragalactic sources", A&A, 431, 893

[Greaves & Holland(2002)] Greaves, J. S., Holland, W. S. (2002) "Submillimetre polarization of M82 and the Galactic Center: Implications for CMB polarimetry", AIP Conf. Proc. 609: Astrophysical Polarized Backgrounds 609, 267-270.

[Jackson et al.(2010)] Jackson, N., Browne, I. W. A., Battye, R. A., Gabuzda, D., Taylor, A. C. (2010) "High-frequency radio polarization measurements of WMAP point sources", MNRAS 401, 1388

[Kronberg(1994)] Kronberg, P. P. (1994) "Extragalactic magnetic fields", Rep. Prog. Phys. 57, 325

[López-Caniego et al.(2009)] López-Caniego, M., Massardi, M., González-Nuevo, J., Lanz, L., Herranz, D., De Zotti, G., Sanz, J. L., Argüeso, F. (2009) "Polarization of the WMAP Point Sources", ApJ 705, 868

[Massardi et al.(2008)] Massardi, M., et al. (2008) "The Australia Telescope 20-GHz (AT20G) Survey: the Bright Source Sample", MNRAS 384, 775

[Negrello et al.(2007)] Negrello, M., Perrotta, F., González-Nuevo, J., Silva, L., de Zotti, G., Granato, G. L., Baccigalupi, C., Danese, L. (2007) "Astrophysical and cosmological information from large-scale submillimetre surveys of extragalactic sources", MNRAS 377, 1557

[Ricci et al.(2004)] Ricci, R., Prandoni, I., Gruppioni, C., Sault, R. J., De Zotti, G. (2004) "High-frequency polarization properties of southern Kühr sources", A&A 415, 549

[Seiffert et al.(2007)] Seiffert, M., Borys, C., Scott, D., Halpern, M. (2007) "An upper limit to polarized submillimetre emission in Arp 220", MNRAS, 374, 409

[Shi et al.(2010)] Shi, H., Liang, H., Han, J. L., Hunstead, R. W. (2010) "Radio sources with ultrahigh polarization", MNRAS, in press, arXiv:1007.2367

[Tucci et al.(2004)] Tucci, M., Martínez-González, E., Toffolatti, L., González-Nuevo, J., De Zotti, G. (2004) "Predictions on the high-frequency polarization properties of extragalactic radio sources and implications for polarization measurements of the cosmic microwave background", MNRAS 349, 1267

[Tucci et al.(2005)] Tucci, M., Martínez-González, E., Vielva, P., Delabrouille, J. (2005) "Limits on the detectability of the CMB B-mode polarization imposed by foregrounds", MNRAS 360, 935

[Wright et al.(2009)] Wright, E. L., et al. colleagues (2009) "Five-Year Wilkinson Microwave Anisotropy Probe Observations: Source Catalog", ApJS 180, 283

[REIONIZATION REFS] REIONIZATION REFS

[Burigana et al.(2008)] Burigana, C., Popa, L. A., Salvaterra, R., Schneider, R., Choudhury, T. R., & Ferrara, A. 2008, MNRAS, 385, 404

[Dvorkin & Smith(2009)] Dvorkin, C., & Smith, K. M. 2009, PRD, 79, 043003

[Larson et al.(2010)] Larson, D., et al. 2010, arXiv:1001.4635

[Mortonson & Hu(2008)] Mortonson, M. J., & Hu, W. 2008, ApJ, 672, 737

[Naselsky & Chiang(2004)] Naselsky, P., & Chiang, L.-Y. 2004, MNRAS, 347, 795

[1] Kronberg, P. P. 2005, in Lecture Notes in Physics, Berlin Springer Verlag, Vol. 664, Cosmic Magnetic Fields, ed. R. Wielebinski & R. Beck, 9–+

[2] Kronberg, P. P., Bernet, M. L., Miniati, F., et al. 2008, ApJ, 676, 70

[3] Grasso, D. & Rubinstein, H. R. 2001, Phys. Reports, 348, 163

[4] Giovannini, M. 2004, Phys. Rev. D, 70, 123507

[5] Giovannini, M. & Kunze, K. E. 2008a, Phys. Rev. D, 78, 023010

[6] Giovannini, M. & Kunze, K. E. 2008b, Phys. Rev. D, 77, 063003

[7] Battaner, E. Florido, E. 2009, Cosmic Magnetic Fields: From Planets, to Stars and Galaxies, Proc. IAU Symp 259, Cambridge Univ. Press.

[8] Lewis, A. 2004, Phys. Rev. D, 70, 043011

[9] Paoletti, D., Finelli, F., & Paci, F. 2009, MNRAS, 396, 523

[10] Kosowsky, A., Kahniashvili, T., Lavrelashvili, G., & Ratra, B. 2005, Phys. Rev. D, 71, 043006

[11] Kahniashvili, T., Maravin, Y., & Kosowsky, A. 2009, Phys. Rev. D, 80, 023009

[12] Scóccola, C., Harari, D., & Mollerach, S. 2004, Phys. Rev. D, 70, 063003

[13] Kristiansen, J. R., & Ferreira, P. G. 2008, Phys. Rev. D, 77, 123004

[14] Reichborn-Kjennerud B. et al, "EBEX: A balloon-borne CMB polarization experiment", Proceedings of the SPIE, Volume 7741, pp. 77411C-77411C-12 (2010). (arXiv:1007.3672)

[15] K. Ichikawa, M. Fukugita and M. Kawasaki, "Constraining neutrino masses by CMB experiments alone," Phys. Rev. D **71** (2005) 043001 [arXiv:astro-ph/0409768].

[16] Abazajian, K., & Dodelson, S. 2003, Physical Review Letters, 91, 041301

[17] A. Slosar, "Detecting neutrino mass difference with cosmology," Phys. Rev. D **73**, 123501 (2006) [arXiv:astro-ph/0602133].

[18] M. Kaplinghat, L. Knox and Y. S. Song, "Determining neutrino mass from the CMB alone," Phys. Rev. Lett. **91** (2003) 241301 [arXiv:astro-ph/0303344].

[19] G. L. Fogli *et al.*, "Observables sensitive to absolute neutrino masses (Addendum)," Phys. Rev. D **78** (2008) 033010 [arXiv:0805.2517 [hep-ph]].

[20] Beck, M., & the Katrin collaboration 2010, Journal of Physics Conference Series, **203**, 012097

[21] J. R. Kristiansen and O. Elgaroy, "Cosmological implications of the KATRIN experiment," JCAP **0801** (2008) 007 [arXiv:0709.4152 [astro-ph]].

[22] H. V. Klapdor-Kleingrothaus, I. V. Krivosheina, A. Dietz and O. Chkvorets, "Search for neutrinoless double beta decay with enriched 76Ge in Gran Sasso 1990-2003," Phys. Lett. B **586** (2004) 198 [arXiv:hep-ph/0404088].

[23] Monfardini, A., et al. 2006, Nuclear Instruments and Methods in Physics Research A, **559**, 346

[24] R. Bowen, S. H. Hansen, A. Melchiorri, J. Silk and R. Trotta, "The Impact of an Extra Background of Relativistic Particles on the Cosmological Parameters derived from Microwave Background Anisotropies," Mon. Not. Roy. Astron. Soc. **334**, 760 (2002) [arXiv:astro-ph/0110636].

[25] G. Mangano, G. Miele, S. Pastor and M. Peloso, "A precision calculation of the effective number of cosmological neutrinos," Phys. Lett. B **534** (2002) 8 [arXiv:astro-ph/0111408].

[26] G. Mangano, G. Miele, S. Pastor, T. Pinto, O. Pisanti and P. D. Serpico, "Effects of non-standard neutrino electron interactions on relic neutrino decoupling," Nucl. Phys. B **756** (2006) 100 [arXiv:hep-ph/0607267].

[27] R. Trotta and S. H. Hansen, "Observing the helium abundance with CMB," Phys. Rev. D **69**, 023509 (2004) [arXiv:astro-ph/0306588].

[28] K. Ichikawa, T. Sekiguchi and T. Takahashi, "Primordial Helium Abundance from CMB: a constraint from recent observations and a forecast," Phys. Rev. D **78** (2008) 043509 [arXiv:0712.4327 [astro-ph]].

[29] Hamann, J., Lesgourgues, J., & Mangano, G. 2008, Journal of Cosmology and Astro-Particle Physics, **3**, 4

[30] F. Iocco, G. Mangano, G. Miele, O. Pisanti and P. D. Serpico, "Primordial Nucleosynthesis: from precision cosmology to fundamental physics," Phys. Rept. **472**, 1 (2009) [arXiv:0809.0631 [astro-ph]].

[31] Komatsu, E., et al. 2010, arXiv:1001.4538.

[32] Bartolo, Nicola; Komatsu, Eiichiro; Matarrese, Sabino; Riotto, Antonio (2004) "Non-Gaussianity from inflation: Theory and observations," Phys. Rept. 402, 103 (2004) (astro-ph/0406398)

[33] Bartolo, Nicola; Matarrese, Sabino; Riotto, Antonio (2010) "Non-Gaussianity and the Cosmic Microwave Background Anisotropies," Adv. Astron. 157079 (arXiv:1001.3957)

[34] Komatsu, Eiichiro (2010) "Hunting for Primordial Non-Gaussianity in the Cosmic Microwave Background," Class. Quant. Grav. 27, 124010 (2010) (arXiv:1003.6097)

[35] Yadav, Amit P.S.; Wandelt, Benjamin D. (2010) "Primordial Non-Gaussianity in the Cosmic Microwave Background," Adv. Astron. 565248 (arXiv:1006.0275)

[36] M. Liguori, E. Sefusatti, J. R. Fergusson, and E. P. S. Shellard. Primordial non-Gaussianity and Bispectrum Measurements in the Cosmic Microwave Background and Large-Scale Structure. (2010) [arXiv:1001.4707].

[37] A. A. Fraisse, C. Ringeval, D. N. Spergel and F. R. Bouchet, "Small-Angle CMB Temperature Anisotropies Induced by Cosmic Strings" Phys. Rev. D **78**, 043535 (2008) [arXiv:0708.1162 [astro-ph]]

[38] Regan, D. M. and E.P.S. Shellard, "Cosmic String Power Spectrum, Bispectrum and Trispectrum", *Physical Review* **D82**, 063527 (2010) [arXiv:0911.2491].

[39] Lehners, Jean-Luc; Steinhardt, Paul J. (2010) "Ekpyrotic Non-Gaussianity: A Review," Adv. Astron.,903907 (2010) (arxiv:1001.3125)

[40] Acquaviva, Viviana; Bartolo, Nicola; Matarrese, Sabino; Riotto, Antonio (2003) "Second-order cosmological perturbations from inflation," Nucl. Phys. B 667, 119 (arXiv:astro-ph/0209156)

[41] Maldacena, Juan M. (2003) "Non-Gaussian features of primordial fluctuations in single field inflationary models," JHEP 0305, 013 (arXiv:astro-ph/0210603)

[42] Komatsu, Eiichiro et al., (2009) "Non-Gaussianity as a Probe of the Physics of the Primordial Universe and the Astrophysics of the Low Redshift Universe," arXiv:0902.4759

[43] Senatore, Leonardo; Smith, Kendrick M.; Zaldarriaga, Matias (2010) "Non-Gaussianities in Single Field Inflation and their Optimal Limits from the WMAP 5-year Data," JCAP **1001**, 028 (arXiv:0905.3746)

[44] Bartolo, Nicola; Fasiello, Matteo; Matarrese, Sabino; Riotto, Anotnio (2010) "Large non-Gaussianities in the Effective Field Theory Approach to Single-Field Inflation: the Bispectrum," JCAP 1008, 008 (arXiv:1004.0893)

[45] Chen, Xingang, Huang; Min-xin; Kachru, Shamit; Shiu, Gary (2007) "Observational signatures and non-Gaussianities of general single field inflation," JCAP 0701, 002 (arXiv:hep-th/0605045)

[46] Alishahiha, Mohsen; Silverstein, Eva; Tong, David (2004) "DBI in the sky," Phys. Rev. D 70, 123505 (arXiv:hep-th/0404084)

[47] Arkani-Hamed, Nima; Creminelli, Paolo; Mukohyama, Shinji; Zaldarriaga, Matias (2004) "Ghost Inflation," JCAP 0404, 001 (arXiv:hep-th/0312100)

[48] Langlois, David; Renaux-Petel, Sebastien; Steer, Daniel A.;Tanaka, Takahiro (2008) "Primordial perturbations and non-Gaussianities in DBI and general multi-field inflation," Phys. Rev. D 78, 063523 (arXiv:0806.0336)

[49] Creminelli, Paolo, and Zaldarriaga, Matias (2004) 'A Naturally Large Four-Point Function in Single Field Ination", [arXiv:1004.1201].

[50] Wang, li-Min; Kamionkowski, Marc (2000) "The cosmic microwave background bispectrum and inflation," Phys. Rev. D 61, 063504 (arXiv:astro-ph/9907431)

[51] Chen, Xingang; Easther, Richard; Lim, Eugene A. (2007) "Large non-Gaussianities in single field inflation," JCAP 0706, 023 (arXiv:astro-ph/0611645)

[52] Chen, Xingang; Easther, Richard; Lim, Eugene A. (2008) "Generation and Characterization of Large Non-Gaussianities in Single Field Inflation," JCAP 0804, 010 (arXiv:0801.3295)

[53] Chen, Xingang, "Primordial Non-Gaussianities from Inflation Models", Adv. Astron. 2010:638979 (2010) [arXiv:1002.1416].

[54] Creminelli, Paolo; Zaldarriaga, Matias (2004) "Single field consistency relation for the 3-point function," JCAP 0410, 006 (arXiv:astro-ph/0407059)

[55] Chen, Xingang (2005) "Running Non-Gaussianities in DBI Inflation," Phys. Rev. D 72, 123518 (arXiv:astro-ph/0507053)

[56] LoVerde, Marilena; Miller, Amber; Shandera, Sarah; Verde, Licia (2008) "Effects of Scale-Dependent Non-Gaussianity on Cosmological Structures," JCAP **0804**, 014 (arXiv:0711.4126)

[57] Bernardeau, Francis and Uzan, Jean-Philippe, "Non-Gaussianity in multi-field inflation", Phys. Rev. D66, 103506 (2002). [hep-ph/0207295].

[58] Lyth D H and Rodriguez Y, "The inflationary prediction for primordial non-Gaussianity", Phys. Rev. Lett. 95 121302 (2005). [astro-ph/0504045[.

[59] Rigopolous, G., E.P.S. Shellard and B.J.W. van Tent, "Large non-Gaussianity in multiple-field inflation", *Physical Review* **D73** 083522 (2006) [astro-ph/0506704].

[60] Byrnes, Christian T.; Choi, Ki-Young; Hall, Lisa M.H. (2009) "Large non-Gaussianity from two-component hybrid inflation," JCAP 0902, 017 (arXiv:0812.0807)

[61] Byrnes, Christian T.; Nurmi, Sami; Tasinato, Gianmasimo; Wands, David (2010) "Scale dependence of local $f_{\rm NL}$," JCAP 1002, 034 [arXiv:0911.2780 [astro-ph.CO]]

[62] Bartolo, Nicola; Fasiello, Matteo; Matarrese, Sabino; Riotto, Anotnio (2010) "Tilt and Running of Cosmological Observables in Generalized Single-Field Inflation," (arXiv:1010.3993)

[63] Lehners, Jean-Luc (2010) "Ekpyrotic Non-Gaussianity – A Review," Adv. Astron., 903907 (arXiv:1001.3125)

[64] Yadav, Amit P.S.; Wandelt, Benjamin D. (2008) "Evidence of Primordial Non-Gaussianity f_{NL} in the Wilkinson Microwave Anisotropy Probe 3-Year Data at 2.8σ," Phys. Rev. Lett. 100, 181301 (astro-ph/07121148)

[65] Regan, D. M., E.P.S. Shellard and J.R. Fergusson, "General CMB and Primordial Trispectrum Estimation", *Physical Review* **D82**, 023520 (2010) [arXiv:1004.2915].

[66] J. R. Fergusson and E. P. S. Shellard. The shape of primordial non-Gaussianity and the CMB bispectrum. *Phys. Rev.*, **D80**, 043510 (2009) [arXiv:0812.3413].

[67] J. R. Fergusson, M. Liguori, and E. P. S. Shellard. General CMB and Primordial Bispectrum Estimation I: Mode Expansion, Map-Making and Measures of f_{NL}. *Phys. Rev.* **D82**, 023502 (2010) [arXiv:0912.5516].

[68] J. R. Fergusson, M. Liguori, and E. P. S. Shellard. The CMB Bispectrum. (2010) [arXiv:1006.1642].

[69] A. D. Linde, Phys. Rev. D **49**, 748 (1994) [arXiv:astro-ph/9307002].

[70] N. Bevis, M. Hindmarsh, M. Kunz and J. Urrestilla, Phys. Rev. Lett. **100**, 021301 (2008) [arXiv:astro-ph/0702223].

[71] R. Battye and A. Moss, Phys. Rev. D **82**, 023521 (2010) [arXiv:1005.0479 [astro-ph.CO]].

[72] P. Mukherjee, J. Urrestilla, M. Kunz, A. R. Liddle, N. Bevis and M. Hindmarsh, arXiv:1010.5662 [astro-ph.CO].

[73] A. Brandenburg. The critical role of magnetic helicity in astrophysical large-scale dynamos. Plasma Physics and Controlled Fusion, 51(12):124043–+, Dec. 2009

[74] M. A. Brentjens and A. G. de Bruyn. Faraday rotation measure synthesis. A& A441:1217–1228, Oct. 2005

[75] M. A. Brentjens and A. G. de Bruyn. RM-synthesis of the Perseus cluster, Astronomische Nachrichten, 327:545–+, June 2006

[76] B. J. Burn. On the depolarization of discrete radio sources by Faraday dispersion, MNRAS, 133:67, 1966

[77] J. A. Eilek. Turbulence in extended synchrotron radio sources. I - Polarization of turbulent sources. II - Power-spectral analysis. ApJ, 98:244–266, July 1989

[78] J. A. Eilek. Turbulence in Extended Synchrotron Radio Sources. II. Power-Spectral Analysis, ApJ, 98:256, July 1989

[79] M. Haverkorn, J. C. Brown, B. M. Gaensler, and N. M. McClure-Griffiths. The Outer Scale of Turbulence in the Magnetoionized Galactic Interstellar Medium, ApJ, 680:362–370, June 2008.

[80] H. Junklewitz. Imprints on energy and helicity spectra on radio polarimetry data. Master's thesis, Ludwig Maximilian Universität München, 2010. (in preparationion)

[81] H. Junklewitz and T. A. Enßlin. Imprints on energy and helicity spectra on radio polarimetry data. in preparation, 2010.

[82] L. Page, G. Hinshaw, E. Komatsu, M. R. Nolta, D. N. Spergel, C. L. Bennett, C. Barnes, R. Bean, O. Doré, J. Dunkley, M. Halpern, R. S. Hill, N. Jarosik, A. Kogut, M. Limon, S. S. Meyer, N. Odegard, H. V. Peiris, G. S. Tucker, L. Verde, J. L. Weiland, E. Wollack, and E. L. Wright. Three-Year Wilkinson Microwave Anisotropy Probe (WMAP) Observations: Polarization Analysis, ApJ(Suppl), 170:335–376, June 2007.

[83] A. Shukurov, D. Sokoloff, K. Subramanian, and A. Brandenburg. Galactic dynamo and helicity losses through fountain flow, A& A, 448:L33–L36, Mar. 2006.

[84] D. Sokoloff, Astrophysical dynamos and magnetic helicity conservation, Plasma Physics and Controlled Fusion, 49:447–+, Dec. 2007.

[85] S. R. Spangler, The transport of polarized synchrotron radiation in a turbulent medium, ApJ, 261:310–320, Oct. 1982.

[86] S. R. Spangler, Determination of the properties of magnetic turbulence in radio sources, ApJ Lett, 271:L49–L53, Aug. 1983.

[87] X. H. Sun, W. Reich, A. Waelkens, and T. A. Enßlin, Radio observational constraints on Galactic 3D-emission models, A& A, 477:573–592, Jan. 2008.

[88] J. C. Testori, P. Reich, and W. Reich, A fully sampled λ21 cm linear polarization survey of the southern sky, A& A, 484:733–742, June 2008

[89] A. H. Waelkens, A. A. Schekochihin, and T. A. Enßlin, Probing magnetic turbulence by synchrotron polarimetry: statistics and structure of magnetic fields from Stokes correlators, MNRAS, 398:1970–1988, Oct. 2009

[90] M. Wolleben, T. L. Landecker, W. Reich, and R. Wielebinski, An absolutely calibrated survey of polarized emission from the northern sky at 1.4 GHz. Observations and data reduction," A&A 448:411–424, Mar. 2006

[91] Reichborn-Kjennerud B. et al, "EBEX: A balloon-borne CMB polarization experiment", Proceedings of the SPIE, Volume 7741, pp. 77411C-77411C-12 (2010). (arXiv:1007.3672)

[92] Tauber et al 2010, A& A, 520, A2.

[93] "Rapport de participation CNES á la proposition CV2 FPP", J. Michaud, S. D'escrivain, S. Tremoliere, B. Helin and D. Delrieu, internal report, Nov 2010.

[94] Chuss et al.....

[95] Engargiola et al., Rev. Sci. Instr. 74, 1380 (2003)

[96] Pisano G., et al., IEEE-MWCL, 17, 286 (2007)

[97] Peverini O.A., et al., IEEE-MTT, 54, 2042 (2006)

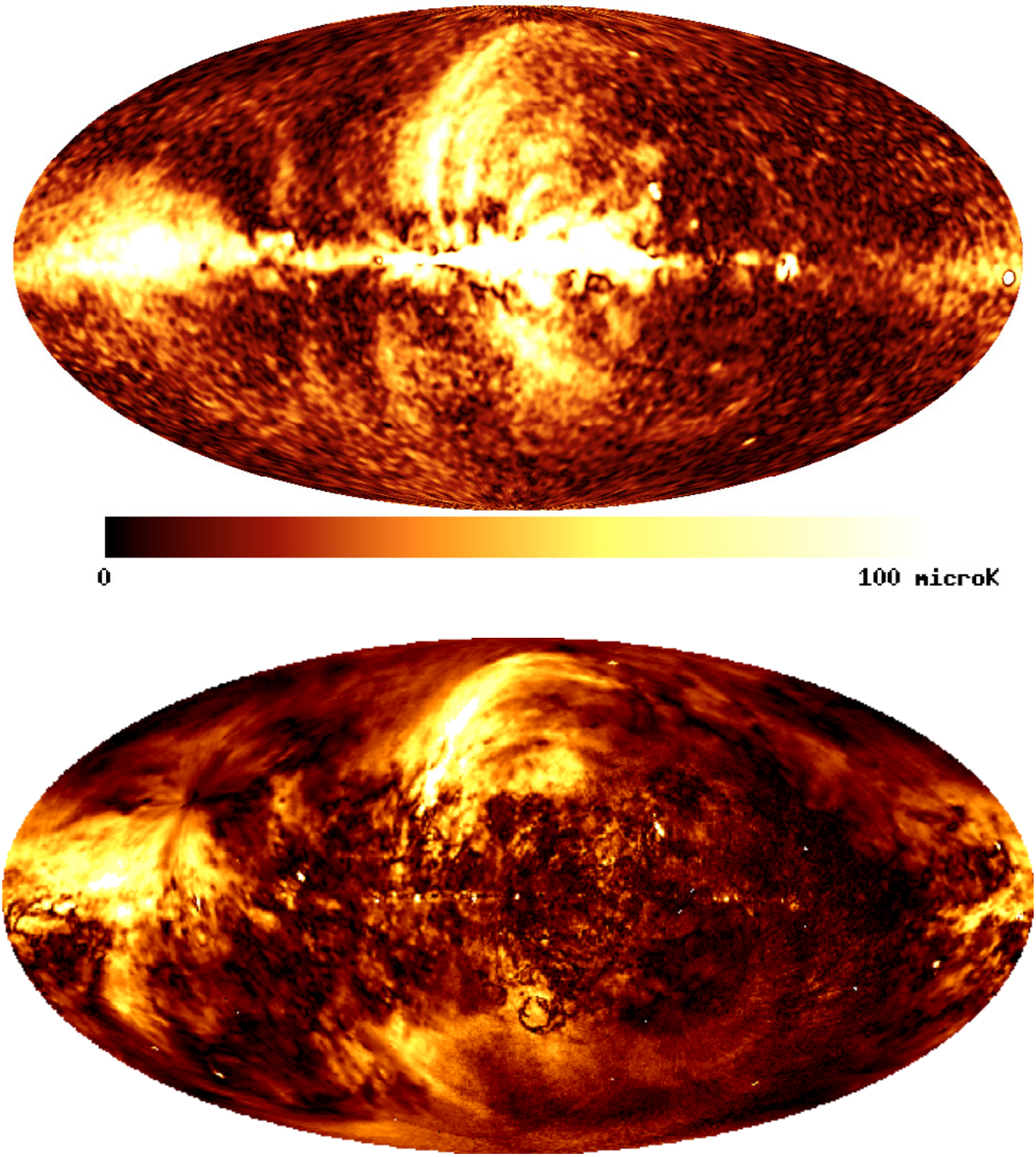

Figure 26: The WMAP 22.8 GHz all-sky polarized intensity map (upper panel) and the 1.4 GHz all-sky polarized intensity map (lower panel). The polarized intensities are shown greyscale coded from 0 to 100 μK for 22.8 GHz and from 0 to 570 mK for 1.4 GHz. Galactic Faraday-depolarization structures are visible in the lower frequency map. Data from [90, 82, 88] and figures from [87].

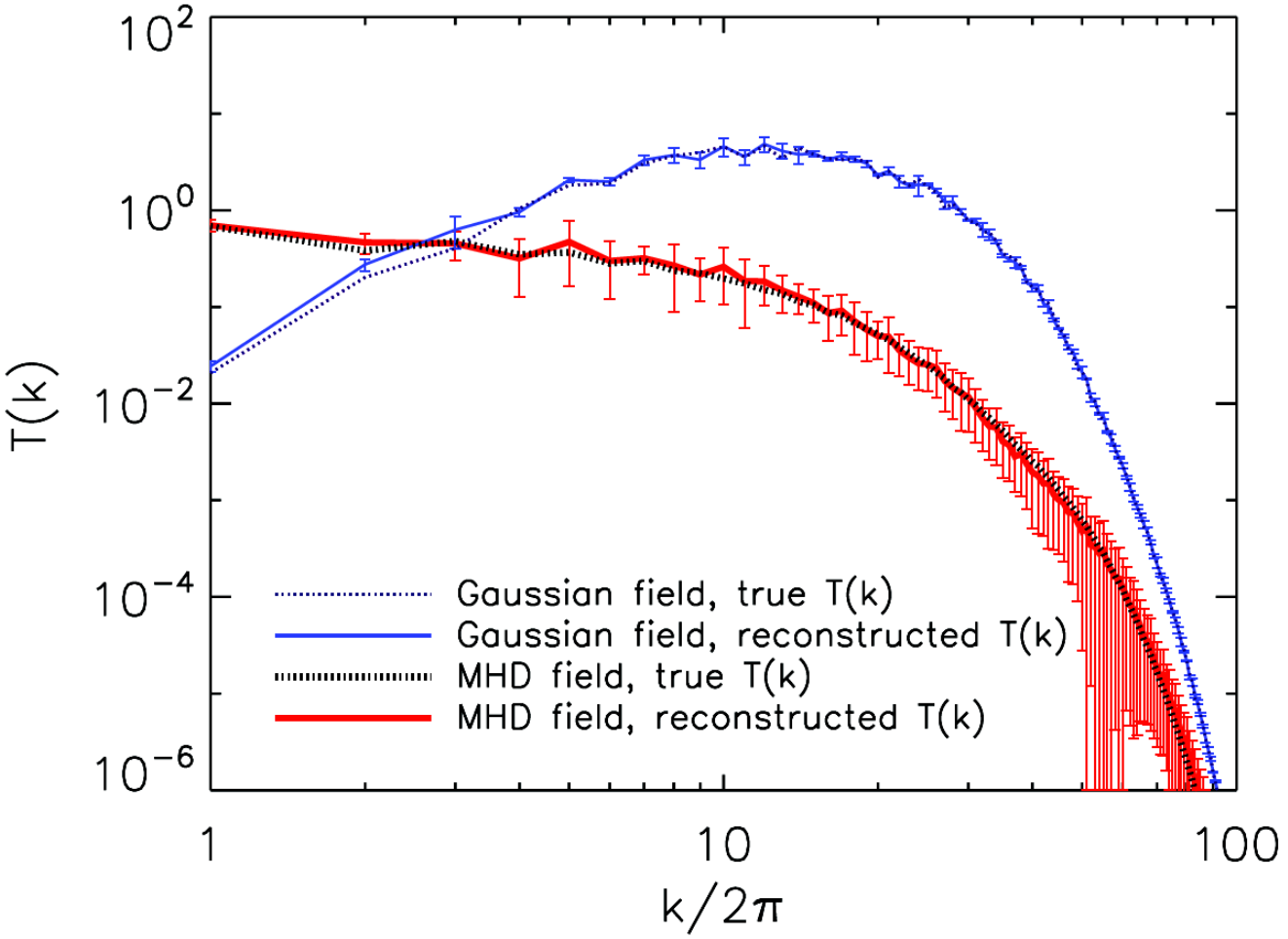

Figure 27: Tension force spectrum reconstructed from mock polarimetry data using the method of Stokes correlators (from [89]). The Gaussian random field was constructed to exhibit the same magnetic energy spectrum as the magneto-hydrodynamical simulation, but it has a different fourth-order statistic as measured by the Stokes correlators.

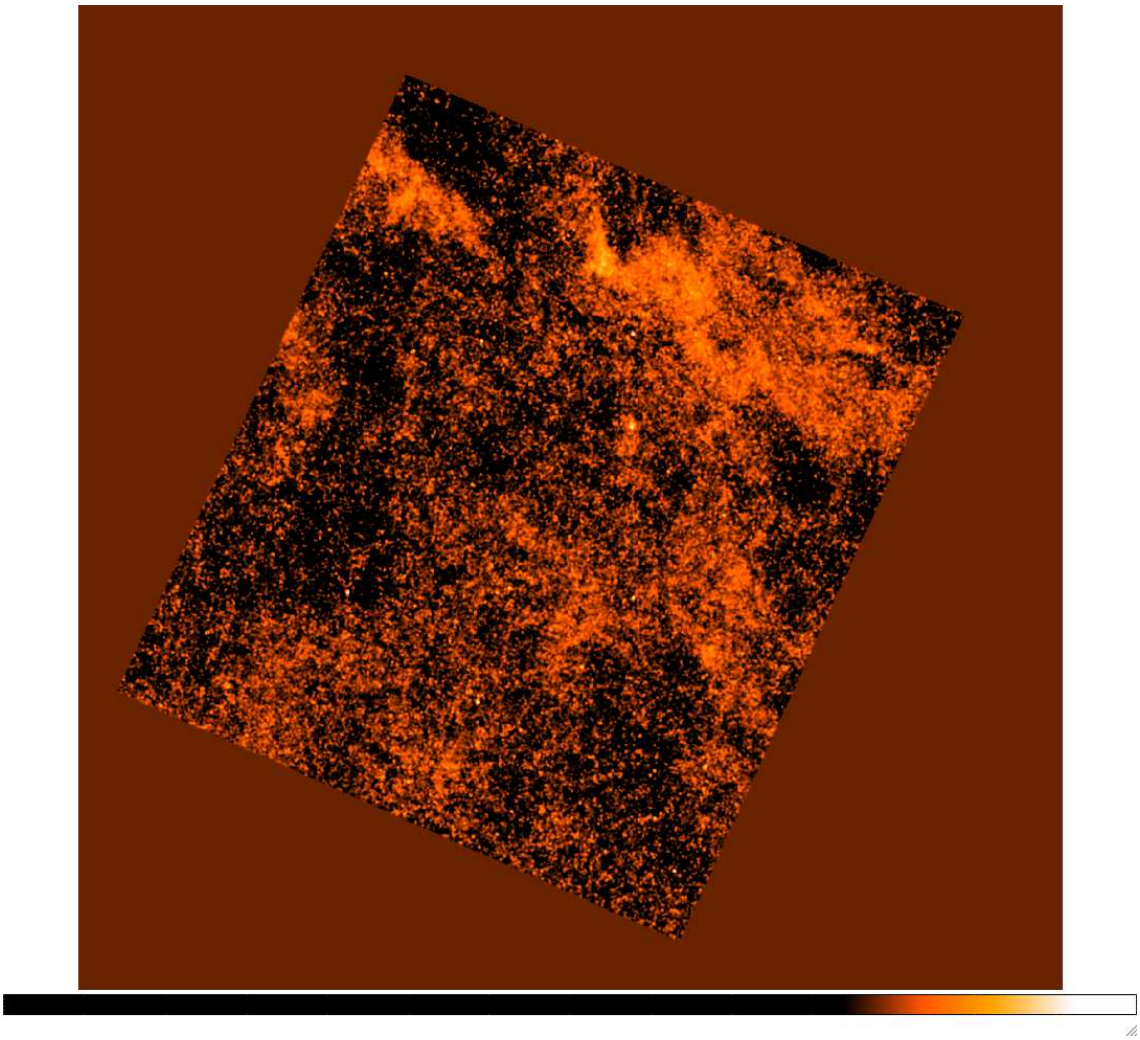

Figure 28: H-ATLAS 350μm SDP field smoothed to CORE resolution. Not the large number of point sources to be detected, and the presence of galactic cirrus dust structures. The brightest sources in this image include an unusual clump of galactic dust emission, possible a high lattitude Bok globule (Thompson et al., 2010), a WMAP blazar (Gonzales-Nuevo et al., 2010) and five lensed high redshift (z$\sim$2) dusty galaxies) Negrello et al., 2010)